UIN:657437386

CERTIFICATE OF COMMITTEE APPROVAL

University of Illinois at Urbana-Champaign
Graduate College

November 30, 2007

We hereby recommend that the thesis by:

ARAVIND SUNDARARAJAN

Entitled:
HEAT TRANSFER DURING MELT SPINNING OF AL-7%SI ALLOY ON A CU-BE WHEEL

Be accepted in partial fulfillment of the requirements for the degree of:

Master of Science

Signatures:

Director of Research - Brian G. Thomas

Head of Department - Huseyin Sehitoglu

Committee on Final Examination*

Chairperson -

Committee Member -

Committee Member -

Committee Member -

Committee Member -

Committee Member -

* Required for doctoral degree but not for master's degree

HEAT TRANSFER DURING MELT-SPINNING OF AL-7% SI ALLOY ON A CU-BE WHEEL

BY

ARAVIND SUNDARARAJAN

B.Eng.(Hons), Birla Institute of Technology and Science, Pilani, 2004

THESIS

Submitted in partial fulfillment of the requirements
for the degree of Master of Science in Mechanical Engineering
in the Graduate College of the
University of Illinois at Urbana-Champaign, 2007

Urbana, Illinois

Adviser:

Professor Brian Thomas

To My Parents
Sri. Sundararajan and Smt. Sudha Sundararajan

Acknowledgements

First and foremost, I take this opportunity to thank my advisor Prof Brian G. Thomas whose support has been pivotal to the success of this project. He has been a father, teacher and friend to me all through my years of assistantship under his honorable guidance. All over these years, he has been solely responsible for having shaped my personality and adding a professional tinge to my outlook. I thank the National Science Foundation (NSF), Grant # DMI 04-04-23794 and the Continuous Casting Consortium at UIUC for having provided support for this project. I also wish to thank Professor Paul Steen and graduate students, Cormac J. Byrne, Eric A. Theisen and Miachel J. Davis at Cornell University for providing the experimental measurements from their pilot caster. Thanks are also due to the Center for Microanalysis of Materials partially supported by the U.S. Department of Energy under grant DEFG02-91-ER4543 and James Mabon for helping with experimental measurements to obtain micrographs of sample. I also thank Joydeep Sengupta for initial research on the project, and Rajneesh Chaudhary for running fluid-flow simulations in FLUENT and all my other lab mates who have helped me in various forms with regards to this project.

Abstract

Transient heat transfer models of the single wheel melt-spinning process have been developed, validated and applied to quantify the effect of process variables including interface depressions on solidification, temperature evolution, thickness variations, and surface depressions in the cast product. Firstly, a one-dimensional transient heat transfer model (STRIP1D) has been developed to simulate Planar Flow Melt-Spinning (strip casting) of Al-7% Si on a Cu-Be wheel. This explicit finite-difference model takes into account the heat transfer and solidification occurring in the strip coupled with heat transfer occurring in the rotating wheel. Heat transfer in the liquid pool is incorporated from the results of a fluid flow / thermal model of the liquid melt pool run with FLUENT using the "superheat flux" method. This method is presented and validated by matching a test problem using both STRIP1D and ABAQUS. Heat transfer across the strip-wheel interface is modeled with a time-dependent heat transfer coefficient function, which depends on the measured gap height (distance between the wheel and the nozzle) and is consistent with previous measurements in other systems. The complete model is calibrated and validated using experimental data from a pilot caster at Cornell University. The model is able to reasonably match the measured strip thickness and wheel thermocouple temperature, including their variations in two different time scales. It also matches the measured strip surface temperature and secondary dendrite arm spacing. The models have then been used to understand the effect of process parameters including casting speed, puddle length (length of contact zone), gap height, superheat and interfacial depressions (gaps) on heat transfer in the strip, with the help of experimental measurements from the pilot caster. Next, transient two- and three-dimensional heat-transfer solidification models of the process have been developed using ABAQUS and validated using the STRIP1D Model. These models incorporate local variations in heat transfer along the length and width of the strip caused by surface defects. The effects of interfacial boron nitride deposits and air gaps were quantified by measuring and modeling longitudinal and transverse surface depressions observed on the wheel-side surface of the strip. Interfacial depressions decrease heat conduction to the wheel and thereby cause surface depressions on the opposite side of the strip. The predicted depression shapes match well with experimental measurements. The control of surface depressions in the melt-spinning process could enable strip casting with imprinted textured surfaces.

KEYWORDS: solidification, strip casting, fluid flow, microstructure**,** aluminum alloys, interface heat transfer, interface coefficient, aluminum alloys, heat transfer, superheat flux, models, thermocouple measurement, surface depressions, computational models.

Table of Contents

Nomenclature

Symbol	Variable	Value	Units
c_{pw}	Specific heat of wheel	419	J/kg K
k_w	Conductivity of wheel	260	W/m K
ρ_w	Density of wheel	8900	kg/ m^3
α_ω	Thermal diffusivity of wheel	6.97 x 10^{-5}	m^2/ sec
c_{ps}	Specific heat of strip	1190	J/kg K
k_s	Conductivity of strip	135	W/m K
ρ_s	Density of strip	2400	kg/ m^3
α_s	Thermal diffusivity of strip	4.73 x 10^{-5}	m^2/ sec
ΔH_L	Latent heat of fusion of Aluminum	417	KJ/ kg
Pe	Peclet number = $V_c\, s/\alpha$		
Q_{sides}	Heat source (from wheel sides)		W/mm^3
q_{amb}	Heat flux to ambient		W/mm^2
G	Gap height		mm
h_0	Initial interfacial heat transfer coefficient	225G	W/m^2 K
t_1	Contact time in Zone 1		Sec
t_{detach}	Total time of contact till strip exits Zone II		sec
q_{wn}	Heat flux into the wheel		W/m^2
q_{sn}	Heat flux leaving the strip		W/m^2
Δt	Time increment		sec
Δr	Increment in radial direction		m
Δz	Increment in angular direction		m
Δy	Unit depth		m
s	Final strip thickness		mm
v_C	Wheel / Casting speed		m/s
v_{C0}	Wheel / Casting speed for standard case in fluid-flow model	7.02	m/s
T_{sol}	Strip solidus temperature	555	^oC

T_{liq}	Strip liquidus temperature	614	^oC
T_{pour}	Strip pour temperature	714	^oC
PL	Puddle length (zone I length)		mm
D	Nozzle opening width	1.6	mm
B	Nozzle Breadth	9.8	mm
r_0	Wheel outer radius	0.304	m
r_i	Wheel inner radius	0.291	m
h_{amb}	Ambient heat transfer coefficient		W/m^2 K
t_0	Empirical reference time in h_{gap}. Eq. [15]	0.0001	sec
m	Empirical exponent in h_{gap}. Eq. [15]	0.33	
T_{amb}	Ambient temperature	31.7	^oC
ΔT	Superheat temperature	100	K
$T_{w_{init}}$	Initial wheel temperature	31.7	^oC
q_{sh}	Superheat flux added at the strip/liquid interface of standard case in fluid-flow model		MW/m^2
q_{sup}	Superheat flux added at strip/liquid interface		MW/m^2
t	Time from start of cast		sec
$\theta 1$ - $\theta 3$	Angles subtended from Zones 1 through 3		deg
v_a	Kinematic viscosity of air	7.04	m/s
μ_a	Dynamic viscosity of air	1.73×10^{-5}	Ns/m^2
ρ_a	Density of air	1.25	kg/m^3
k_a	Conductivity of air	0.01	W/m K
Σ	Stefan-Boltzmann constant	5.67×10^{-8}	$W/m^2/K^4$
T_{sn}	Strip cold surface temperature		K
T_{sf}	Strip hot surface temperature		K
h_{con}	Convective heat transfer coefficient occurring owing wheel movement		W/m^2K
h_{rad}	Radiative heat transfer coefficient occurring at the wheel surface		W/m^2K

T_{wn}	Wheel hot surface temperature		K
T_{w1}	Wheel cold surface temperature		K
Subscripts			
s	Pertaining to strip		
w	Pertaining to wheel		
i, n	Node numbers (Figure 2.4., Appendix A)		
f	Pertaining to solidification front		

List of Figures

1. Introduction

Near net shape products including thin sheets, thin strips, ribbons and foils can be manufactured efficiently with fine microstructures and unique properties by casting onto a single spinning roll [1-3]. Other processes to cast metal strip include twin roll; single belt (mold-trough train); twin belt; wheel-belt; and spray deposition[1]. When used to cast strips (thickness 1-10 mm) the process is called strip casting. Melt spinning can be used to cast thin strip (thickness 0.01-1 mm)[4, 5], and to rapidly quench metallic-glass (amorphous) ribbons[6, 7]. A major advantage of melt spinning over other conventional continuous casting processes is that thin strips cast with fine microstructural properties[3] are the final product and thereby circumventing expensive commercial finishing processes like rolling in order to produce a finished product. As a potential manufacturing process, this process could be an economical way to produce strip product with textured surfaces embossed with text and images. Recent interests in application of this process include steel strip casting, aluminum casting and special alloy casting.

The melt-spinning process is characterized by continuous delivery of molten metal onto a rapidly spinning substrate (wheel), which solidifies and quenches the metal into thin strips[8]. As soon as the molten metal is in contact with the substrate, a bond is formed at the interface, which quickly accelerates the strip to the wheel speed. This bond is also responsible for heat transfer to the wheel. The resistance to flow through the liquid metal delivery system together with the wheel rotation speed controls the thickness of the strip product. The heat transfer rate and the ultimate thickness together control the length of the molten metal pool. After leaving the liquid puddle, the metal solidifies into strip, cools and the thermal shrinkage during casting generates stresses that separate the strip from the wheel[9]. Single roll melt spinning can be either Chill block (CBMS) or Planar flow (PFMS)[3]. In CBMS, a high-speed metal jet streams onto the wheel surface from above and forms a puddle that is unconstrained by the crucible nozzle. In the PFMS processes, the crucible nozzle is very close to the wheel and constrains the upper surface of the melt puddle thereby enabling casting of thinner strips.

In order to quantify and understand the effects of various casting conditions and the effect of interfacial surface depressions on heat transfer, the development of a computational model of the process is pivotal. The strip produced during the melt-spinning process experiences different types of local surface imperfections, which are crucial to strip quality and the ability to control the surface texture and topology. Influencing factors include fluid flow in the melt pool, thermodynamics, air entrainment and dissolved gas evolution, surface tension and meniscus formation, heat transfer between the strip and the wheel, thermal properties of the strip and wheel, wheel geometry, wheel texture, length of puddle and contact regions and many other phenomena. Despite several efforts undertaken to model this process, no previous model has coupled the effects of fluid flow and heat transfer in the melt pool with solidification and heat transfer in the strip and transient conduction through the wheel. This emphasizes the need for a detailed theoretical model to quantify, understand, and optimize the heat transfer in this process.

In this work, transient multi-dimensional heat-transfer models have been developed of the melt-spinning process for Al-7%Si alloy which have been used to quantify the effect of process conditions on the heat transfer during the process. Chapter 2 explains the melt-spinning process and the various steps in the development and validation of the STRIP1D model of the process using experimental measurements obtained from the pilot caster at Cornell University[10]. Chapter 3 presents the development and validation of computational models in two- and three-dimensions with ABAQUS[11] application of these models to investigate the effects of process conditions such as casting speed, puddle length, gap thickness and superheat on solidification, and to predict the effect surface imperfections in the strip. Finally, Chapter 4 highlights some of the most important conclusions of the model and its implications on the process.

2. Model Development and Validation

2.1. Introduction

In this chapter, a comprehensive one-dimensional heat transfer model STRIP1D developed by Li and Thomas[12] has been modified to suit the melt-spinning process for Al-7%Si alloy. The STRIP1D model includes superheat transport in the liquid pool, solidification and cooling of the strip, and transient heat conduction in the rotating wheel. A steady model of fluid-flow and heat transfer is developed of the liquid pool with FLUENT[13] to obtain the superheat flux profile at the solidification front, which has been validated using a test case. A time-dependent heat transfer coefficient model of the contact region between the strip and the wheel has been developed and is discussed in section 2.6. The complete model is calibrated to match the time-dependent strip thickness and wheel temperatures[10] measured in the PFMS process at Cornell, and validated by comparing the secondary dendrite arm spacings, and strip surface temperatures measurements[10].

This project focuses on the PFMS process at Cornell University where Al-7% Si alloy is cast into thin 50mm-wide aluminum strips on a 100mm wide, 12.7mm thick Cu-Be wheel (substrate). Figure 2.1. shows a schematic of the process. Molten aluminum alloy at 714^{o}C (100 K superheat) is poured through the nozzle onto the rotating wheel. As the air-cooled wheel moves, the metal solidifies and detaches in the form of a solidified strip. The thickness *s*, of the ribbons produced ranges from 0.08mm to 0.35 mm[14].

2.2. Literature Review: Heat Flow Models of Melt Spinning

Previous work to investigate the strip-casting process includes inverse-model analysis of experimental measurements, heat transfer-solidification models of strip casting, melt spinning and other related processes, and numerical models coupling fluid-flow and heat transfer . Experimental studies have been conducted to understand heat transfer during the strip-casting process, and to extract the interfacial heat flux using inverse modeling [15-18]. To match experimental data, the fitted interface heat transfer coefficients decrease with increasing contact time, at a given casting speed (15 m/s)[15] The heat transfer coefficient increases with casting speed, perhaps owing to a reduction in size of air pockets formed at the melt-substrate interface[15]. Birat and co-workers[17] measured similar relations between the thickness of the solidifying shell at mold exit, heat flux, and residence time in the mold for continuous casting of steel.

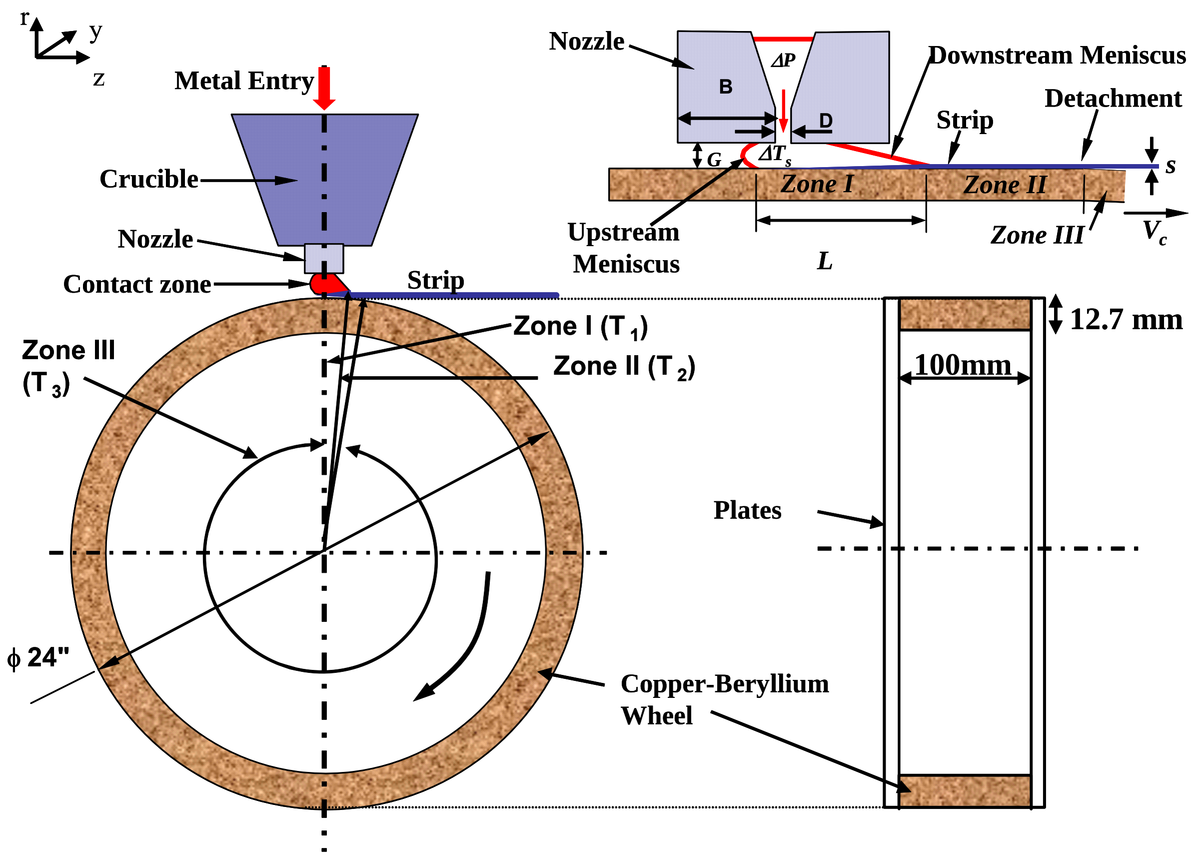

Figure 2.1. Schematic of Strip Casting Process

Mahapatra and Blejde[18] measured heat flux for steel strip casting at Castrip LLC. and observed that roll texture greatly affected heat transfer. The peak heat flux was found to characterize the effectiveness of the initial contact and to correlate well with the measured nucleation density. Keanini [19] used inverse modeling to estimate the surface heat flux distributions during high speed rolling, and observed high initial heat flux which decreased with time. Muojekwu et al[20] used a 1-D inverse model to find a decrease in both heat flux and heat transfer coefficient with time. In each study, heat flux was observed to decrease with time below the peak and usually, the heat transfer coefficient behaved similarly.

Several numerical models of heat transfer and solidification of strip casting focus on the strip-wheel heat transfer coefficient and other thermal behaviors and have estimated values of the interfacial heat transfer coefficient. Li and Thomas reviewed these values[21]. More recently, Wang and Matthys[22] reported an initial interfacial heat transfer coefficient in the range of 10 – 300 $kW/m^{-2}K^{-1}$. The highest values are achieved when the molten splat is in contact with the substrate, followed by a small value of less than 10 kW/m^2K during later stages of solidification. Ho and Phelke[23] used an inverse heat conduction method to study the interface heat transfer coefficient during casting of aluminum strip on a copper wheel. They found that an interfacial gap forms between the strip and the wheel and that the interface coefficient increases with contact pressure. Chen et al[24] investigated interface heat transfer behavior in free-jet casting of wood's alloy onto a moving copper substrate. A one-dimensional transient heat equation was used to calculate interface heat fluxes from the measured time-dependent substrate surface temperatures. Heat flux was reported to increase rapidly during the initial contact between the moving substrate and the melt puddle and later to decrease with time[24]. Li and Thomas[21] observed a similar initial increase in the measured thermocouple temperature for a steel strip-casting process, but reasoned that this was simply due to the time lag required to heat up the thermocouple embedded in the wheel. A good match with experiments was obtained from a simple equation for heat transfer coefficient that dropped continuously with time[21]. The initial maximum heat transfer coefficient of 16-28 kW/m^2K for varying speeds (0.5-1.5 m/s) decreased with time.

Numerous previous numerical models have been developed of strip casting and melt spinning. Many of these are one-dimensional transient models (of the wheel or of the strip) that have been used to determine average heat transfer coefficients in PFMS. Carpenter and Steen[25] calculated a value of 170 $kW/m^{-2}K^{-1}$, using one-dimensional Stefan problem of the strip. Kukura and Steen[26] have applied separate uncoupled one-dimensional numerical models of the wheel and strip in PFMS of Al-7% Si and determined an average interface coefficient of 110 $kWm^{-2}K^{-1}$. They predicted the increase in wheel temperature that arises each cycle. Wang et al[27] developed a 1-D control-volume model of the strip and the wheel to study the effects of undercooling and cooling rate on planar flow casting of aluminum strip on copper. Average heat transfer coefficients of 200 - 1000 kW m^{-2} °K^{-1} were reported. Hattel and Pryds[28] applied a 1-D control-volume solidification model of melt spinning. to find that the delay of initial solidification depends on both the heat transfer coefficient and wheel heating. Including the wheel in the numerical model was found to be essential (even for highly conductive copper), owing to its high surface temperatures.

In the related process of twin-roll strip casting, similar modeling efforts have been undertaken. Masounave el al[29] modeled the casting of A380 aluminum alloy on the IMRI steel twin-roll caster. They concluded that the heat transfer coefficient required to complete strip solidification at or before the roll pinch varied from 8.5 -10 kW/m^2 K. Caron et al[30] simulated a twin roll casting of 2 mm bronze and aluminum strips on steel roll at casting speed of 19m/min using a 1-D transient heat transfer model. The numerical results agreed with their experimental data when an average interface coefficient of 30 kW/m^{2}K was chosen.

Several models have investigated additional phenomena such as undercooling[4, 27],microstructure evolution[20], or 2-D effects[31]. Chen and Rajagopalan[4] developed a model with nucleation undercooling to study the effect of interfacial heat transfer coefficient on solidification of Al-Si alloys. The onset of solidification was delayed by 30-80 μs for 100-200K of undercooling. The computed solidification front growth profile was very different from the usual parabolic profile observed in other models and systems[27] and in classic theory[32]. It curved upwards and rose steeply, and with undercooling of 100-200K, a very high interfacial solidification velocity of the order of 4-10 m/s was predicted. Muojekwu et al[20] investigated the heat transfer and secondary dendrite arm spacings (SDAS) during solidification of Al-Si alloys. Based on dip tests of the chill, instrumented with thermocouples into the alloys, a one-dimensional implicit finite–difference model was applied to also study the effect of mold surface roughness, mold material, metal superheat, alloy composition, and lubricant on heat transfer and cast structure. Papai and Mobley [31, 33] developed a time-dependent two-dimensional finite-difference model of solidifying aluminum sheet on copper and found that thicker substrates resulted in shorter solidification times. This is likely due to the chilling effect of the larger thermal mass.

Several coupled models of fluid flow and heat transfer have been developed of strip-casting processes in order to understand the effect of fluid flow on the solidification of the strip in the liquid puddle. Mehrotra and Mallik[34] developed a 2-D steady-state control-volume model of fluid flow and heat transfer for a steel strip caster. It was found that the speed of rotation of the caster wheel and the length of the liquid metal pool strongly affect the process, but the cooling conditions at the inner surface of the wheel only marginally affect the final strip thickness. In addition, the wheel material affects the temperature distribution in the wheel, which was suggested to affect the microstructure[34]. Wu et al[35] developed a 2-D transient SOLA-VOF fluid-flow model to predict the velocity and pressure distributions and to track the movement of the free surfaces of the liquid pool. The results reveal how the melt puddle is formed between the nozzle and the rotating substrate and how changes in process conditions affect the puddle shape, flow and heat transfer behavior[35]. A coupled 2-D model of heat transfer and turbulent fluid flow using k-ε in FIDAP was developed for the aluminum strip-casting process by Moore and Sahai[36],. They assumed a constant interfacial heat transfer coefficient of 10 kW/m^2K and predicted an almost linear strip growth with a final strip thickness of 0.8-2.5 mm at a wheel speed of 0.2-2 m/s. No previous model has coupled the effects of fluid flow and heat transfer in the melt pool with solidification and heat transfer in the strip and transient conduction through the wheel for the melt-spinning process.

2.3. Melt-Pool Model

The metal delivery system affects the melt-spinning process, by controlling the mass flow rate, and delivery of superheat. The first part of the current model simulates fluid flow and heat transfer in the melt pool (Zone I). In addition to understanding the flow dynamics, this model is needed to obtain the heat flux profile applied on the solid-liquid interface of the STRIP1D model in order to account for the superheat entering the solidifying strip from the liquid metal.

A. *Model description*

A two-dimensional steady-state fluid-flow and heat-transfer model was used to obtain the velocity and temperature distribution in the liquid pool by solving the Navier Stokes equations, k-ε turbulence model, and energy balance equations using the SIMPLE finite-volume algorithm with FLUENT. The domain includes the entire length and shape of the liquid pool, which was measured from a video recording of the process. The domain, process, and boundary conditions are shown in Fig. 2a and Table 2.1. Liquid aluminum enters the pool with a velocity of 0.97 m/s at a pour temperature of 714°C (T_{pour}) . The top surface (ceramic wall) of the domain was assumed to be flat with a no slip boundary condition at a constant temperature of 714 °C, owing to continuous contact of the refractory nozzle with the melt. The bottom surface of the domain is the interface between the liquid and the solidification mushy zone. It is maintained at the liquidus temperature of 614 °C (T_{liq}) and moves at a constant speed of 7.02 m/s (v_z) in the casting (z) direction. Because this surface is slightly sloped, (at angle 0.013°) the normal velocity across the interface that accounts for the outlet mass flow (due to solidification) is given by

$$v_N = v_z \sin\theta - v_r \cos\theta \qquad [1]$$

Where v_N is 0.09 m/s for the conditions in Table 2.1. A free slip condition with convection heat transfer coefficient of 10W/m^{2}K was imposed on the free surfaces exposed to the atmosphere.

Parameter	**Validation Case**	**Case 43 (ODSU06_43)**
G	1.5	0.78
PL	23. 3	16.6
V_c	6.23	7.02
t_1	3.74	2.36
s	0.233	0.215
(θ_1, θ_2, θ_3)	(4.39,0,0)	(3.13,15, 343.87)

Table 2.1. Process conditions for different cases

B. ***Model results***

A typical velocity distribution is included in Figure 2.2 (a). The velocity is maximum at the interface and decreases rapidly with distance into the puddle. Figures 2.2 (b). shows the stream function contours which reveal the recirculation zones. Small recirculation regions are observed on both the left and right of the inlet jet. The fluid enters the domain vertically downwards, impinges on the strip and splits. One jet moves towards the left (against the casting direction) and re-circulates back into the pool. As the other jet travels towards the right free surface, its recirculation disappears at around 7mm along the puddle length, whereupon the flow is all in the casting direction. The velocity profile decreases uniformly from the strip towards the free surface. This type of re-circulating flow pattern is typical of melt-pool models[37, 38] In actuality, the free surface oscillates due to the turbulent flow, with a frequency that is proportional to the flow rate[14].

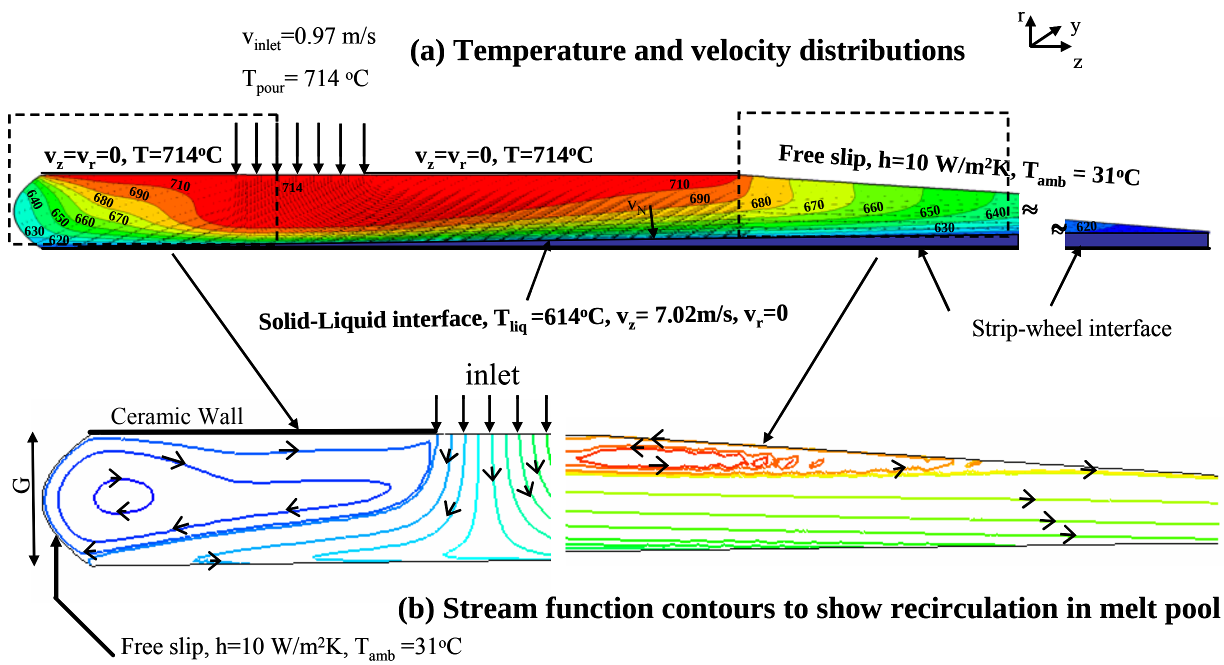

Figure 2.2. Fluid-flow model velocity and temperature distribution in melt pool (sample 43)

The temperature distribution observed in the liquid pool is shown in Figure 2.2 (a). Temperature contours naturally follow the fluid-flow pattern. As expected, a steep temperature gradient is observed near the interface. There is negligible heat gained from conduction from the upper nozzle walls, or heat lost due to radiation away from the surfaces exposed to the atmosphere. The steepest, gradients are found directly beneath the nozzle owing to the hot liquid jet entering the domain. Thus, the superheat flux to the strip is a maximum at the jet impingement point, and decreases with distance on either side. Figure 2.3. shows the heat flux profile output along the interface between the liquid and the solidification mushy zone. This heat flux profile is input as superheat flux into the STRIP1D Model which is discussed in the next section.

The superheat flux is a direct function of casting speed[39], superheat temperature[39], and strip thickness. Assuming that the curve shape is relatively independent of puddle length, the effect of changes to these four casting conditions on the superheat flux can be approximated as follows

$$q_{\sup} = \frac{V_c}{V_{c0}} \frac{\Delta T}{\Delta T_0} \frac{s}{s_0} \frac{l_0}{l} q_{sh} \qquad [2]$$

where v_{c0}, ΔT_0, s_0, l_0 and q_{sh} refer to the casting speed, superheat temperature, strip thickness, puddle length and the superheat flux for the standard fluid-flow simulation. Using Eq. [2], the results for other cases for STRIP1D can be estimated without re-running the fluid-flow model. It is important to note that when Eq. [2] is used to couple the effect of puddle length on superheat flux, each value of q_{sup} obtained for a given distance along the casting direction z_0 is mapped to the corresponding new distance z given by

$$z = z_0 \frac{l}{l_0} \qquad [3]$$

Where z_0 is the distance along the casting direction for the standard flow simulation. Figure 2.3. compares the superheat flux profiles obtained for a thinner strip (0.168mm) using the melt-pool model and with Eq [2] using standard flow simulation results for 0.215mm strip. The heat flux from the actual simulation is higher near the impingement point and lower near the end of the puddle. However, the total area under both curves is the same, so the total heat entering the interface is the same in both cases.

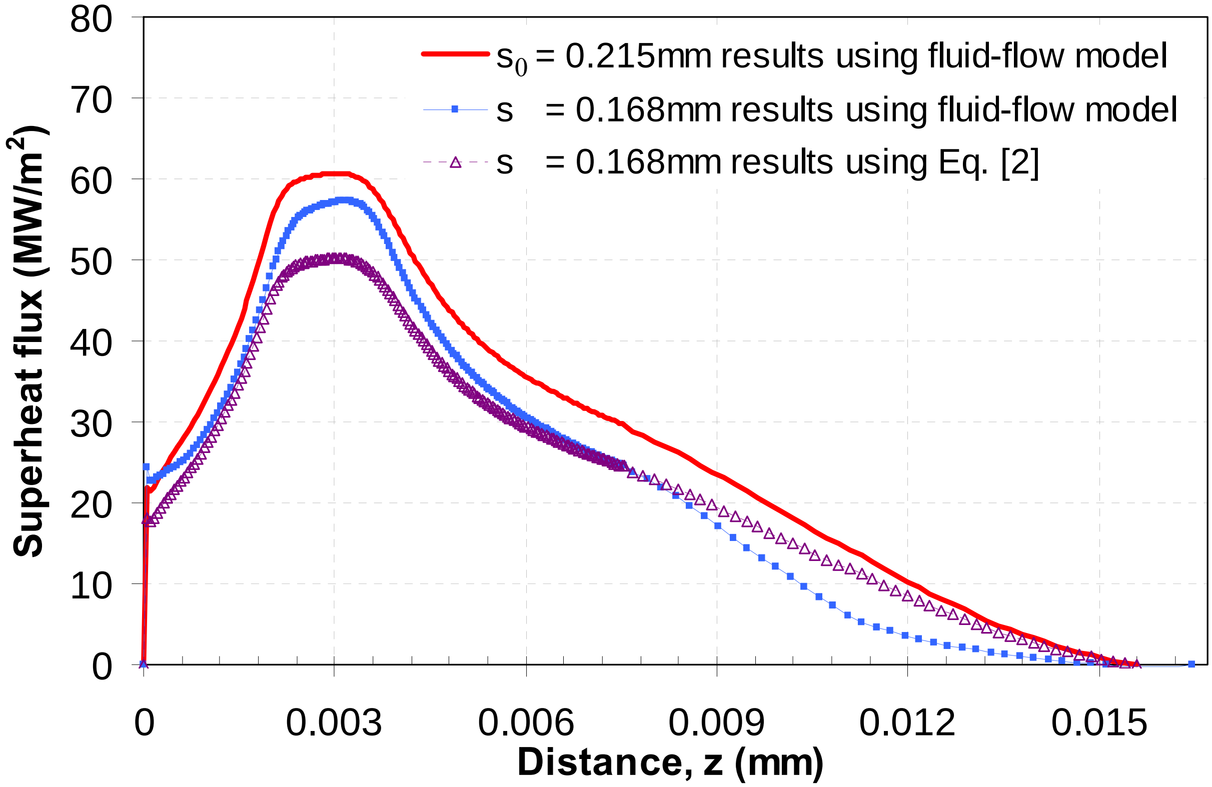

Figure 2.3. Superheat flux profile (sample 43)

2.4. STRIP1D (Strip-Wheel) Model Description:

STRIP1D is a one-dimensional transient heat-transfer model that solves the following Fourier heat conduction equation[12] .

$$\rho c_p \frac{\partial T}{\partial t} = k\frac{\partial^2 T}{\partial r^2} + \frac{k}{r}\frac{\partial T}{\partial r} + \frac{\partial k}{\partial t}\left(\frac{\partial T}{\partial r}\right)^2 + Q \qquad [4]$$

This finite-difference model follows the transient temperature evolution of a one-dimensional slice domain through the strip, and the wheel beneath it, along the casting direction in a Lagrangian frame. Figure 2.4. shows this model domain and the boundary conditions used. The following assumptions have been used to simplify the model.

- The process is at steady state, including the fluid-flow pattern and resulting superheat distribution along the solidification front.

- There is no relative motion between the strip and wheel
- Heat loss across the width of the strip (y direction as in Figure 2.1.) is negligible
- Circumferential heat conduction in both the wheel and strip along the casting direction is negligible, as the Peclet number, Pe, is large.
- Strip thickness remains the same after it exits the liquid puddle at the end of zone I.
- The mushy zone moves with the wheel at the casting speed without any change in shape.

Eq. [4] is discretized using an explicit formulation, as detailed in Appendix [A2] Eqs and [A4]. Thus, the following stability condition must be satisfied.

$$\frac{\Delta t k}{\Delta r^2 \rho c_p} < 0.5 \qquad [5]$$

A time step, *Δt*, of the order of 10^{-9} sec has been chosen for mesh spacing in the strip, *Δr* of 1μm. The wheel is divided into three zones according to θ in Figure 2.1. Zone I is the region where liquid is in contact with strip, so is also known as the "puddle region". In Zone II the solidified strip cools in contact with the wheel and Zone III is after they separate. The boundary conditions in each zone are summarized below for the strip and wheel, and their discretizations are given in Appendix A. A typical simulation of 10 wheel revolutions (2.7s real time) takes 20 min on a Intel Xenon 2.6 GHz PC for a time step size of 10^{-9}s (zone I-II) and 10^{-6}s (zone III) for 250 nodes in the strip and 200 nodes in the wheel.

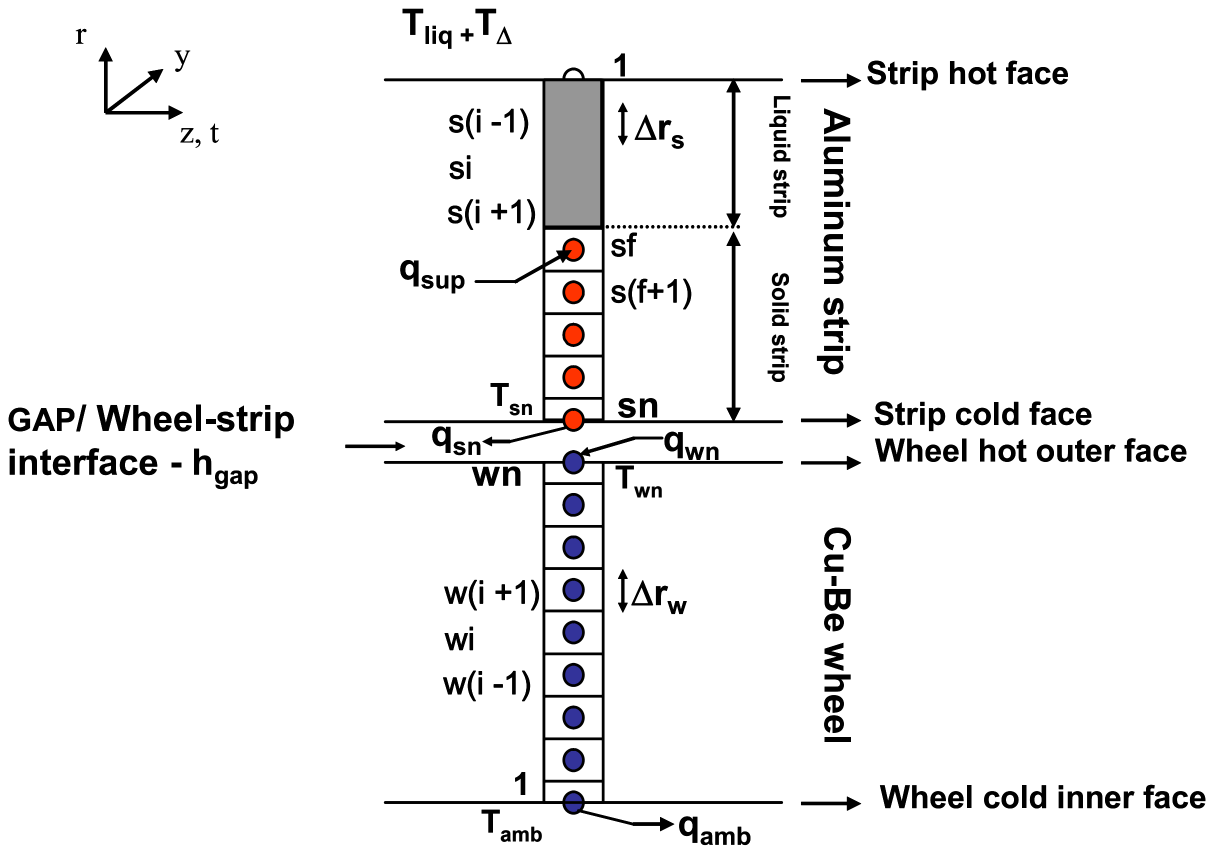

Figure 2.4. 1-D slice domain of STRIP1D model (sample 43)

Zone I (puddle region): In this zone, the solidifying strip moves through the melt pool while in contact with the wheel.

Strip: The melt-pool model described in section 2.3. is used to obtain the superheat flux distribution at the interface between the liquid and the solidification mushy zone.

$$-k_s \left.\frac{\partial T}{\partial r}\right|_{r=s} = q_{\sup} \qquad [6]$$

The solidification front location, s, is determined at any instant, by the following linear interpolation. The liquidus temperature, T_{liq}, was used as the criterion to define the solidification front in the melt-pool.

$$s = f_s x_{sol} + (1 - f_s) x_{liq}$$

[7]

Here x_{sol} and x_{liq} refer to the distance of the solidus and liquidus respectively from the wheel hot outer surface and f_s is the critical solid fraction (0). A thermal convection boundary condition has been applied at the strip-wheel interface.

$$-k_s \left.\frac{\partial T}{\partial r}\right|_{r=r_0} = q_{sn} = h_{gap}(T_{sn} - T_{wn}) \quad [8]$$

Where h_{gap} is discussed in section 2.6., T_{wn} , T_{sn} and r_o are defined in the nomenclature table.

Wheel: The hot outer surface of the wheel experiences convective heat transfer at the interface and the cold inner surface is exposed to ambient cooling.

$$q_{wn} = -q_{sn} \quad [9]$$

$$q_{amb} = h_{amb}(T_{w1} - T_{amb}) \quad [10]$$

Where T_{w1} is the temperature at the inner surface of the wheel. The ambient heat transfer coefficient (h_{amb}) of 25W/m^{2}K has been estimated using the empirical relation established for flow over a cylinder[40] as explained in Appendix B Eq**s**. [B1] to [B3]. Also taken to account is heat loss Q_{sides} from wheel sides due to convection. This is done by treating the convective heat transfer as a heat source removal from within the wheel. See Appendix B, Eq [B4] for calculations.

Zone II (Strip cooling zone): In this zone, the mushy or solidified strip is outside the melt pool but still in good contact with the wheel. Thus, this region employs the same function for heat transfer coefficient h_{gap} for q_{sn} or q_{wn} as in Zone I at the wheel-strip interface given by Eqs [8] and .[9]. Zone II ends when the strip becomes fully solid and thereby gains the necessary strength to break off from the wheel, due to mismatching thermal strains.

Strip: The strip is outside the liquid pool so its thickness is constant and its upper surface is exposed to ambient cooling

$$q_{sf} = (h_{amb} + h_{rad,sf})(T_{sf} - T_{amb}) \quad [11]$$

Wheel: The wheel experiences the same boundary conditions as in Zone I given by Eqs. [9] and [10].

Zone III (Non-contact Zone): After exiting Zone II, the parts of the domain representing the solid strip and the wheel are mathematically separated. Thus, this zone consists of the rest of the wheel and the detached portion of the strip.

Strip: The detached strip is exposed to atmosphere on both sides, where forced convection and radiation are applied:

$$q_{sn} = (h_{amb} + h_{rad,sn})(T_{sn} - T_{amb}) \quad [12]$$

$$q_{sf} = (h_{amb} + h_{rad,sf})(T_{sf} - T_{amb}) \quad [13]$$

where, $h_{rad,sn} = \varepsilon\sigma_{SB} (T_{sn}^2+T_{amb}^2)(T_{sn}+T_{amb})$ *and* $h_{rad,sf} = \varepsilon\sigma_{SB} (T_{sf}^2+T_{amb}^2)(T_{sf}+T_{amb})$.

Wheel: Both surfaces of the wheel undergo ambient cooling.

$$q_{wn} = h_{conv}(T_{wn} - T_{amb}) \quad [14]$$

The complete history of a slice through the strip is simulated once each wheel revolution. The simulation continues for any desired number of cycles, during which the wheel continuously heats up.

2.5. Superheat Flux Method and Validation

As discussed in Section 2.3, the melt-pool model is used to obtain the superheat flux profile along the interface between the liquid and the solidification mushy zone. This profile is input into STRIP1D to incorporate the effect of the superheat on the strip temperature evolution and solidification, instead of letting the superheat simply conduct through the liquid. The superheat flux can be treated like an internal heat flux boundary condition given by Eq [A17], as applied in previous work[12]. In the "superheat flux method" of the current work, superheat flux was treated as a heat source added to the closest node below an internal insulated interface (liquidus temperature) as given by Eq [A15]. The initial temperature of the domain is dropped to $T_{liq}+T_{\Delta}$, so that superheat is taken into account only by the imposed superheat flux profile. Using the theoretically best value of T_{Δ} of 0.0 has the undesirable numerical consequence of inaccurate interpolation of the position of the solidification front. A post-iterative correction is finally made to all nodal temperatures above the liquidus temperature by reassigning them back to $T_{liq}+T_{\Delta}$.

In order to validate this method, a simple "validation case" was performed with conditions listed in Table 2.1., and also compared with results using ABAQUS. The fluid-flow model, shown in Figure 2.5., was simplified to constant initial temperature (T = 714^{o}C) fluid moving with the strip along z direction at a constant velocity (6.23 m/s). This is equivalent to the assumptions made with a transient model (ABAQUS or STRIP1D) formulated in a Lagrangian frame with simple conduction through the superheated liquid. Using a fixed temperature (614^{o}C) lower boundary condition, the superheat flux crossing the liquid-mush interface to enter the strip calculated using FLUENT for this case is given in Figure 2.6.

Transient conduction simulations were then performed with both STRIP1D and ABAQUS using a domain height of 1.5mm. Results using both constant thermo-physical properties and realistic temperature-dependent properties for this alloy (Figures 2.7., 2.8., 2.9.)[41] were compared using ABAQUS. Figure 2.10 (a). shows a match in the solidification front growth between STRIP1D and ABAQUS using simple conduction in the liquid.

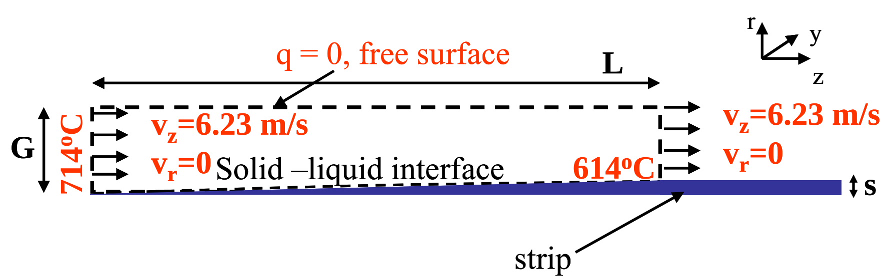

Figure 2.5. Fluid-flow Model Domain– (validation case)

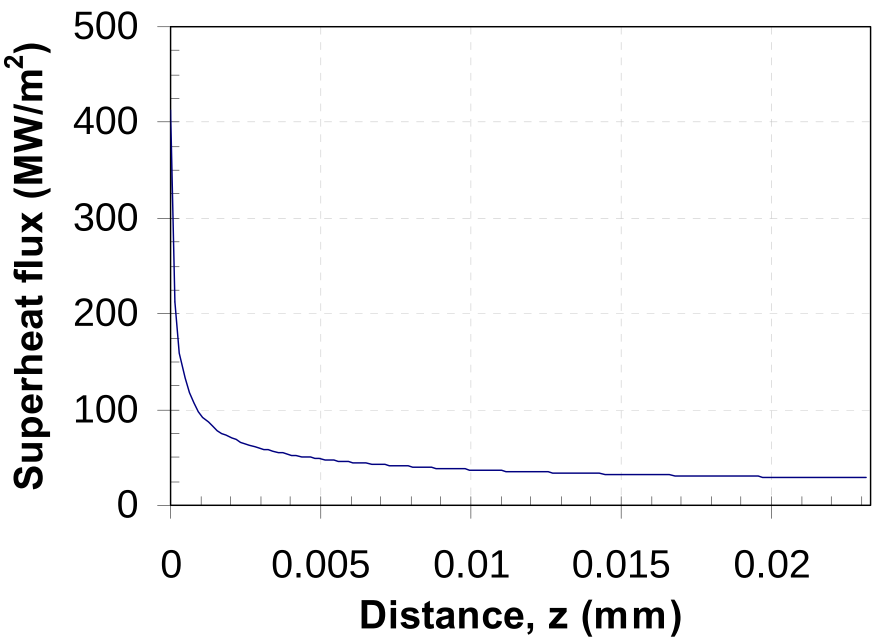

Figure 2.6. Superheat flux profile – (validation case)

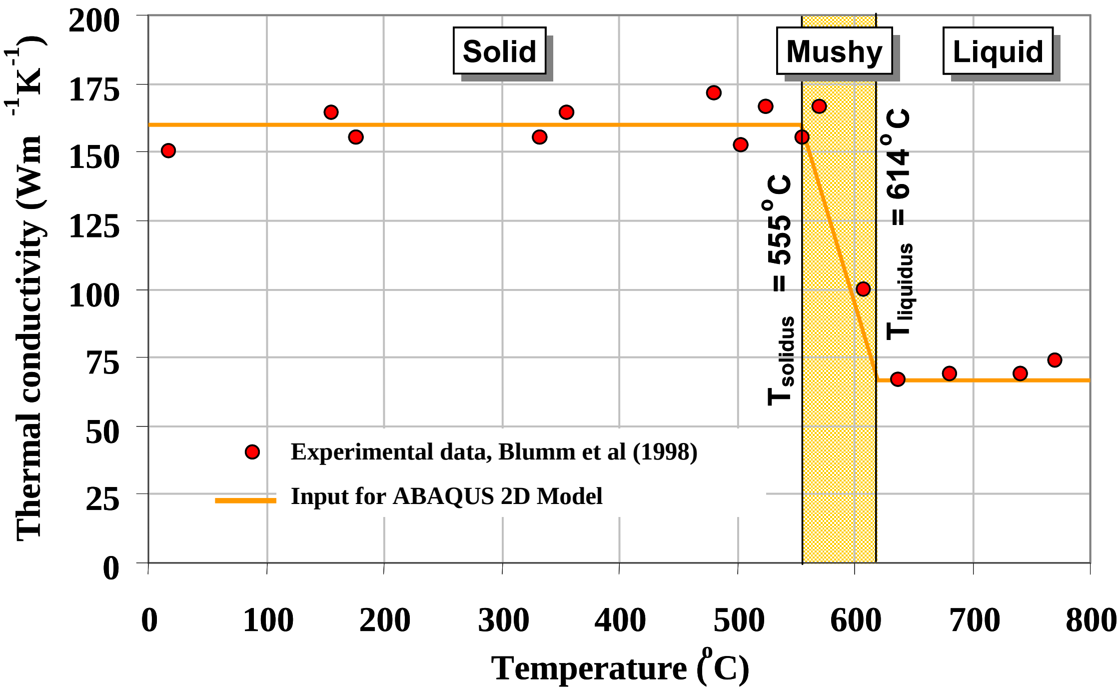

Figure 2.7. Temperature dependent thermo-physical properties (conductivity)

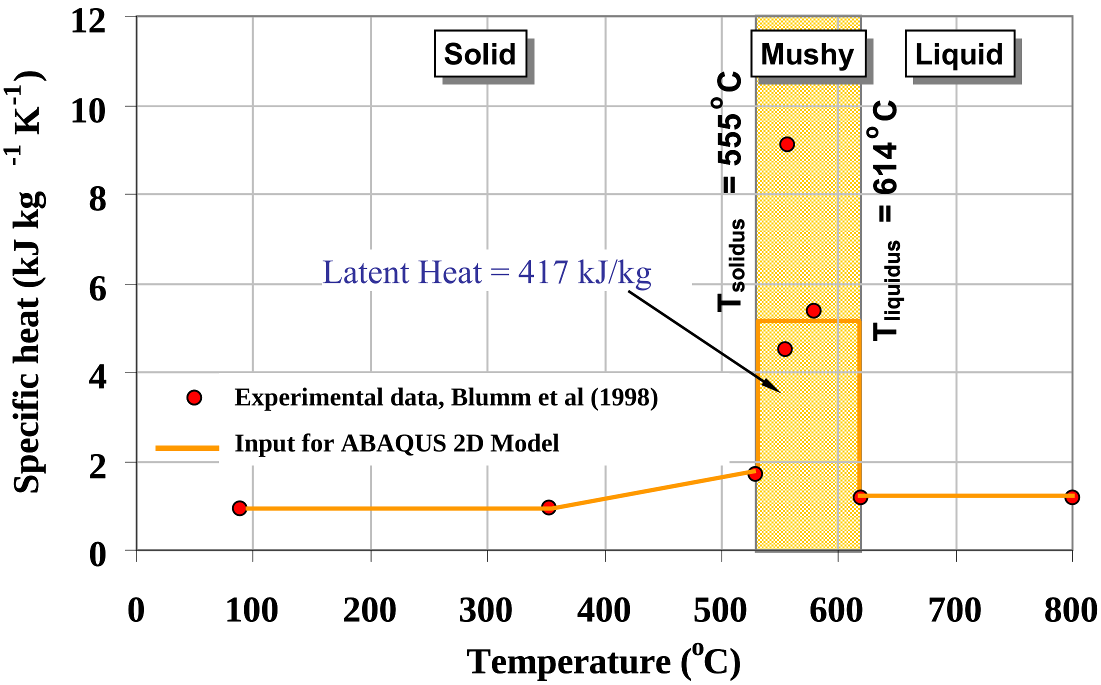

Figure 2.8. Temperature dependent thermo-physical properties (specific heat)

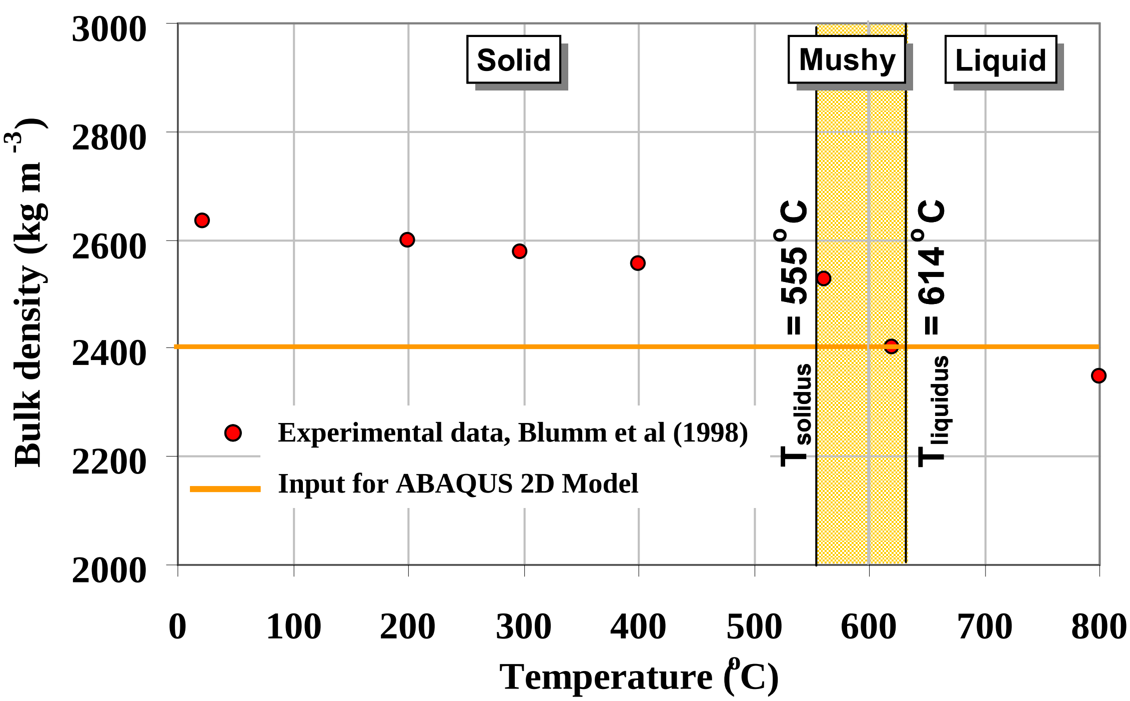

Figure 2.9. Temperature dependent thermo-physical properties (density)

This shows that the choices of constant thermo-physical properties for this alloy are reasonable.

Figure 2.10 (a). also shows a match in the solidification front growth profiles obtained from STRIP1D using the superheat flux method and the simple conduction method. Fig 2.10(b). shows that the superheat flux method generates the same strip growth profile for different domain heights, ranging from 0.25 to 1.5 mm. This figure also shows the effect of increasing T_Δ. Increasing T_Δ initially decreases the strip thickness, but the effect diminishes for T_Δ greater than 3. An increase in T_Δ naturally decreases the strip thickness, owing to the increase in superheat, but this error is small. The heat balance in Table 2.3. indicates that the superheat contributed by T_Δ of 1 is only about 0.2% of the total heat extracted from the strip. Of greater importance is that increasing T_Δ also decreases the numerical error associated with interpolating the liquidus contour. A value of 3.0 for T_Δ was judged to achieve the best accuracy.

Figure 2.11. shows a near-perfect match in the temperature distribution through the thickness of the strip at specific times for the STRIP1D and ABAQUS models using either the simple conduction or the superheat

Table 2.3. Heat Balance for STRIP1D at exit of zone II -Validation case and Case 43-cycle 3

Parameters	**Simple Conduction (validation case)**	**Superheat flux method (validation case)**			**Superheat flux method (Case 43)**
Gap (mm)	1.5	1.5	0.25	0.25	0.25
Delta		3.0	1.0	3.0	3.0
Total Heat going to wheel (KW/m)	2104.9	2110.88	2097.41	2111.11	2067.27
Superheat flux into the strip (KW/m)	0	1071.61	1071.61	1071.61	427.84
Superheat (KW/m)	1072	11.97	4.14	11.97	11.97
Latent heat (KW/m)	862.19	874.74	884.77	874.29	1439.76
Sensible heat from strip (KW/m)	172.05	175.39	178.37	175.26	249.29
Strip thickness (mm)	0.232	0.224	0.232	0.224	0.215
Error	-0.08%	-1. 08%	-1.98%	-1.04%	-3.03%

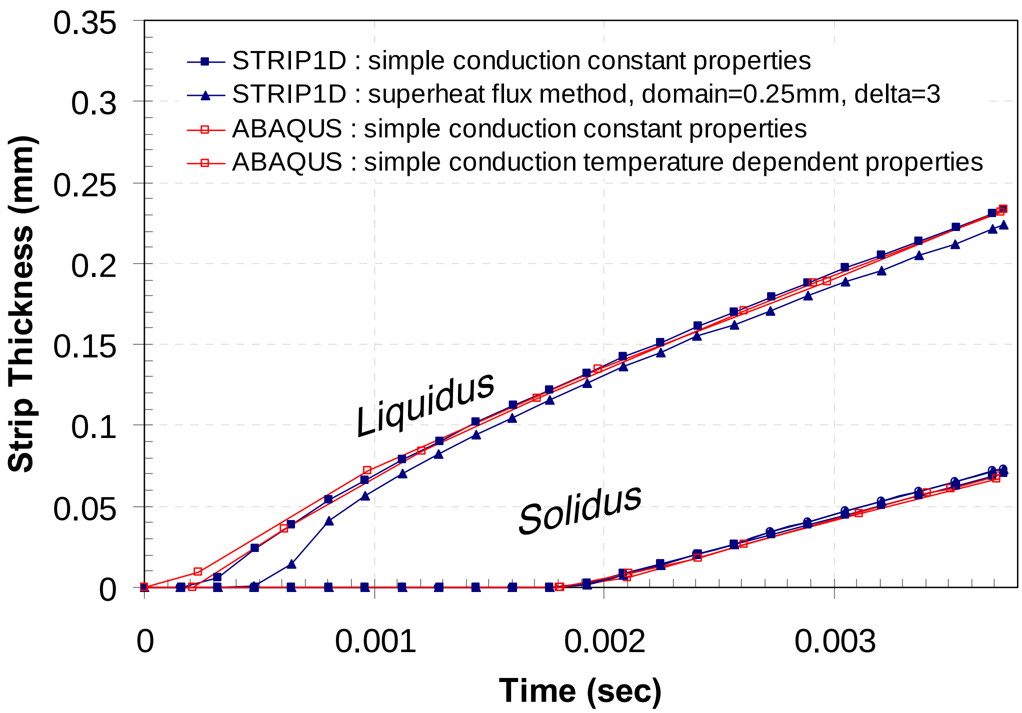

Figure 2.10. (a) Shell growth vs. time- (validation case)

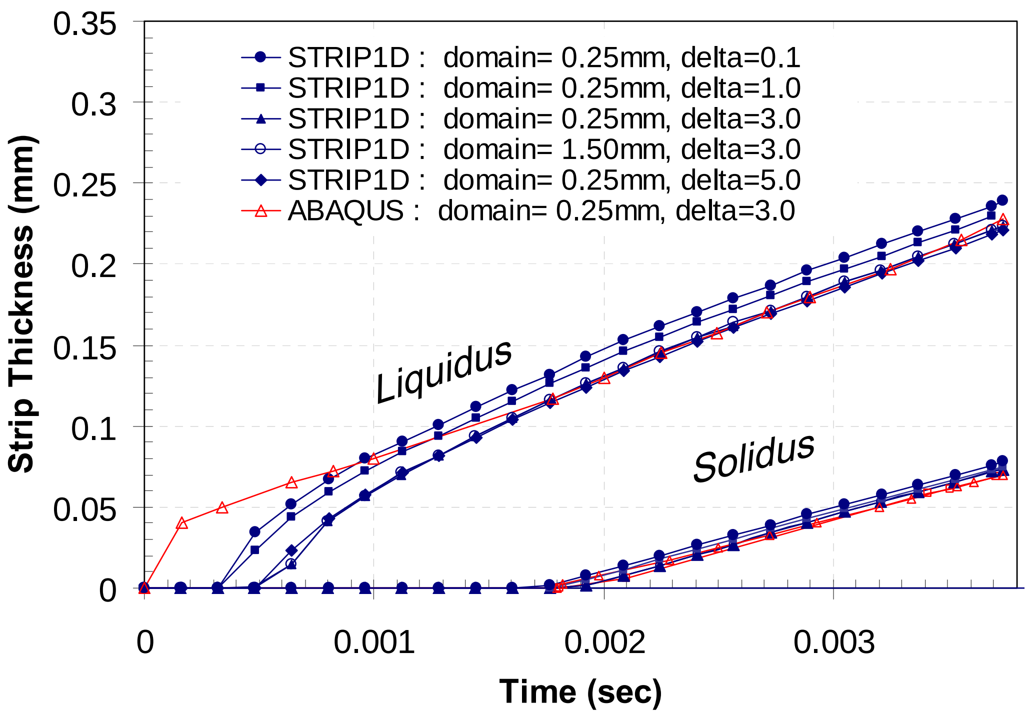

Figure 2.10. (b) Shell growth vs. time- (validation case)

flux methods. Notice that the superheat flux method fixes temperatures in the liquid to just above the

liquidus temperature (T_{liq}+T_{Δ}), so are not expected to match the simple conduction method in the liquid where the initial temperature is T_{pour}. These results demonstrate that the superheat flux method is valid and can be used to couple the effect of fluid flow in the melt pool with heat transfer in the strip and wheel.

2.6. Heat Transfer Coefficient h_{gap} in Strip-Wheel Contact Zone

The heat transfer coefficient in the wheel-strip interface is the most critical parameter which governs the conduction of heat from the strip through the wheel. As reviewed in Section 2.2., several studies have been made to quantify the heat transfer coefficient in the contact region for melt-spinning applications[24-28] . Initial contact between liquid and solid is nearly perfect and produces very high heat transfer. Very quickly, the contact condition at the interface gradually drops, due to the gradual formation of gas pockets, imperfections, thermal contraction of the solid, and other phenomena related to gap formation.

According to many researchers[15-18], the heat transfer coefficient decreases with the time from the meniscus. In this work, the following time-dependent empirical relation for h_{gap} has been adopted from the past work of Li and Thomas[12].

$$h_{gap} = \left\{ \begin{array}{ll} h_0 & t \le t_0 \\ h_0 \left(\dfrac{t_0}{t} \right)^m & t_{\det ach} > t > t_0 \end{array} \right\} \qquad [15]$$

A value of 1/3 was chosen for m and 0.1 ms for t_0. The low value of t_0 indicates that the time of perfect liquid contact is very short, and is consistent with previous estimates of the undercooling time[4].

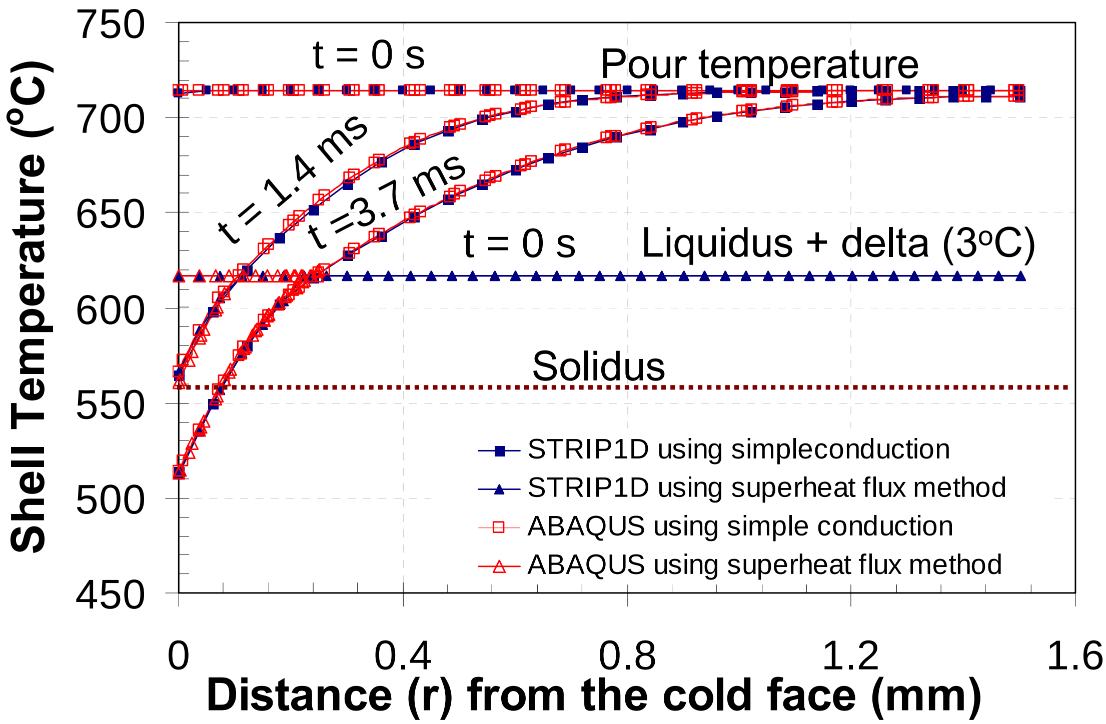

Figure 2.11. Temperature profile along shell thickness over time- (validation case)

Experimental measurements, such as shown in Figure 2.12., indicate that the gap height varies with time during the cast in two time scales[10]. The gap generally decreases with number of cycles, due to overall
thermal expansion of the wheel as it heats up. The gap also varies within each cycle, owing to its not being perfectly circular. A decrease in gap height is believed to cause a decrease in heat transfer coefficient. This is because decreasing the gap height causes liquid in the puddle to oscillate more violently and with higher frequency[2]. More rapid fluctuation of the meniscus thus decreases the contact between the liquid and the substrate at the interface, and encourages the formation of gas pockets and other interfacial imperfections. This decreased contact is expected to decrease the heat transfer coefficient. This effect has been empirically calibrated using Eq. [16].

$$h_0 = 225G \qquad [16]$$

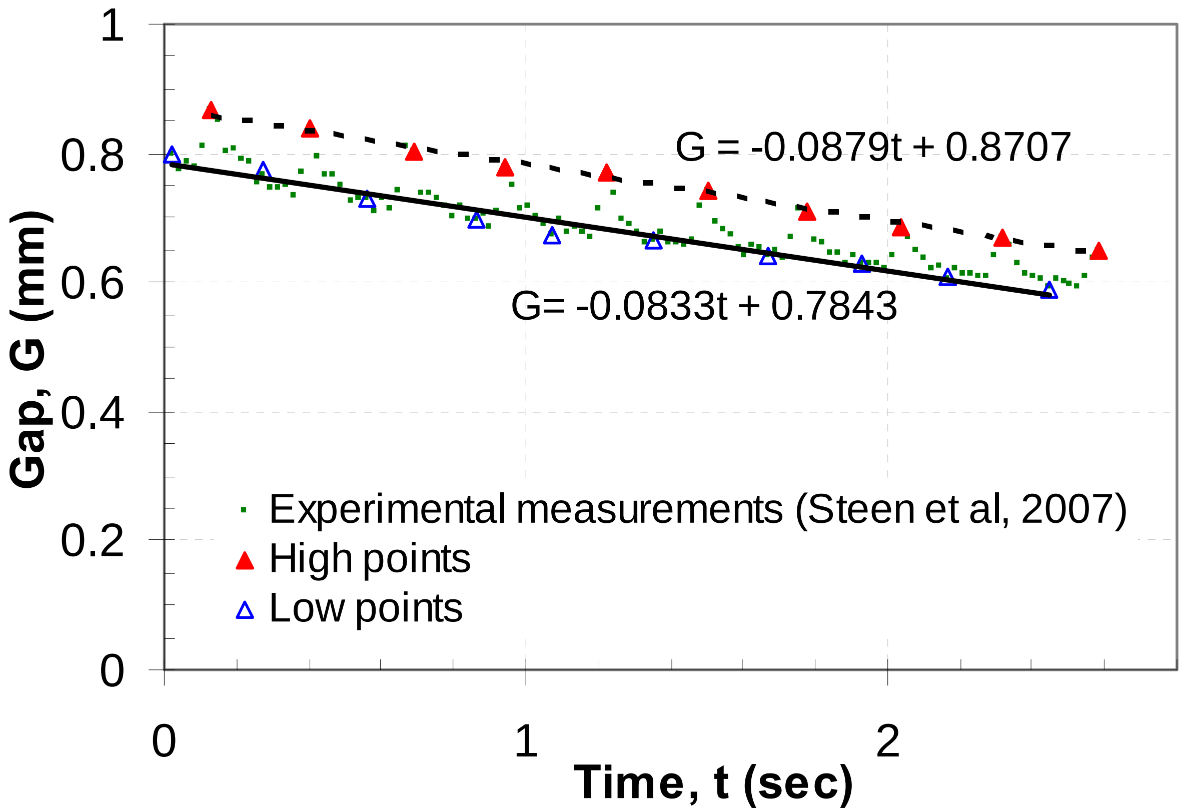

Figure 2.12. Measured Gap height history – (sample 43)

The heat flux profile obtained from the simulation for cycle number 3 using Eq. [15] and [16] (h_0 = 165 kW/m^{2}K) is shown in Figure 2.13. This profile matches well with the extrapolated line through the measurements made by Birat et.al[17] and is within the range of experimental heat flux values measured by Blejde and Mahapatra at Castrip LLC[18] for the steel strip-casting process. The average heat transfer coefficient in Zone I can be computed using Eq. [17]

$$h_{avg} = \frac{1}{t_1}\int_0^{t1} h_{gap} = \frac{h_0 t_0}{t_1}\left[1 + \frac{1}{1-m}\left\{\left(\frac{t_0}{t_1}\right)^{1-m} - 1\right\}\right] \qquad [17]$$

This equation gives a value of 110 kW/ m^{2}K for t_1 = 2.36 ms which matches with the value reported by Kukura and Steen[26].

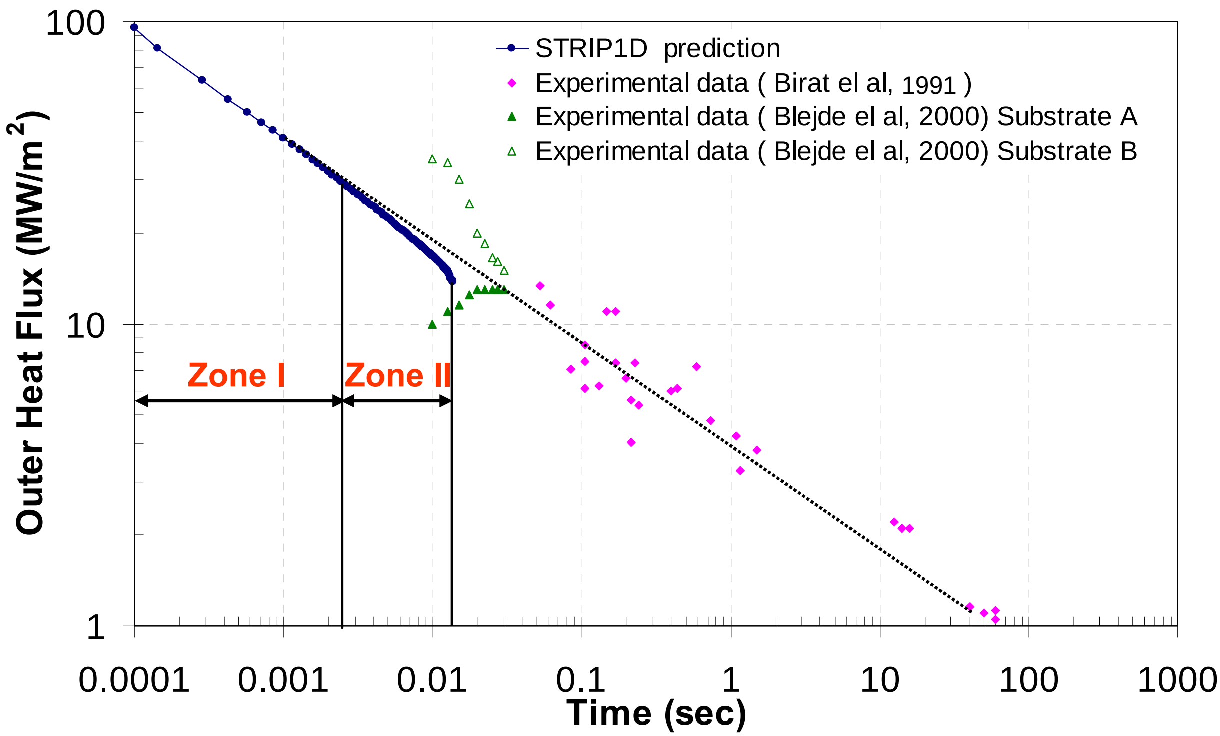

Figure 2.13. Heat flux profile entering the wheel in Zones I &II – (sample 43)

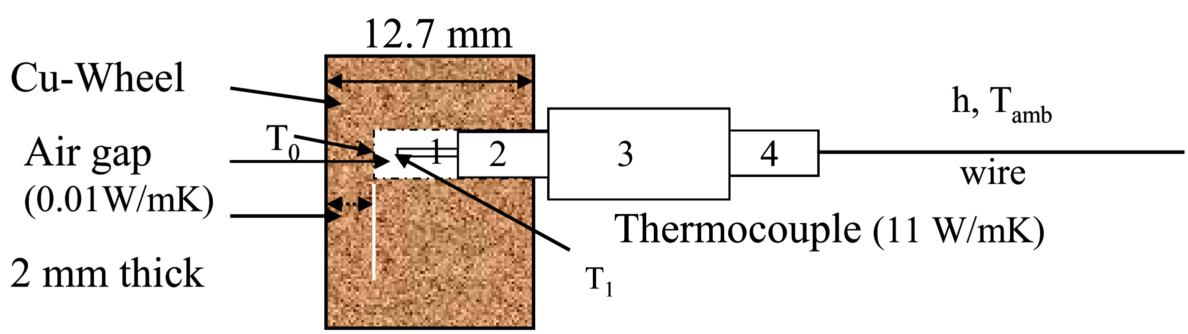

Figure 2.14. Resistor treatment given to TC embedded in the wheel

2.7. Effect of Thermocouple (TC) in Wheel

The wheel temperature was experimentally measured[10] using a K-TYPE Fast response thermocouple (TC) which was embedded 2mm below the outer wheel surface. However, the TC may not perfectly contact the wheel. This causes a thin air gap between the substrate and the TC, which resists the heat flow to the thermocouple, lowering the recorded TC temperature. In order to model this, the TC has been treated as a set of resistors as shown in Figure 2.14., including an air gap of 1μm. This same thickness was chosen for all simulations and may be considered as a parameter that incorporates all modeling and experimental errors, including neglect of 3-D conduction effects near the TC hole. A relation between the predicted TC temperature, T_1, and the adjacent wheel temperature, T_0, has been obtained. See Table 2.2 and Appendix B3, Eq**s** [B6] and [B8] for details.

$$T_1 = 0.89T_0 + 0.11T_{amb} \quad [18]$$

2.8. Model Results and Validation

The model thus calibrated has been validated with experiments conducted at Cornell University[10]. Case 43 (Cast ID # ODSU06_43) was chosen to verify the model predictions. The experimentally observed trends for the gap height, *G* with time of cast, *t* in Figure 2.12. were used to vary the heat transfer coefficient with gap height using Eq. [16]. Owing to fluctuation in the observed data, two sets of gap data, highs and lows of the data points, were chosen separately and a line of fit was drawn through them. The highs and lows of the puddle length were used as shown in Table 2.4.

Table 2.4. Measured process parameters against model predictions.

Cycle number	**Measured gap thickness (mm)**		**Measured puddle length (mm)**		**Measured strip thickness (mm)**		**HT coefficient (kW/m^2 K)**		**Predicted strip thickness (mm)**	
	High	Low	High	Low	High	Low	High	Low	High	Low
1	0.867	0.798	22.0	18.8	0.228	0.215	195.1	179.6	0.226	0.215
2	0.838	0.776	22.0	18.7	0.225	0.210	188.5	174.6	0.219	0.206
3	0.803	0.730	18.9	16.9	0.215	0.203	180.6	164.3	0.214	0.205
4	0.778	0.697	17.4	16.7	0.212	0.197	175.0	156.8	0.211	0.198
5	0.769	0.674	17.3	16.8	0.207	0.195	172.9	151.7	0.206	0.196
6	0.744	0.666	17.1	16.6	0.202	0.190	167.3	149.9	0.202	0.190
7	0.708	0.642	16.9	16.4	0.198	0.186	159.2	144.5	0.198	0.186
8	0.685	0.630	16.4	16.1	0.192	0.181	154.2	141.8	0.193	0.181
9	0.670	0.609	16.5	15.8	0.185	0.175	150.8	137.1	0.189	0.177
10	0.649	0.590	17.0	16.1	0.154	0.148	146.0	132.8	0.184	0.171

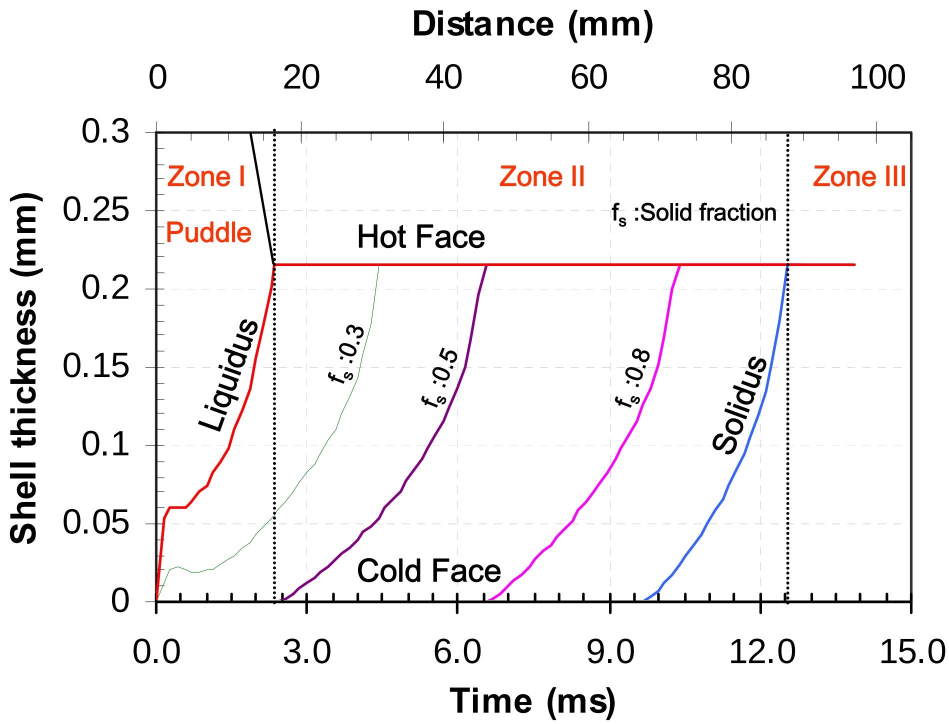

Figure 2.15. Solidification front growth

Table 2.2. Resistance treatment given to TC

Parameter	**Air gap**	**Part 1**	**Part 2**	**Part 3**	**Part 4**	**Wire**
Length (mm)	0.001	2.27	0.13	0.13	0.119	Infinite
Diameter (mm)	0.8	0.8	2.0	7.2	2.0	1.63
Resistance l/kA (K/W)	199	410	376	29	345	587

A. *Solidification front growth:* The predicted solidification front profile in Zones I &II is shown in Figure 2.15. Without undercooling, solidification starts at 1μs and increases rapidly. The predicted front growth slows beneath the jet impingement region, and then increases sharply as the superheat diminishes. The temperature contours for different solid fractions in the strip have a similar steep shape and are almost parallel to each other. This logical but nontraditional profile agrees with the solidification front growth reported by Chen et al[4]. The liquidus reaches the top surface in 2.36 ms from the start of contact at the meniscus, and the solidus after 13.6 ms. This long delay is due to the lower heat transfer rates predicted at greater times by Eq. 15 (see Figure

2.13.). The extensive mushy region is predicted to persist well past the end of the liquid pool. The strip is proposed to detach from the wheel (end of Zone II) at ~87mm when it fully becomes solid and gains the necessary strength to break off from the substrate surface.

B. *Strip thickness:* Figure 2.16. shows excellent agreement in the strip thickness between the model predictions and the experimental observations[10] and captures the observed variations in two different time scales. The overall decreasing trend in strip thickness profile can be attributed to two main reasons. Firstly, because the gap height generally decreases with time, the heat transfer coefficient decreases from Eq. [16]. Secondly, because the wheel temperature increases each cycle, less heat flux is extracted (from Eq. [8]). A third minor contributing reason is the decrease in puddle length with time, which is caused by flow resistance associated with the decreased gap (see Table 2.4.). This shortens the time available for solidification, so tends to decrease the strip thickness. However, after cycle 4, the puddle length remains almost constant while the strip thickness drops significantly. The effect of puddle length is incorporated in the predictions, but turns out to be small.

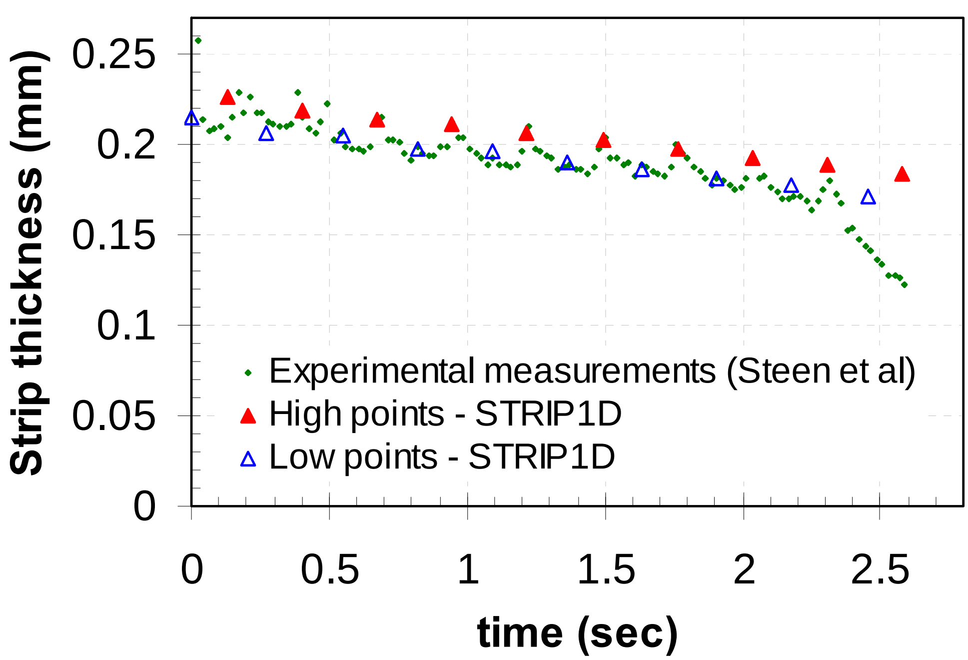

Figure 2.16. Measured & Predicted strip thickness history – (sample 43)

It is interesting to note periodic glitches in the measured strip thickness within each cycle, which are represented by selected high and low points. These are caused mainly by the periodic variations in measured gap height (Figure 2.12.) owing to the oblong wheel shape. Bulges on the wheel form a low measured gap beneath the nozzle and the depressions form a high gap. According to Eq.[16], the heat transfer coefficient varies and generates a similar trend in the observed strip-thickness profile. Again, the measured puddle length also drops from high to low points, but its effect is less important.

The predictions do not match well with the thicknesses measured during the start and end of the process. This is because the empirical relation developed between the gap height and the heat transfer coefficient given by Eq. [16] does not hold well during these times. Once the process begins, it takes some time for it to stabilize and reach steady state. During the end of the casting process, the pressure head of the melt in the crucible drops, which lowers the liquid flow rate, and decreases the strip thickness, in order to satisfy the mass balance. However, this is accompanied by an unexpected increase in the measured puddle length, so the interfacial heat transfer must drop, in order to satisfy the heat balance. This might be due to chaotic flow variations, wheel surface contamination, or other reasons.

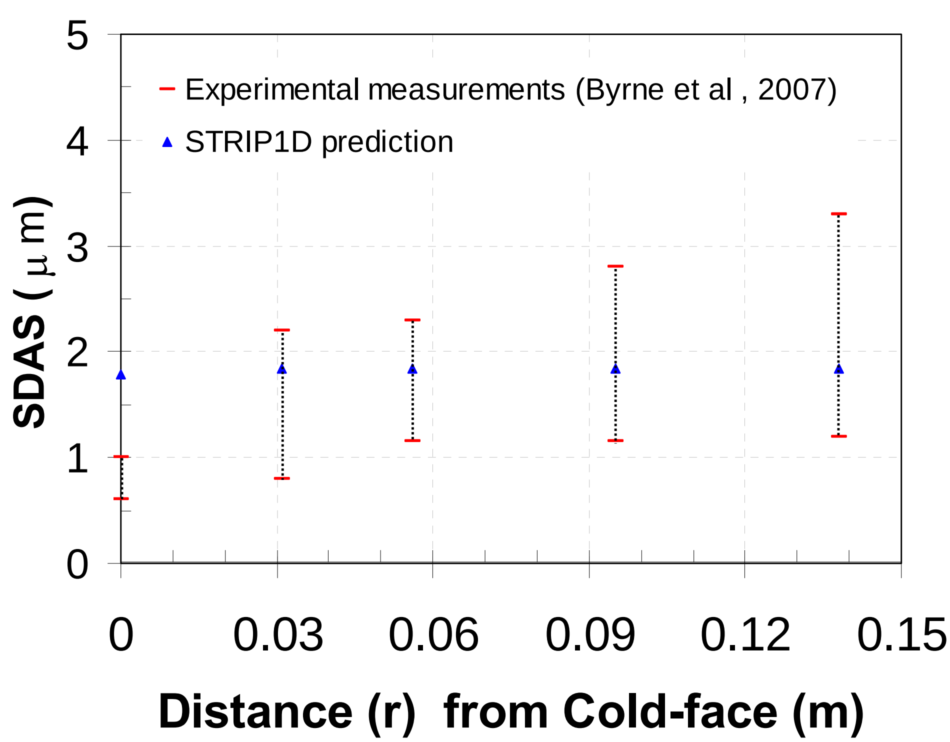

Figure 2.17. Measured and predicted SDAS through the strip thickness (sample 43)

C. *Solidification velocity, cooling rate, and microstructure:* The velocity of the solidification fronts is simply the average slope of the liquidus and solidus lines in Figure 2.15. Velocities of 0.082 m/s (liquidus) and 0.078 m/s (solidus) lie within the range of 0.05 -0.1 m/s reported by Byrne et al[2]. The liquidus grows at a faster rate than the solidus because the heat transfer coefficient decreases along the casting direction according to Eq. [15].

The time difference between solidus and liquidus from Figure 2.15. was used to obtain the solidification time t_{sol} at various thicknesses through the strip. The obtained solidification time t_{sol} can be used to determine the cooling rate (CR) by

$$CR = \frac{(T_{liq} - T_{sol})}{t_{sol}} \qquad [19]$$

The top surface and interface have similar cooling rates, owing to the high conductivity and thin strip of this process. The predicted cooling rates of 5800-6000 deg/sec are on the same order as the average cooling rates reported by Byrne[42] using Bamberger's model[43].

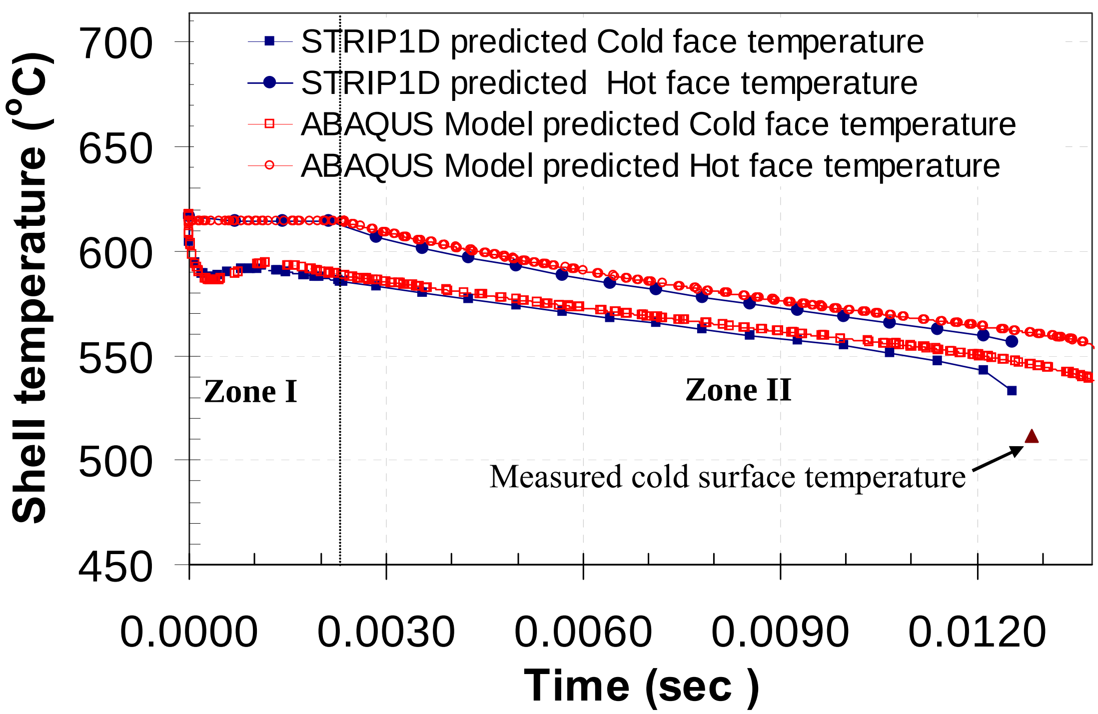

Figure 2.18. Strip surface temperature profiles (sample 43)

The solidification times can also be used to predict the SDAS of the microstructure, λ, using an empirical relation developed by Spinelli[44].

$$\lambda = 5(4.9t_{sol})^{0.333} \qquad [20]$$

Figure 2.17. compares the predicted and measured SDAS at various locations through the strip. Because the conditions of the experiments were different[42], and the model does not take into account the nonlinear dependency of latent heat on the solid fraction, a perfect match between SDAS predictions and measurements is not expected

D. *Strip surface temperatures:* Figure 2.18. shows the temperature history at the strip hot and cold faces. The predicted cold-face surface temperature profile has a small dip in zone I. This indicates reheating, but is not due to either nucleation undercooling[45] or sudden drops in interfacial heat flux[46] which have been observed in other work. Here, the reheating is attributed to the peak superheat flux at the region of jet impingement, as discussed in section 2.8.A.

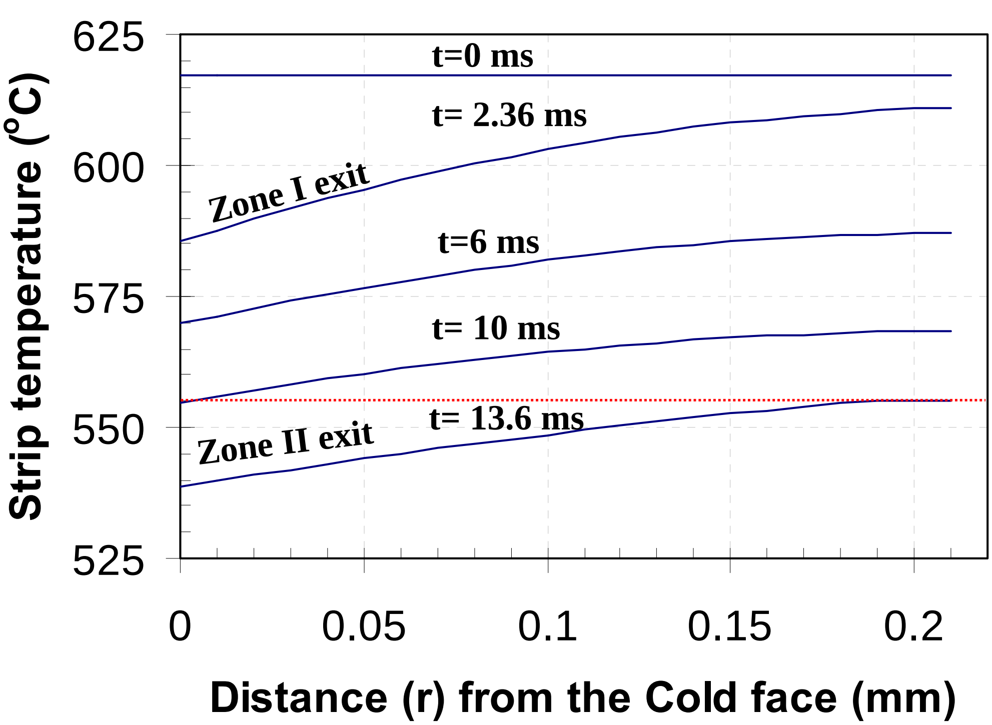

Figure 2.19. STRIP1D predicted temperature profile through shell thickness over time (sample 43)

The predicted strip hot and cold face temperature profile is in great agreement with that obtained from the ABAQUS model. It is clear that the predicted cold face temperature of the strip at the exit of zone II (detachment) of 537°C is within 5% of the experimentally measured exit temperature of 512°C. The prediction is expected to be higher because the exit temperature can be experimentally measured only after a few seconds after the strip leaves the wheel. Figure 2.19. shows the temperature through the thickness of the strip at various times in Zones I and II. Temperature gradients through the strip thickness are relatively small, as the center cools within 20°C of the surface after only 13.6ms.

E. *Heat balance:* Table 2.3. provides a detailed heat balance for cycle 3 of this simulation, case 43. The total heat flux extracted from the strip (and entering the wheel) is calculated by integrating Eqs. [8] and [9] until the end of zone II. This total heat flux is the sum of the superheat, latent heat and the sensible heat. The latent heat comprises around 68% of the total while the superheat and sensible heat contribute 20% and 12% respectively. These fractions are consistent with other work on strip casting[21, 26]. Owing to numerical errors, the sum of these three parts is 3% more than the total, which indicates the accuracy of the computation.

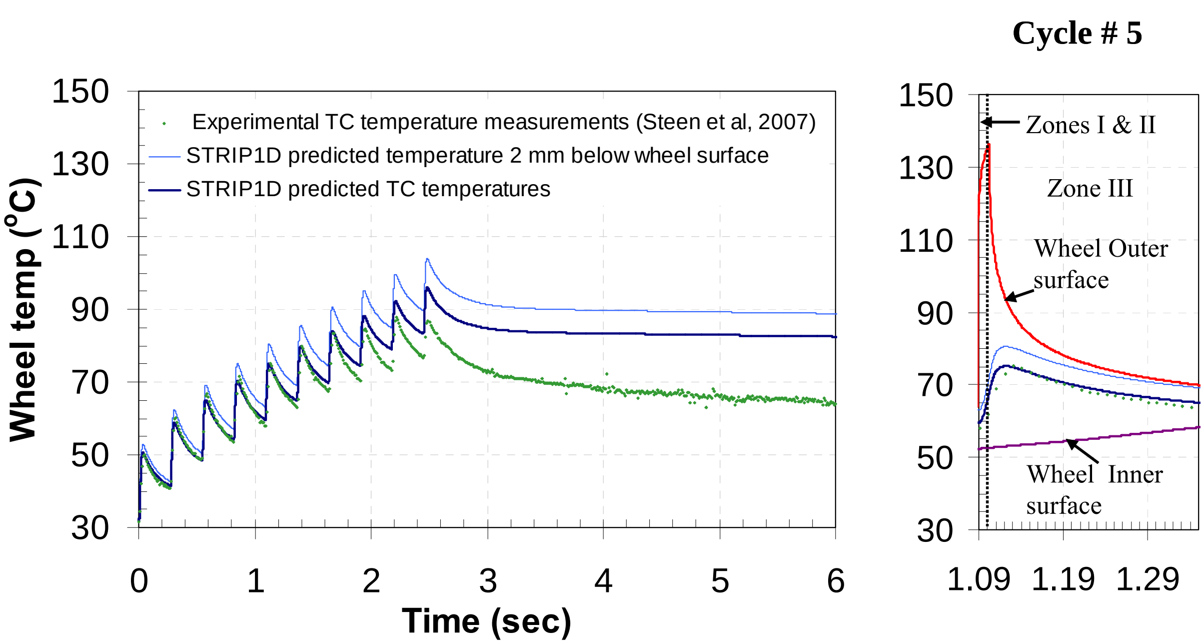

Figure 2.20. Measured & Predicted wheel TC temperature history (sample 43)

F. *Wheel temperatures:* To evaluate the wheel temperature predictions, the temperature profile 2mm below the wheel surface was used to predict the thermocouple temperature using Eq [18] . The results in Figure 2.20. show excellent agreement with the experimental measurements for all ten casting cycles.

The wheel heats up each cycle and never reaches steady state. The hot face where heat is input naturally reaches high temperatures very fast. Heat is extracted from the strip mainly by the cold thermal mass of the wheel, which heats up monotonically only a little each cycle. The increase in wheel temperature decreases with each passing cycle because the initial heat transfer coefficient h_0, decreases with cycle from Eq.[16], owing to the general decrease in gap height during the cast. Because air cooling of the wheel is very small, there is a limit to the number of cycles possible before the wheel becomes too hot to solidify any strip.

The STRIP1D predicted wheel temperatures match well with the measurements while the strip is contact with the wheel. During this time, there are steep temperature gradients in the wheel and only the surface layer of the wheel is heated (see Figure 2.20.). The wheel acts almost like a semi-infinite domain and its thickness is not very important. Once there is no more metal-substrate contact, however, internal temperature gradients subside as the wheel undergoes only ambient cooling. The predicted temperature no longer matches the TC measurement. This is because the heat transfer coefficient during this period (h_{amb}) is very small (25 W/m^2K). This drops the Biot number, internal temperature gradients subside, and the wheel behaves as a lumped system. The cooling rate in this regime increases in cases of less thermal mass. Since the thickness of the wheel near the thermocouple is only 2mm thick (owing to the hole drilled to place the thermocouple), the cooling rate near that region increases. This results in a faster rate of cooling measured by the thermocouple, relative to elsewhere in the wheel. Thus, the predictions are no longer expected to match the measurements.

2.9. Conclusions

This chapter presents a simple, yet accurate numerical model of the planar-flow melt-spinning process for Al-7%Si alloys. This model includes a realistic treatment of fluid flow and heat transfer in the melt pool, coupled with transient heat transfer and solidification of the strip and transient heat conduction within the wheel. Simultaneous predictions of transient strip thickness, SDAS, cooling rate, strip surface temperature and transient wheel temperature have been validated using experimental data measured at Cornell and excellent agreement has been observed.

3. Parametric Studies and Modeling Surface Defects

3.1. Introduction

Melt-spinning process[8, 9] can be used to cast amorphous metallic glass ribbons[7, 38] or thin metal strips[25] with fine microstructure and properties[2, 3, 24]. With cooling rates of 10^3-10^6 K/s , this is a rapid solidification process[24] Previous research on strip casting and melt spinning and a detailed description of the single roll melt-spinning process is given in Chapter 2 of this work. The strip produced during this process has several different types of observable surface defects [33, 47, 48]. These include cracks, holes, hot tears, segregation and surface depressions [33, 47, 48]. Steen et al[49-51] have suggested that if the surface depressions can be controlled, this method could be an economical way to produce strip product with textured surfaces embossed with text and images. Figure 3.1. shows a sample with imprinted text on the liquid side of the strip surface, which demonstrates this unique idea.[52]

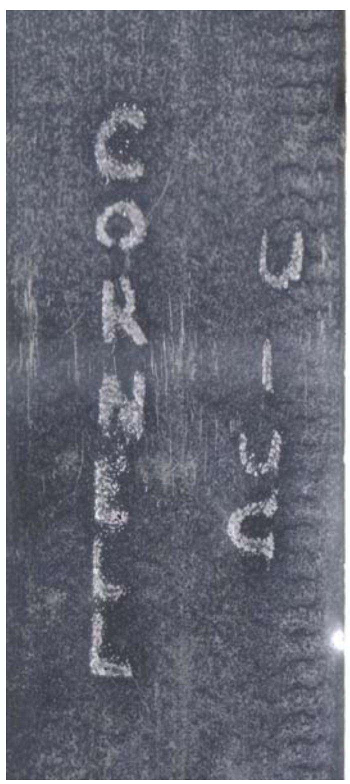

Figure 3.1. Controlled surface depressions on strip cast by planar flow melt spinning, using imprinting via BN wheel deposits

Different techniques can be used to produce strips with textured surfaces. These include laser interaction with the melt-pool, meniscus fluctuations from vibrations of the melt pool[2], and treating the wheel surface either thermally (such as via laser scanning) or physically, such as via coating deposits. For example, imprinting a layer of low-conductivity BN onto the wheel can act as an interface surface depression that transfers a 'negative' template from the substrate to the product during solidification[50, 51]. Surface depressions include longitudinal depressions along the casting direction and transverse depressions across the width of the strip, as shown in Figure 3.2. A depression on the substrate surface causes a local increase in thermal resistance at the interface between the strip and the wheel (wheel side surface) and thus slows the heat transfer and local solidification rate. This produces a corresponding deeper depression on the opposite upper surface of the strip (liquid side surface) which translates into discernable thickness variations. In order to quantify the effect of these interfacial depressions, a thorough understanding of the heat transfer phenomena occurring during this process is essential.

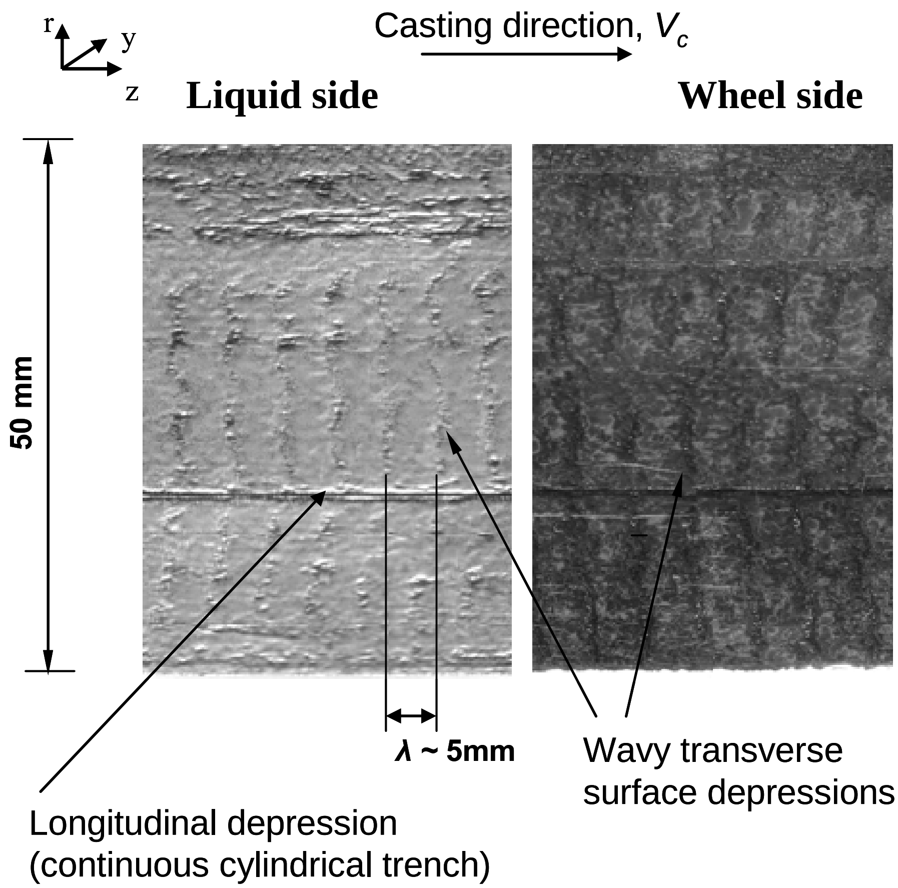

Figure 3.2 (a). Depressions observed in strip surface

As a first step towards quantitative understanding of heat transfer during melt spinning, a mathematical model of the process called STRIP1D has been developed in Chapter 2. STRIP1D is a transient one-dimensional heat-transfer model of the planar-flow melt-spinning process used to cast Al-7% Si strips on a Cu-Be wheel. In this chapter, the STRIP1D model is used to validate two- and three-dimensional heat transfer models of the process. The models are then applied to investigate the effect of casting conditions and interfacial depressions on heat transfer and solidification during melt spinning, including thickness variations and surface depressions. In particular, the longitudinal depressions caused by a continuous ridge of BN deposits and transverse depressions caused by rows of small, closely-spaced air pockets are investigated.

3.2. Literature Review: Process Conditions and Defect Formation

Some previous work has been done to estimate the effects of process conditions[20, 21] on heat transfer in strip casting processes, and to understand the surface defects occurring in different continuous casting processes[5, 47, 48]. Li and Thomas[21] have computed how increases in casting speed or superheat decrease the strip thickness. An increase in casting speed also increases the average interfacial heat transfer coefficient, thereby increasing the wheel temperature. Muojekwu et al[20] found that the interfacial heat transfer coefficient in aluminum strip casting increases as the wheel roughness decreases, owing to increasing contact between the strip and the wheel. In addition, increasing thermal diffusivity of the substrate material increased the interfacial heat transfer, owing to an increase in the ability of the chill to absorb and transport heat.

Efforts have been undertaken to understand how defects form in the related process of continuous casting of steel. Thomas[53] studied how fluid-flow causes defects to form during solidification. These include excessive surface turbulence causing fluctuations in the surface level, low casting speed or superheat which may result in partial freezing of the meniscus, inclusions and bubbles that may get entrapped in the solidifying shell thereby causing many costly defects in the final product. Sengupta et al[54] have found the formation mechanism of hook-type oscillation marks, which are long transverse depressions in the surface of the solidifying steel. They initiate by partial meniscus solidification, and the instantaneous shape of the meniscus at this time dictates the shape of the defect and its microstructure. The spacing of these marks is the product of the casting speed and the period of the mold oscillation cycle. Singh and Blazek[55] observed that solidifying shell is rippled for peritectic steels. The oscillation marks for these compositions are deeper. Jenkins and Thomas[56] have confirmed that deep surface depressions are responsible for the local variations in thickness of the steel shell. Thomas et al[57] have quantified the effect of an oscillation mark on decreasing interfacial heat transfer which delays the local solidification rate and results in a thinner steel shell. Level fluctuations are deviations of the meniscus position at the mold wall, which also lead to non-uniform solidification, deep oscillation marks, and surface cracks. Kubota[58] and Sasabe[59] found that large level fluctuations correlate with defects in the steel product.

There have been attempts to classify the defects occurring in melt-spinning. Depressions occurring at the liquid side surface of the strip form due to differential heat transfer from depressions at the wheel side, or due to unsteady fluid flow in the melt pool[47, 60]. Legresey et al[60] have attributed transverse thickness variations (longitudinal depressions) to heat-transfer variations at the strip-wheel interface and longitudinal thickness variations (transverse depressions) to fluctuations of the liquid metal level in the crucible. Carpenter and Steenl[47] classified the most common surface defects in the planar-flow spin-casting process as dimples, streaks, herringbone and cross-stream patterns[2]. The dimple pattern is the most common type of defect in pure aluminum. Each dimple is a depression on the liquid side surface of the strip that corresponds with a small depression at the same location on the wheel side surface of the strip. The streak pattern appears as long thin grooves that usually run along the casting direction (longitudinal) on the upper surface of the strip. Both the dimple and steak pattern depressions have been suggested to occur due to small gas pockets on the wheel side that form by air entrainment when the liquid metal first contacts the wheel[47]. Each pocket retards the heat transfer locally, so solidification is slower than elsewhere in the strip, which results in a depression on the liquid side of the strip. The herringbone pattern found on the wheel side of the strip, consists of wavy transverse lines on the wheel side and is caused by non-uniformities in fluid-flow. A small piece of metal protruding into the nozzle induces non-uniform flow and generates this pattern on the strip surface. Although the herringbone pattern consists of liquid side depressions similar to the other patterns, it suppresses other instabilities so the surface is smoother than with the streak or dimple patterns[47]. The cross-stream pattern is similar to the herringbone pattern and occurs only in alloys such as Al-7%Si. The pitch between the herringbone defects is ~1mm,[47] and between successive cross-stream waves (depressions) is ~ 8mm, which matches with the oscillation frequency of the liquid pool[2].

Research has been done to estimate the effect of various process parameters affecting the strip surface during the planar-flow casting process [5, 47, 48]. Haga et al measured the effect of nozzle type, ejection angle and nozzle-roll gap on the different types of surface defects observed on the surface during planar flow casting of aluminum foils. Since interference between the nozzle and the puddle has a significant effect on the liquid side surface, they recommend that the puddle size be restricted in order to avoid defects on the upper surface. Huang and Fiedler[48] extensively studied the effect of the wheel on surface defect formation. They identified distinctly different wetting patterns and defect types forming on smooth and matte-finished wheel surfaces. When casting on a smooth wheel, very small air pockets nucleate along the casting direction, depending on the stability of the melt pool. On a matte wheel, the air pockets nucleate randomly at low spots on the wheel and are responsible for heterogeneous patterns on the liquid side of the strip.

It is clear from previous work that fluid flow is responsible for transverse depressions and the herringbone and cross-stream patterns. It is not clear, however, if the waves caused by the time-dependent flow freeze to form surface depressions directly, or act indirectly by affecting the upstream meniscus. Despite many previous studies of surface defects in melt spinning there has been very little effort to quantify them.

Table 3.1. Process conditions for cases used in the parametric study.

Case	V_c (m/s)	G (mm)	Pressure head (kPa)	Measured PL (mm)	PL = f(G)) (mm)	q_{sup} (kW)	h_0 (225G) (kW/m^2)	Measured s mm
Case 20	9.54	0.580	4.9	9.24	11.75	261.5	130.41	0.147
Case 40	7.96	0.507	6.1	11.6	11.02	273.4	114.08	0.150
Case 47	7.2	0.73	4.0	12	14.23	337.2	164.25	0.169
Case 43 (standard)	**7.02**	**0.740**	4.6	**16.6**	14.45	410.0	**166.50**	0.206
Case 42	6.36	0.687	4.7	13.7	13.39	396.1	154.56	0.208

This chapter aims to quantify the effect of wheel-side surface depressions and other casting parameters on heat transfer and upper-surface depressions and thereby confirm the mechanism of their occurrence.

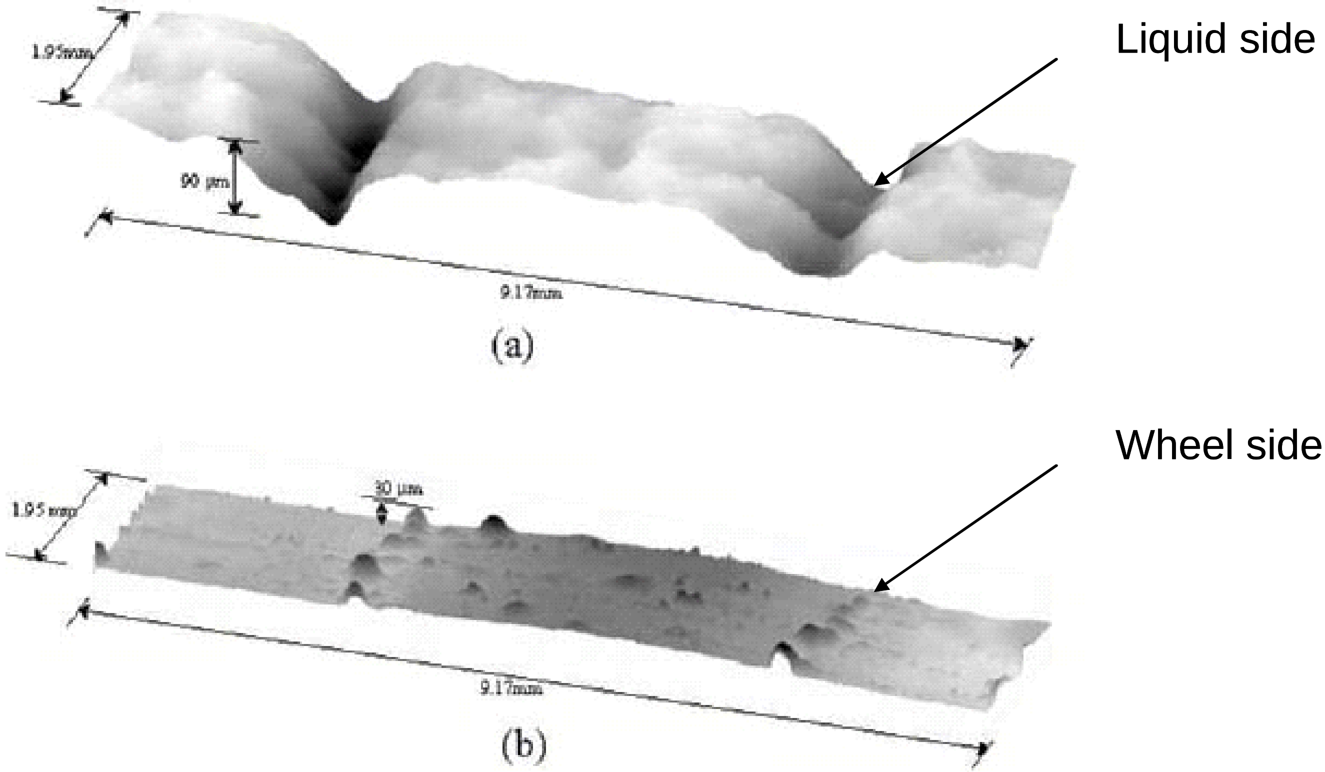

Figure 3.2(b). Close up of wavy transverse depressions (Steen et al[52])

3.3. Analysis of Strip-Casting Experiments:

The effect of process variables on the heat transfer and surface defects during the melt-spinning process was investigated with the help of five different casting experiments performed with the pilot caster at Cornell University[42]. A complete set of conditions and results were recorded as a function of time during each run, including casting speed, puddle length, gap height, strip thickness, and wheel temperature. Puddle length was measured using a high-resolution video recording shot during the cast. The solidified aluminum strip was cut into 15-cm long pieces and the average thickness of each sample was calculated by dividing its mass by the density, width, and length. The process conditions for each case are listed in Table 3.1. and were chosen at the end of cycle two. To investigate interfacial surface depressions, special attention was focused on Case 43, (Cast ID ODSU06_43)[61] which contained two different types of surface defect, pictured in Figure 3.2 (a). The first type was a long, continuous longitudinal depression, created by spraying a ridge of boron nitride onto the wheel surface prior to casting. The ridge was a straight line of about 0.03-mm high and 0.25-mm wide, consisting of many overlapping spot deposits.

The second type was a cross-stream pattern, which appeared as a series of transverse depressions (see Figure 3.2 (a)). The depressions are continuous cylindrical trenches that form roughly parallel wavy lines across the strip. Each depression corresponds exactly with a line of very closely spaced craters across the width of the strip on the wheel side. Figure 3.2(b). shows a close up of two rows of transverse depressions and reveals very small transverse air pockets, about 0.03 mm deep. Although these pockets appear hemispherical, others are about 3-5 times longer than their width, with a depth similar to their width. Note that the surface also includes random pockets that do not align to produce a transverse depression.

In order to measure these depressions, representative sections of the strip containing each type of depression were cut out and mounted in epoxy resin. The cylindrical samples were polished to 1200µm carbimet paper and 0.3µm alumina powder solution, and photographed. The micrographs were measured to obtain accurate local strip thickness and dimensions of the surface depressions.

3.4. Model Description

A thorough understanding of heat transfer in the melt-spinning process requires accurate computational models. Transient two- and three-dimensional heat-transfer models have been developed using ABAQUS[11]. They are validated with the transient one-dimensional heat-transfer model STRIP1D[62].

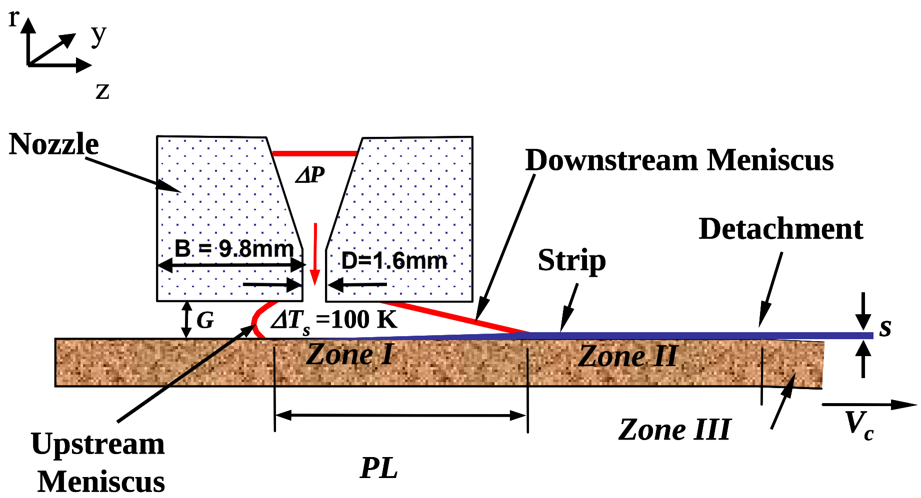

Figure 3.3. Schematic of Model Domain

Figure 3.3. shows a schematic of the model domain. The wheel is divided into three zones. Zone I is the "puddle region" where the liquid pool is in contact with strip. It is assumed that at the end of this zone, all of the liquid ($T>T_{liq}$ = 614°C) in the depression is retained by the melt pool and only the solidifying strip exits. In Zone II, the solidified strip cools in contact with the wheel until the strip becomes entirely solid ($T>T_{sol}$ =555°C). Zone III is after they separate. A separate two-dimensional steady model of fluid-flow and heat transfer has been developed of the liquid pool (zone I) with FLUENT[13] to obtain the superheat flux profile at the solidification front. The initial wheel temperature (T_{winit}) and the ambient temperature (T_{amb}) of 31.7°C was taken from experimental measurements. A constant density of 2400 kg/m^3, thermal conductivity of 135 W/m K and specific heat of 1190 J/kg K are used for Al-7% Si as mentioned in part one[62]. The average casting speed, puddle length, and other variables are taken from experimental measurements, given in Table 3.1.

A. *STRIP1D model:* A transient one-dimensional heat-transfer model of the planar-flow melt-spinning process called STRIP1D has been developed to simulate temperature and solidification in a one-dimensional slice of the strip and the wheel directly beneath it[62]. An internal boundary condition is used to incorporate the superheat flux entering from the liquid at the interface between the liquid and solidifying mush. The model features a time-dependent heat transfer coefficient model at the strip-wheel interface. Because decreasing gap height was observed to increase oscillation of the menisci[47] in the liquid puddle, the interface heat transfer coefficient also was proposed to decrease with gap height[62]. The complete model was calibrated to match the time-dependent strip thicknesses and wheel temperatures measured in the PFMS process at Cornell, and were validated by comparing with measured cooling rates, solidification velocities, strip surface temperatures, and secondary dendrite arm spacings. Complete details of this model are provided in Chapter 2.

B. *2-D model:* Multi-dimensional models are required to predict the effect of wheel side depressions and ridges on the strip surface. Figure 3.2(a). shows a typical longitudinal depression in the strip running along the casting direction. Since the depressions on both sides of the strip can be considered as long continuous cylindrical trenches, a 2-D transverse slice through the depression is sufficient to accurately predict the shape of the liquid side depression. Ignoring the wheel curvature effects, the 2-D transient heat conduction equation in Cartesian coordinates (r, y) governing this process is given by Eq. [1]

$$\rho c_p \frac{\partial T}{\partial t} = k\left[\frac{\partial^2 T}{\partial r^2} + \frac{\partial^2 T}{\partial y^2}\right] + Q \qquad [1]$$

Figure 3.4(a). shows the 2-D domain and boundary conditions used. The wheel-side depression is modeled as a part of the domain with properties of the material in the depression. The liquid side depression is inside the domain, which is assigned properties of Al -7% Si throughout. Its shape is defined by the liquidus contour at the exit of Zone I. The equations are solved using a 0.001 x 0.001mm mesh of 4-nodes linear elements in ABAQUS[11].

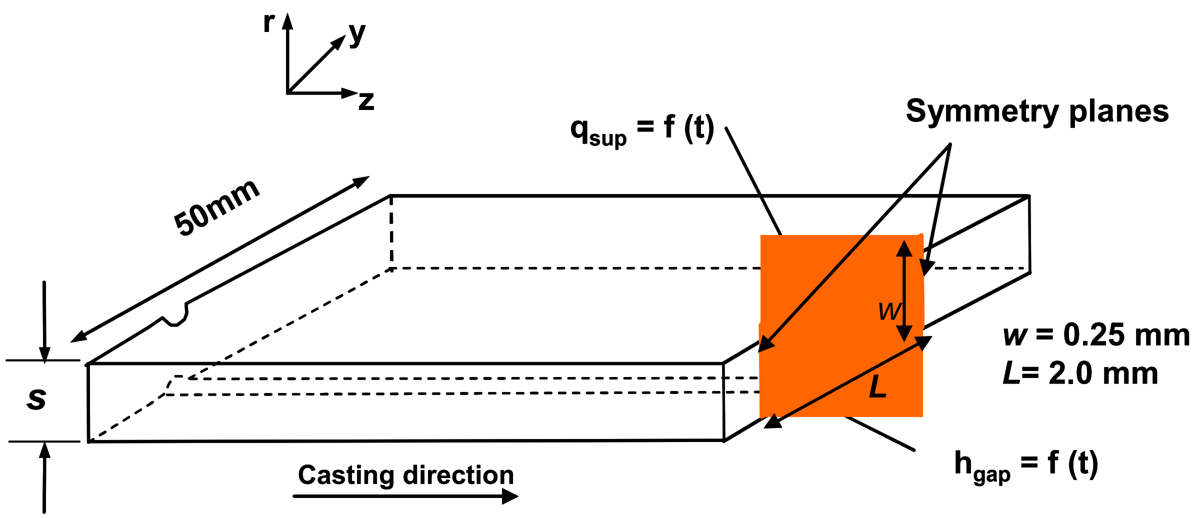

Figure 3.4(a). 2-D Model domain and boundary conditions for simulating longitudinal depressions

The bottom surface of the domain forms the strip-wheel interface and is exposed to convective heat transfer with the wheel, with a time-dependent heat transfer coefficient. The STRIP1D model was run using the same simulation conditions to obtain the wheel temperatures which are input to ABAQUS at the strip-wheel interface. The superheat flux obtained from the fluid-flow model described in Chapter 2. is input to the top surface of the domain. In the STRIP1D model this heat flux is added at the node just below the liquidus temperature (T_{liq}) which forms the interface between the liquid and solidifying mush. However, in the ABAQUS model these internal nodes cannot be accessed, so the superheat flux curve was added along the top surface of the domain. Because conduction through the liquid changes the superheat flux reaching the internal interface, the superheat flux input to the 2-D ABAQUS model had to be adjusted in order to match the solidification front growth profile obtained from STRIP1D. This was done by increasing the superheat by 150% before the impingement point, by 10% at the impingement point, then dropping it by 50% for a distance of 0.008m then finally increasing by 50% for the rest of the distance in Zone I. This resulted in a net increase of superheat by 74% over that obtained from the fluid-flow simulations, which went to provide sensible heat to the extra liquid elements in the 2-D model. Because of symmetry , both vertical sides of the domain were insulated. Like in the STRIP1D model, the whole domain is given an initial temperature of T_{liq} + T_{Δ} in order to avoid numerical errors owing to inaccurate interpolation.

C. *Extension to 3-D model:* Figure 3.2(b). shows a close up of typical transverse surface depressions which occur as hemispherical craters. The actual sample modeled here had elongated craters, with 0.046mm width, 0.023mm depth and 0.3 mm length that were spaced about every 0.1mm along the width and 5mm along the length of the strip. Unlike the long continuous trenches in the previous case, these depressions require solving the heat conduction eq. 1 in all three coordinate directions, in order to accurately simulate their effect on the heat transfer. Figure 3.4 (b) shows the model domain and boundary conditions. Exploiting periodic symmetry, a domain of 0.05 x 2.5mm is chosen to simulate one quarter of one crater and the corresponding strip, along with a domain height of 0.25 mm.

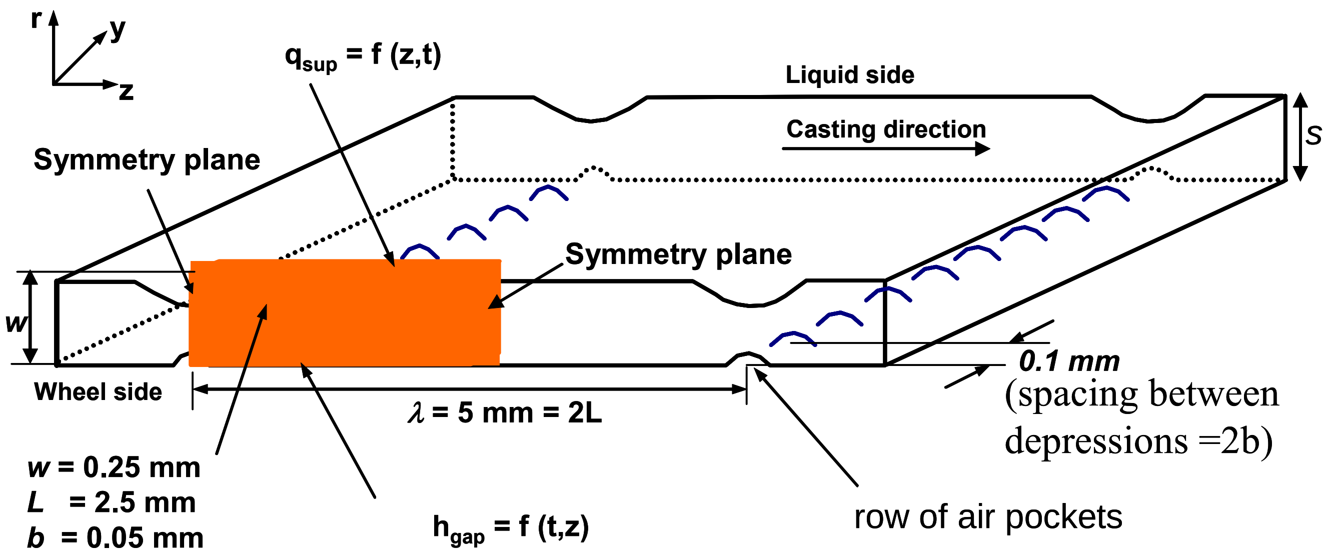

Figure 3.4(b). 3-D Model domain and boundary conditions for simulating transverse depressions

The boundary conditions are extended from the 2-D model case. An important difference is that the heat transfer coefficient h_{gap} and the superheat flux q_{sup} along the bottom and top surfaces respectively are transformed into functions of both time t and position z in order to convert the Eulerian reference frame to the Lagrangian frame of the model. This means that h_{gap} and q_{sup} vary along the casting direction as every point along the length of the domain has a different value of h_{gap} and q_{sup} as boundary conditions at a given time. The local time t_{local} at any given distance z along the domain from the right edge is given by Eq. [2].

$$t_{local} = t(\sec) - 10^{-3} z(mm) / V_c(m/s)$$

[2]

where V_c is the casting speed, and t is the time measured from when the right (front) edge of the domain is at the meniscus. The heat transfer coefficient at any point along the domain length is given by Eq. [3].

$$h_{gap}(z,t)(kW/m^2K) = 225G(mm)\left(\frac{10^{-4}}{t_{local}}\right)^{0.33}, t_{local} > 10^{-4} \quad [3]$$

where G is the gap height.

3.5. Model Validation

The STRIP1D model was validated extensively in Chapter 2. The multi-dimensional models are validated by comparing their predictions with STRIP1D model results. First, the "validation case" explained in part one[62] is extended to 2-D. The right edge of the 2-D domain in Figure 3.4(a). in section IV B opposite from the wheel-side depression is equivalent to the one-dimensional domain in STRIP1D. The model simulates the strip in zones I and II. In zone I, the heat flux (see Figure 2.6. in Chapter 2.)curve obtained from the results of a fluid-flow heat-transfer model of the melt-pool in FLUENT, is imposed on the top surface to account for the superheat flux entering the solidifying shell. The wheel side is exposed to convective cooling at the strip-wheel interface as in STRIP1D. The vertical sides of the domain were insulated owing to symmetry. As with STRIP1D, the initial temperature is 617°C, which includes $T_\Delta = 3\ ^{o}C$ to avoid numerical errors. The domain height is dropped to 0.25mm to minimize errors from conduction in the liquid. The simulation conditions are given in Table 3.3.

Table 3.3. Process conditions for different cases used for the ABAQUS 2-D model.

Name	Validation Case	Case 43 (standard)	BN Case	Air pocket Case
G = Gap height: (mm)	1.5	0.74	0.78	0.63
PL = Puddle length (mm)	23. 3	16.6	16.6	20.1
Zone II length (mm)	0	77.9	79.5	63.7
V_c = Wheel speed (linear) (m/s)	6.23	7.02	7.02	8.85
ΔT_s = Superheat: (K)	100	100	100	100
t_1 = Zone I contact time (ms):	3.74	2.36	2.36	2.27
h_0 = Interfacial heat transfer coefficient (kW/m^{2}K)	170	166.5	175.5	141.7
s = Strip thickness (mm)	0.233	0.206	0.215	0.183
Angles θ_1, θ_2 (^{o})	(4.39,0)	(3.13,14.7)	(3.13,15)	(3.13,12)

Figure 2.10(b). in Chapter 2 shows a reasonable agreement in the solidification front growth profiles between the STRIP1D and ABAQUS models for these conditions. The ABAQUS model profile is slightly higher than the STRIP1D model in the initial 1.7 ms, perhaps due to adding the superheat to the top surface and not at the interface. Temperature evolution through the strip thickness was also compared and a perfect match is observed in Figure 2.11. in Chapter 2. Only temperatures in the solidifying strip are comparable, as temperature evolution in the liquid is not modeled accurately with the superheat flux method. The 2-D model is further validated by comparing solidification front and temperature predictions in zone II, as explained in section VI E1. The 3-D model is validated in a similar manner by comparison with STRIP1D predictions far from the depressions. This is discussed in section VI E2.

3.6. Results

The casting conditions during the melt-spinning process play a very important role in determining the quality of the product. Parametric studies have been performed to understand the effect of several process conditions on heat transfer, including casting speed, gap height, puddle length, superheat and interfacial depressions. The exact conditions of each study are explained in Table 3.2. To further validate the model, the first two zones of the five experimental cases were simulated according to the conditions in Table 3.1., with all other model parameters constant. Good agreement between the measured and predicted strip thickness is observed in each case.

A. *Effect of casting speed (V_c):* Casting speed is one of the most important factors that determines the thickness of the product. A thicker strip requires an increase in "residence time", or contact time in zone I, when the strip is beneath the puddle and in good contact with the wheel. Lowering casting speed increases this residence time and hence solidifies thicker strips. To isolate the effect of casting speed with constant puddle length, the process conditions for Case 43 (Table 3.1.) were simulated for different casting speeds. Figure 3.5. quantifies the decrease in the strip thickness with increase in casting speed. Casting speeds ranging from 5-10 m/s were predicted to produce 0.25-0.16 mm thick strips. However, in reality, where flow rate is controlled (by maintaining the pressure head in the crucible), increasing speed decreases residence time, which increases the average heat transfer rate, (see Eq. 3) and results in decreased puddle length. Specifically, doubling the casting speed halves the strip thickness for a constant flow rate. This makes the effect of casting speed on decreasing strip thickness more severe.

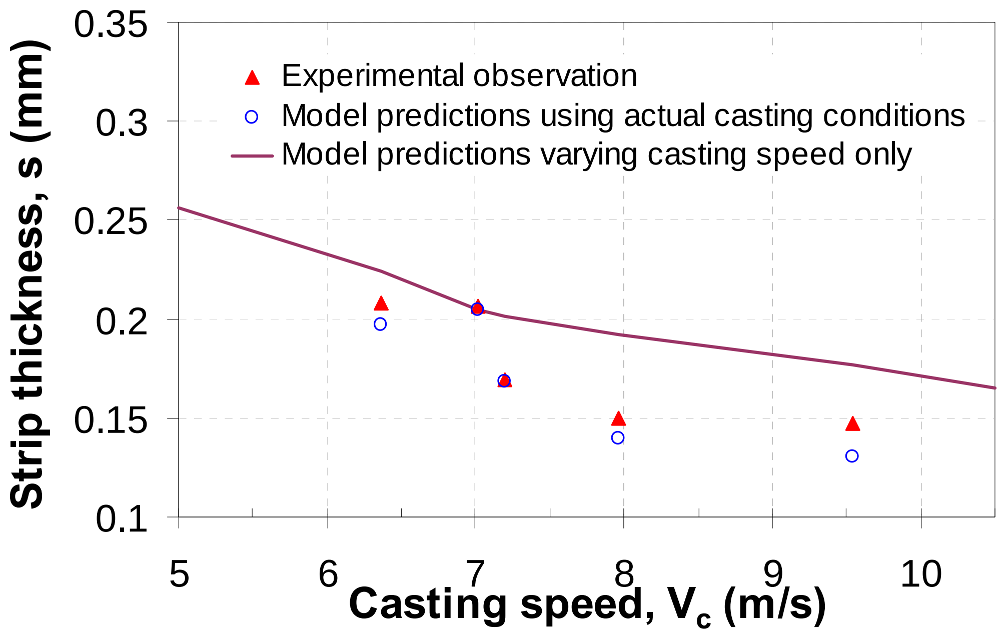

Figure 3.5. Effect of Casting speed on Strip thickness

Table 3.2. Predicted strip thickness (s, mm) for different conditions

Conditions varied	***V_c G, PL***	***V_c* only**	***h_0 = f(G) only***	***PL= f(G) only***	***PL & h_0 = f(G)***	***PL* only**
Conditions kept standard	**None (all meas.)**	***PL, G, h_0***	***V_c, PL***	***V_c, h_0***	***V_c***	***Vc, G, h_0***
X-axis	*V_c, PL, G*	*V_c*	*G*	*PL, G*	*PL, G*	*PL*
Case 20	0.130	0.177	0.173	0.171	0.151	0.151
Case 40	0.140	0.195	0.159	0.174	0.138	0.17
Case 47	0.168	0.201	0.201	0.191	0.19	0.173
Case 43 (standard)	0.205	0.205	0.205	0.194	0.196	0.205
Case 42	0.197	0.224	0.196	0.182	0.184	0.185

Figure 3.6. shows the effect of casting speed on the wheel temperatures, computed near the end of zone I at 1.6 ms to mimic a "sliding thermocouple". The inner and outer wheel temperatures increase with casting speed. An increase in casting speed decreases the residence time. Less time in zones I and II increases the average heat transfer coefficient across the strip-wheel interface.[62] Also the wheel undergoes less cooling due to the decreased time spent in zone III. These two factors together result in an increase in the wheel temperatures in both the inner and outer surfaces of the wheel, as observed by Li and Thomas[21]. The effect of this wheel heat-up is negligible, however, as the strip thickness drops only 10% from the first to tenth cycles from this effect alone.

B. *Effect of gap height (G):* Experimental observations indicate that strip thickness is directly related to gap height. As gap height also affects several other variables, its effect on strip thickness was investigated under four different sets of conditions.

1. *Experimental conditions:* The best model predictions of strip thickness for the actual experimental conditions, which already validate the model, are replotted as a function of gap height in Figure 3.7. The trend is very rough, owing mainly to changes in casting speed.

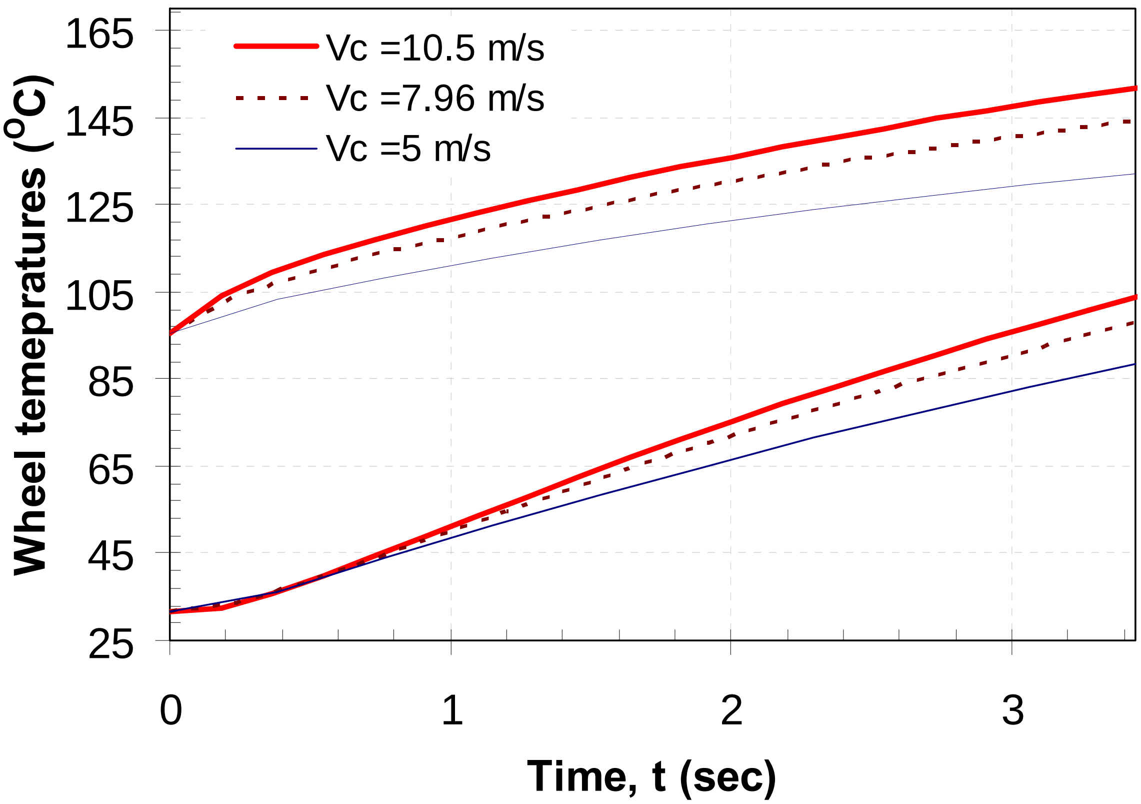

Figure 3.6. Effect of casting speed on wheel surface temperatures

2. Varying PL=f(G) only: Transient measurements from all five cases were plotted in Figure 3.8. to reveal a trend in the puddle length variation with gap height. A curve fit to describe this variation is given by:

$$PL = 28.915G^2 - 21.314G + 14.385 \qquad [4]$$

Employing this relation to choose the puddle length, the effect of gap height on strip thickness was re-plotted, keeping all other conditions the same as standard Case 43. As expected, the strip thickness decreases with gap height, due to less residence time in zone I from the shorter puddle length. Figure 3.7. shows a sharp decrease in strip thickness for a gap height dropping until 0.61 mm, with more gradual drop for further gap reduction. This reflects the parabolic trend in Figure 3.8., where the slope drops with decreasing gap height.

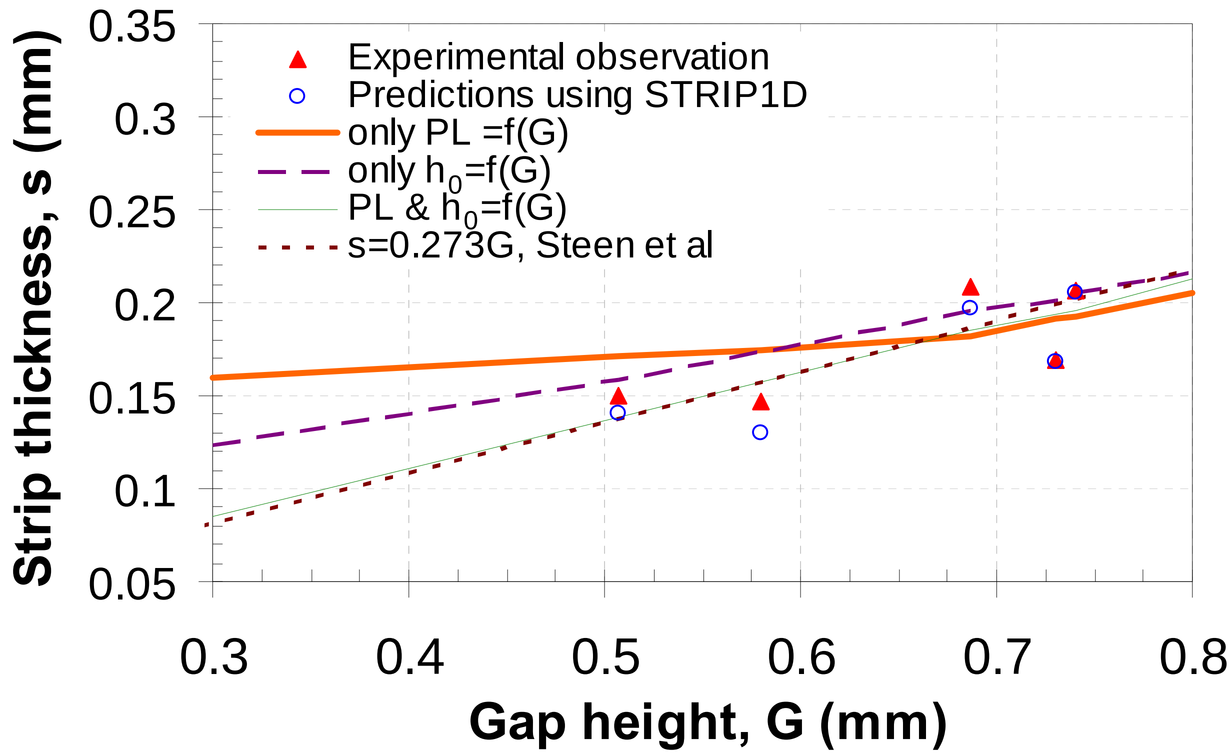

Figure 3.7. Effect of Gap height on Strip thickness

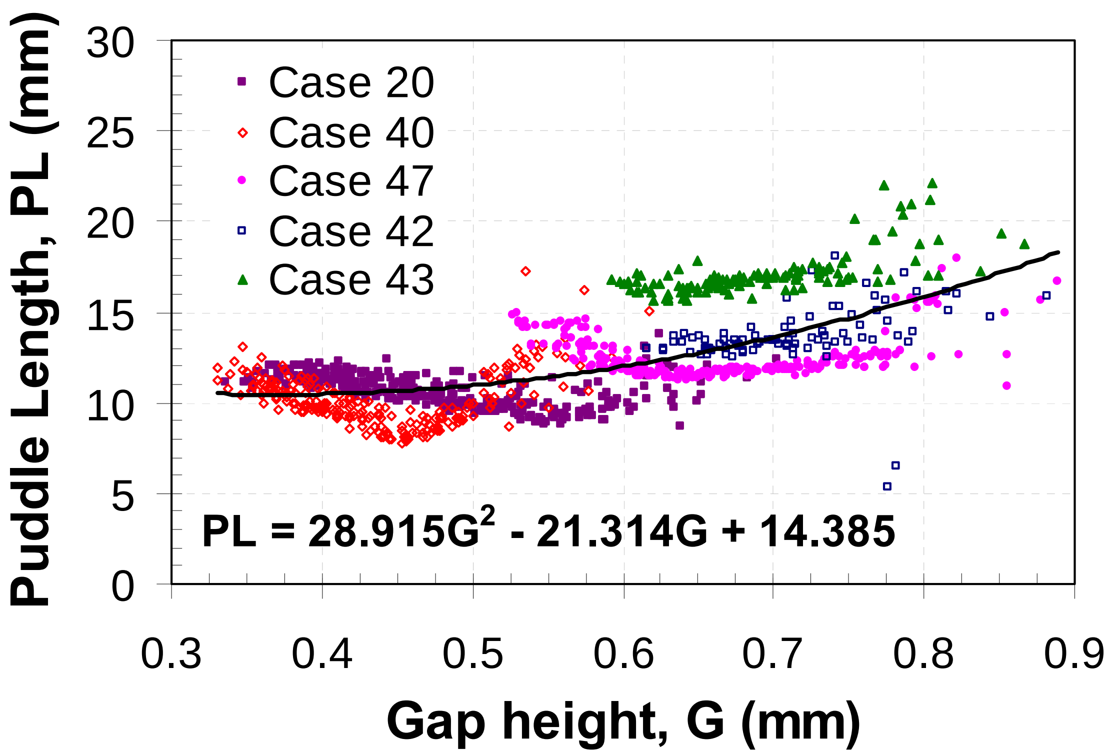

Figure 3.8. Puddle length as a function of Gap height

3. Varying h_0=f(G) only: To isolate the effect of gap height due to dropping the interfacial heat transfer coefficient, all conditions including puddle length were kept the same as that of Case 43, except for the following relation introduced in Chapter 2.

$$h_0 = 225G \tag{5}$$

Figure 3.7. shows that strip thickness naturally drops with decreasing gap for this condition, due to the accompanying drop in heat transfer rate. For a gap height of 0.74, this condition is equivalent to simulating Case 43, so the line intersects the prediction for this experimental case. The drop in thickness is more severe than the previous condition, showing that the heat transfer effect of gap is more important than its effect on puddle length.

4. Varying PL=f(G) and h_0=f(G): This most realistic case includes both effects of gap height from the previous two conditions to study the combined effects of the interfacial heat transfer coefficient and puddle length on strip thickness. As shown in Figure 3.7., these two consequences of decreasing gap greatly decrease the strip thickness. Furthermore, the drop in the strip thickness for this condition is more severe than either of the individual effects alone (sections VI B1 and VI B2) because the effects are additive.

The real effect of gap height on strip thickness can also be determined using mass balance[37, 47, 63], and used for further model validation. Rearranging the mass balance and Bernouli-relation between head and flow rate, Eq [5] from Carpenter and Steen[47], gives

$$s = a\left[\frac{2\Delta P}{\rho V_c^{\,2}}\right]^{0.5} G \tag{6}$$

Further setting the constant a=1[61], and substituting the values for pressure head, ΔP, V_c, and density, ρ, from Case 43 gives

$$s = 0.273G \tag{7}$$

These equations show that an increase in gap height allows the liquid flow rate to increase, which increases the strip thickness (other conditions constant). Plotting this relation as a function of gap height in Fig. 7 intersects with the experimental point for case 43, demonstrating the accuracy of this simple relation in predicting strip thickness. This relation also produces an almost exact match with the strip thickness line obtained with condition 4. These results validate the predictive ability of present model. The heat transfer model can predict strip thickness accurately only by including the effects of gap on both heat transfer coefficient and puddle length.

C. *Effect of puddle length (PL):* Puddle length refers to the length of the melt pool which characterizes the time spent by the strip in Zone I. The effect of puddle length on strip thickness is investigated for two different conditions.

1. Varying PL only: The effect of varying puddle length on strip thickness is plotted in Figure 3.9., with all other conditions kept standard (Case 43). As expected, a nearly-linear decrease in strip thickness with decreasing puddle length is observed, owing to the decrease in residence time in the liquid pool. This result also shows an accidental match with the rough trend in the experimental cases.

2. Varying PL=f(G) and h_0=f(G): This more realistic condition is replotted in Figure 3.9. from Figure 3.7. to present the typical expected effect of puddle length on strip thickness. As observed in each of the five individual data sets in Figure 3.8., the puddle length in each cast initially decreases with time and decreasing gap height but later increases with further decrease in gap height towards the end of the cast. Initially, the decrease in gap height decreases the flow rate. This decreases the strip thickness and thereby shortens the puddle length, starting from the top right of the solid line in Figure 3.9. However, towards the end of cast, the smaller gap height lowers the heat transfer coefficient greatly, while only slightly decreasing the strip thickness. The net effect is that the puddle length must increase to allow time for this strip thickness to solidify. This effect is captured by the end of solid line in Figure 3.9., where the puddle length increases for gap heights less than 0.37mm. The shortest puddle length is 10.45 mm. This indicates that the puddle length is dictated by the heat transfer and the strip thickness, both of which are determined by the gap height.

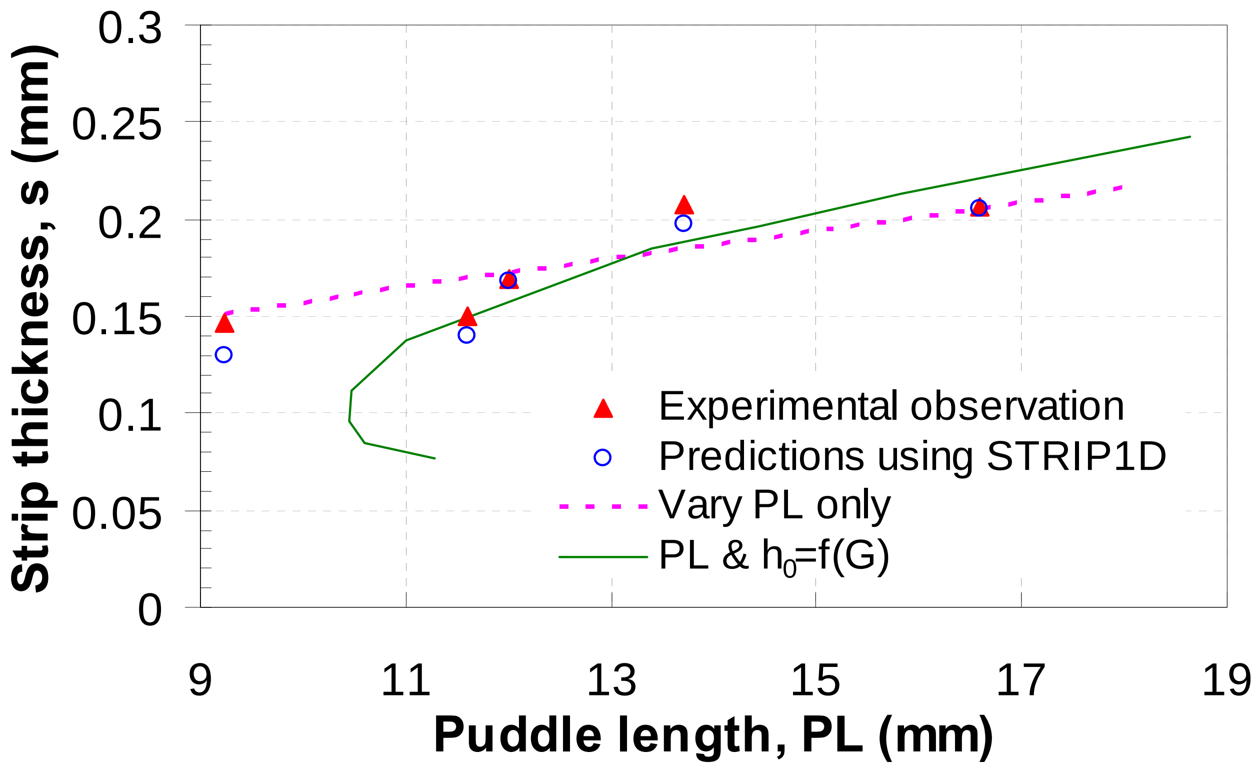

Figure 3.9. Effect of Puddle length on Strip thickness

D. ***Effect of super heat (ΔT):*** An increase in the superheat temperature tends to slow the solidification of the strip in the melt pool. This is captured in the model by increasing the superheat flux delivered at the liquid-solidifying mush interface according to

$$q_{\sup} = \dot{m}\, c_p \Delta T \tag{8}$$

This increased superheat decreases the strip thickness, as shown in Figure 3.10., with other conditions (including puddle length) remaining constant. As superheat decreases towards zero, the strip thickness could eventually reach the gap height, causing a catastrophic freeze-up of the process. The effect can be prevented by increasing casting speed. In reality, decreasing superheat will shorten the puddle length, for a given flow rate and casting speed.

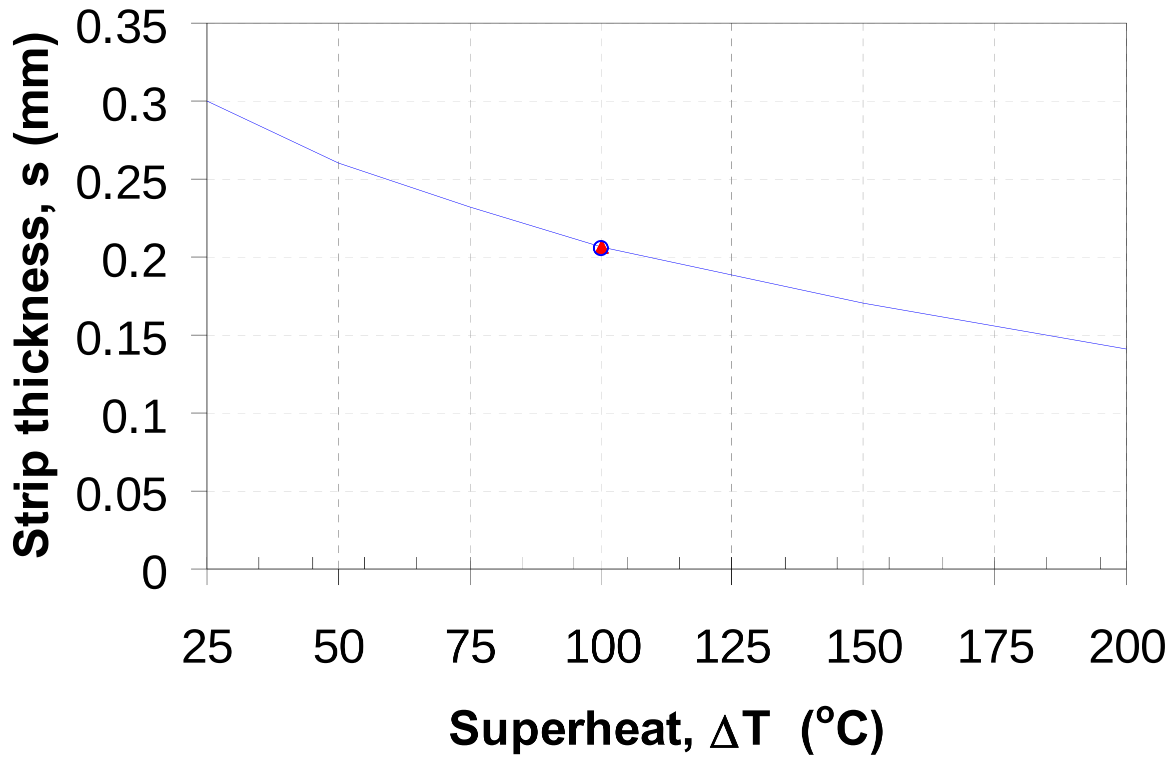

Figure 3.10. Effect of superheat on strip thickness

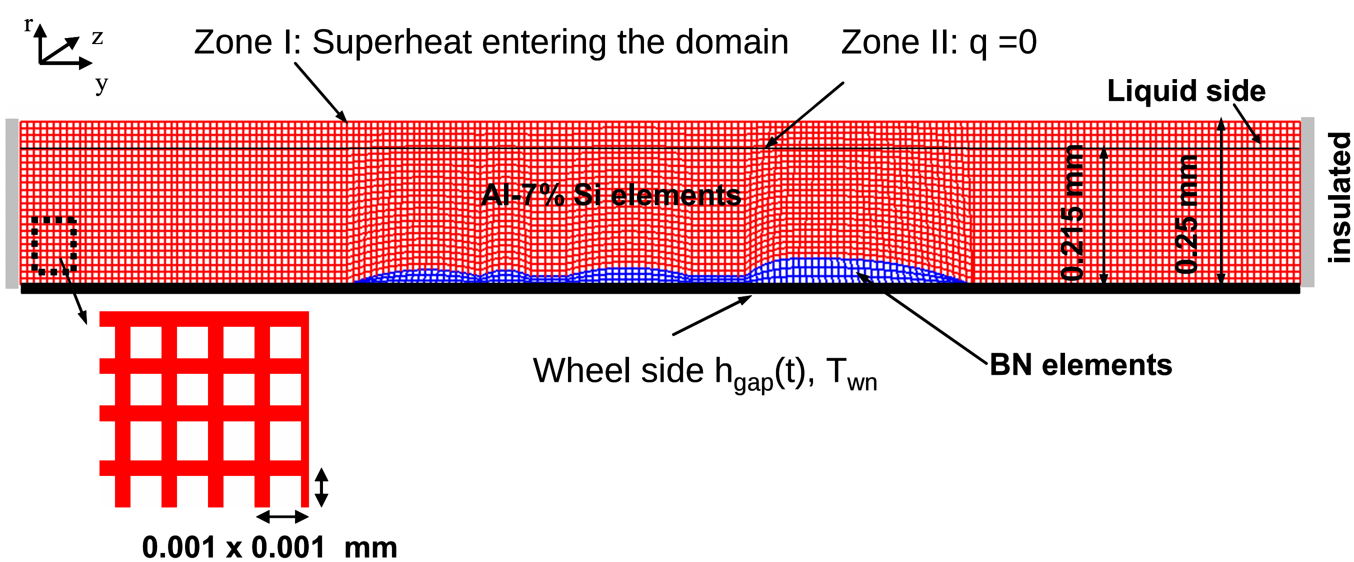

Figure 3.11. 2-D Domain, Boundary conditions & Mesh (BN case)

E. *Effect of surface depressions:* Surface depressions form where the meniscus first contacts the strip-wheel interface from several causes, discussed in Sections I and II. This section models the effects of two different types of wheel-side depressions on local heat transfer and thereby predicts the shape of the corresponding liquid-side surface depressions. Specifically, the model is applied to simulate longitudinal depressions caused by a linear ridge of interfacial boron nitride and transverse depressions due to rows of air pockets entrained at the meniscus / wheel interface.

1. *Continuous BN-gap case*: In order to quantify the effect of an interfacial BN ridge, several regions of the wheel were sprayed with a line of boron nitride (BN) deposits in the longitudinal direction (casting direction). After casting, longitudinal surface depressions formed on the liquid side of the opposite from the BN deposits. The 2-D model described in section IV B was applied to simulate and quantify this effect.

The depression shapes on both sides of the wheel were measured, as described in section III . The BN wheel-side ridge appeared as a line of dense dots along the casting direction. This was approximated as a continuous cylindrical trench along the strip. Figure 3.11. shows the domain, boundary conditions and mesh used to model the strip for this case. The elements comprising the wheel-side depression were assigned properties of BN. The contact resistance between the BN sprayed on the wheel and the strip has been neglected. The measured gap height for this sample was used to obtain the heat transfer coefficient from Eq. [5] at the strip wheel interface. The outer wheel temperatures obtained from the STRIP1D model, shown in Figure 3.12., were used to complete this boundary condition. The superheat flux profile added at the top surface of the domain was adjusted until the solidification fronts obtained from the ABAQUS matched STRIP1D results, as shown in Figure 3.13. The model was then run in ABAQUS until the strip exited Zone I, using the measured puddle length to define the residence time (see Table 3.3.).

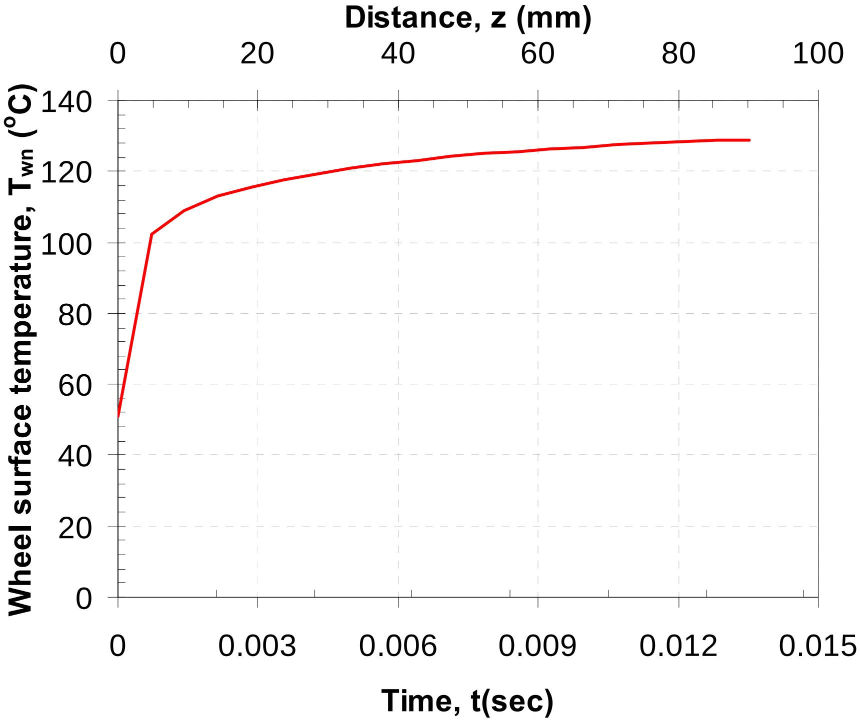

Figure 3.12. Wheel surface temperature profile (BN case)

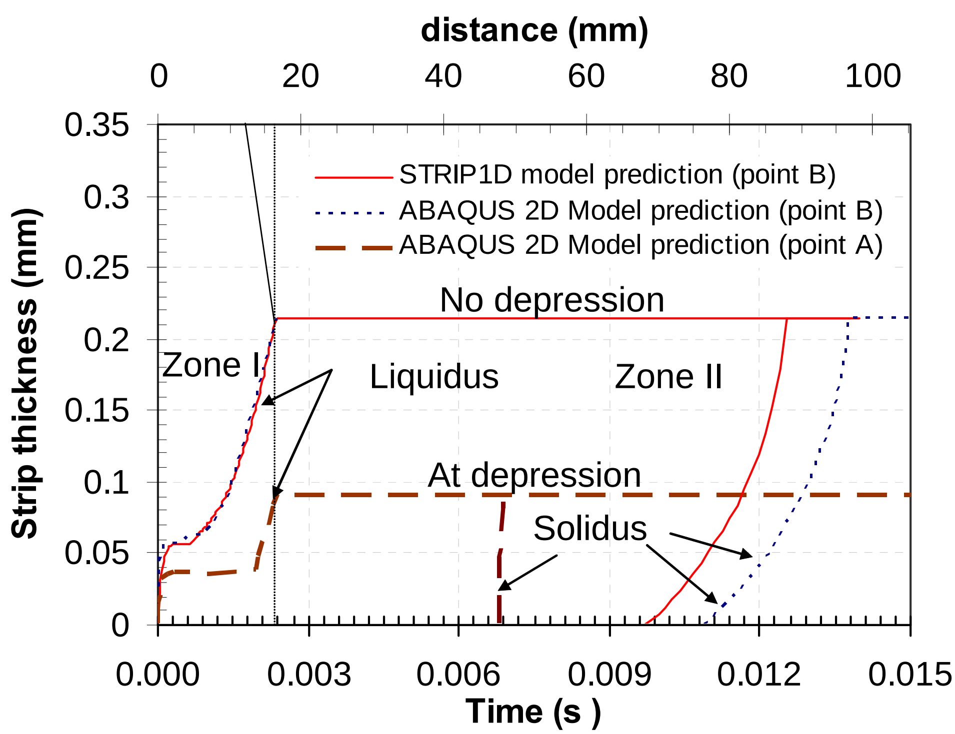

Figure 3.13. Solidification front growth profile (BN case)

The low conductivity of BN relative to Al-7%Si increases the thermal resistance across the BN-filled gap. This lowers the local solidification rate above the depression relative to the rest of the strip. This causes a corresponding depression on the liquid side of the strip. Figure 3.14. shows the temperature distribution through the thickness of the strip at the end of Zone I at two different locations: A (maximum depression depth) and B (right edge of the domain where heat transfer is 1-D). The temperature distribution through the strip thickness at point A indicates a very high temperature gradient within the BN depression, owing to its insulating ability. This produces higher temperatures in the strip just above. Temperature gradients through most of the strip (eg. point B) are very shallow, with maximum temperature differences of only ~25^{o}C.

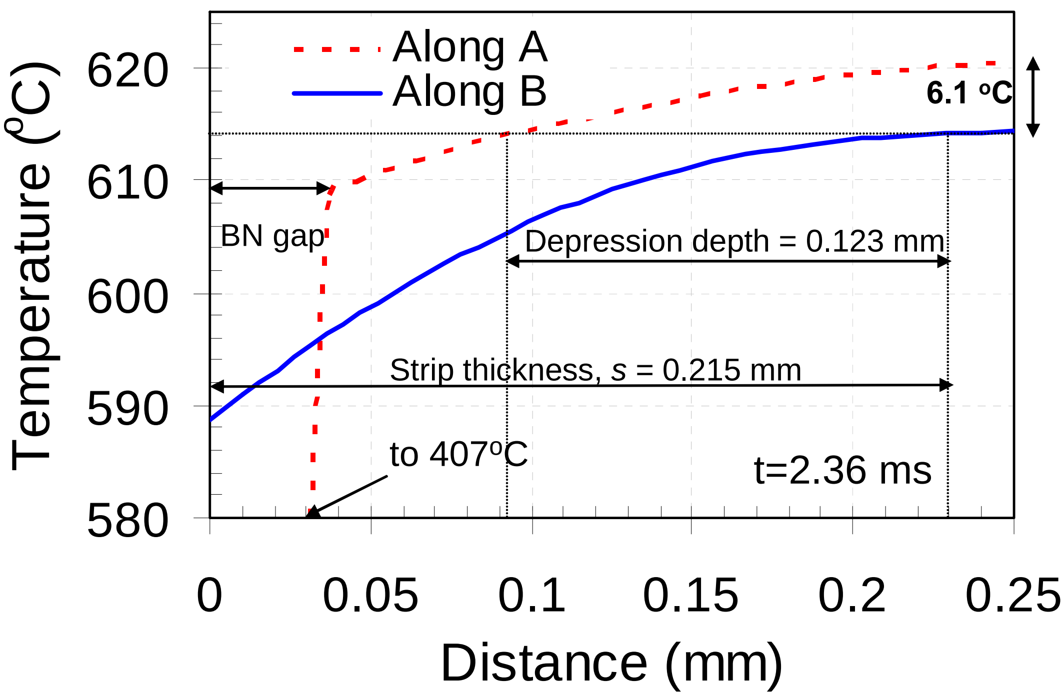

Figure 3.14. Strip temperature profiles at Zone I exit showing liquid-side depression depth (BN case)

Figure 3.14. also indicates the depth of the liquid-side depression. Intersecting the horizontal liquidus line (614^{o}C) with the temperature profiles indicates the strip thickness at points A and B. The difference is the depression depth of 123μm in this case. This is more than half of the 215μm total thickness at this location, indicating the substantial influence of the small BN ridge, which has a maximum thickness of less than 30μm. The complete depression shape (defined by

$T > T_{liq}$) is revealed in the contour plot in Figure 3.15., which also shows a comparison with a micrograph of the sample. An excellent match is observed. The similar shape and difference in depth of only 2 μm strongly suggests that the model is reasonable. It should be noted, however, that the neglect of contact resistance between the BN and the strip may have cancelled the approximation of the BN deposits as a cylindrical trench, resulting in a near-perfect match.

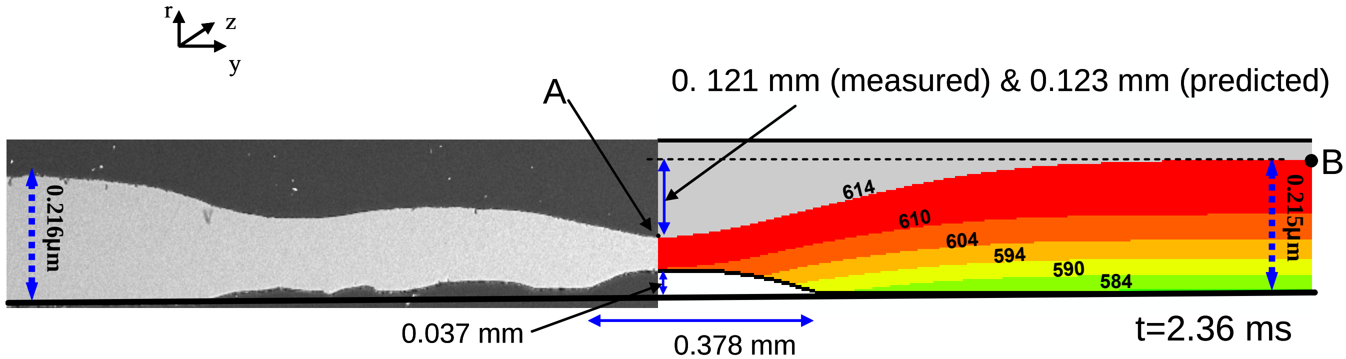

Figure 3.15. Comparison between measured and predicted longitudinal depression profile at Zone I exit, (BN case)

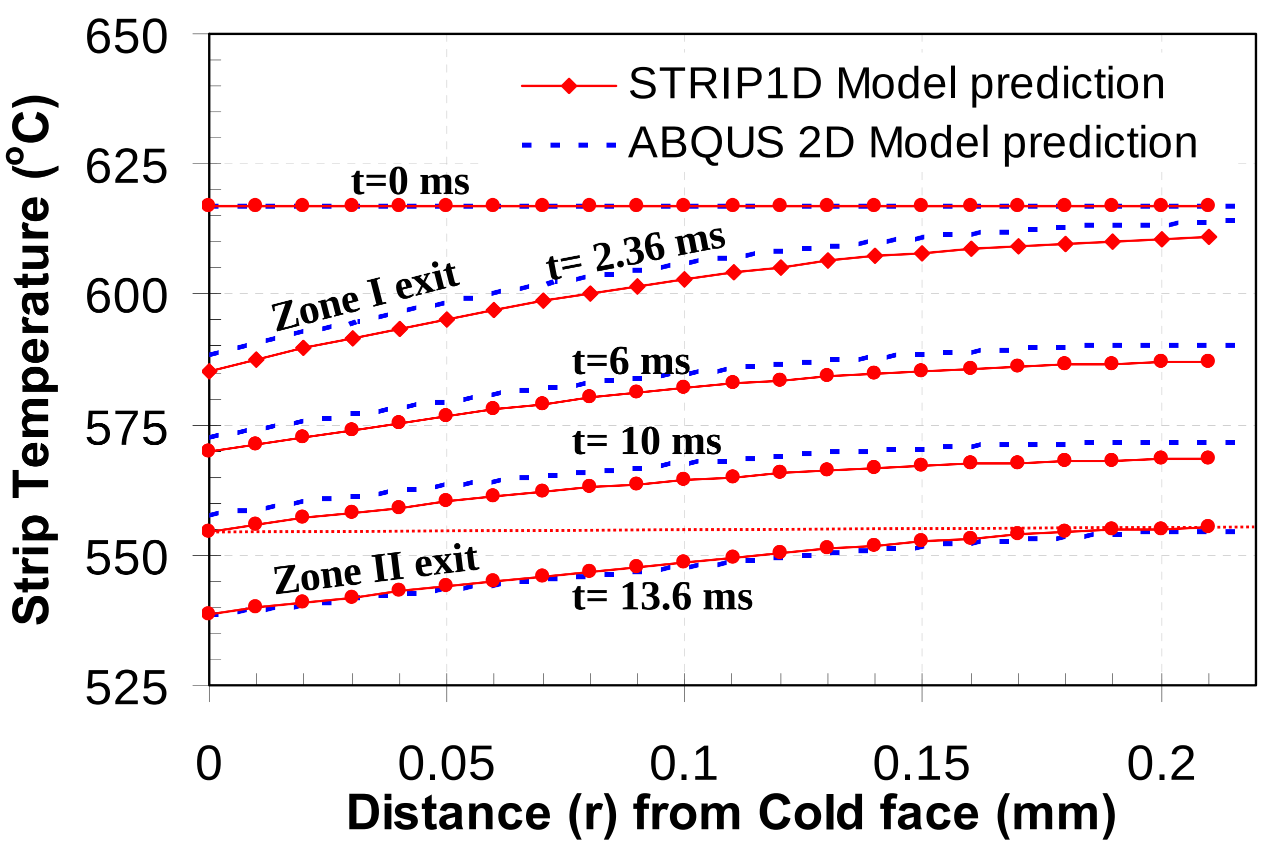

Figure 3.16. Predicted temperature profiles through strip thickness with time (BN case)

Since only solid or mushy strip exits zone I, all of the liquid nodes ($T > T_{liq}$) were removed from the 2-D model. The simulation was then further run until the strip became fully solid, indicating the end of zone II. Figure 3.13. compares the solidification front growth of the liquidus and solidus for both the ABAQUS 2-D and STRIP1D models in zones I and II. The 2-D model predicts slightly higher temperatures and slower solidification because ABAQUS is unable to apply the superheat flux at the internal solidification front. The error is only about 3^{o}C, however, which validates both models.

It is interesting to note that solidification at the depression location (2-D model) is delayed while the strip is in zone I but is faster than the rest of the strip in zone II. In zone I, the low-conductivity gap naturally slows the local solidification. However once the strip enters zone II, there is no more liquid above the depression so the thin strip at the depression location can cool faster by conducting heat laterally .

2. *Discontinuous air-gap case:* The formation of the transverse surface depressions of the cross-stream pattern in Figure 3.2(a). was simulated with the 3-D model, assuming they are caused by the periodic rows of air pockets[47, 48] across the strip-wheel interface. Each row of air pockets is attributed to the continuous oscillation of the liquid pool which entraps air at the meniscus where the liquid metal and air contact together. These closely-spaced depressions represent a third time-scale of thickness variations along the strip. The model methodology was similar to that for the BN-gap case. The boundary conditions were obtained by first running the STRIP1D model. Periodic symmetry was invoked in both directions, so the 3-D model domain needed to contain just one quarter of a single air pocket, as discussed in Section IV C, and shown in Figure 3.17. bottom. The air pockets are spaced every 0.1mm across the strip and are elongated in the casting direction with 5mm spacing (Figure 17 top). Table 3.3. gives the process conditions for this case.

Figure 3.18. shows the solidification front growth of the strip with and without the depression. The strip- growth solidification front at a location far from the depression where the heat transfer

is one-dimensional matches with that obtained from STRIP1D, which validates the 3-D model. The liquid-side depression starts solidifying later, due to air pockets at the wheel-side. The air pockets themselves are seen to remain above the liquidus temperature for most of Zone I.

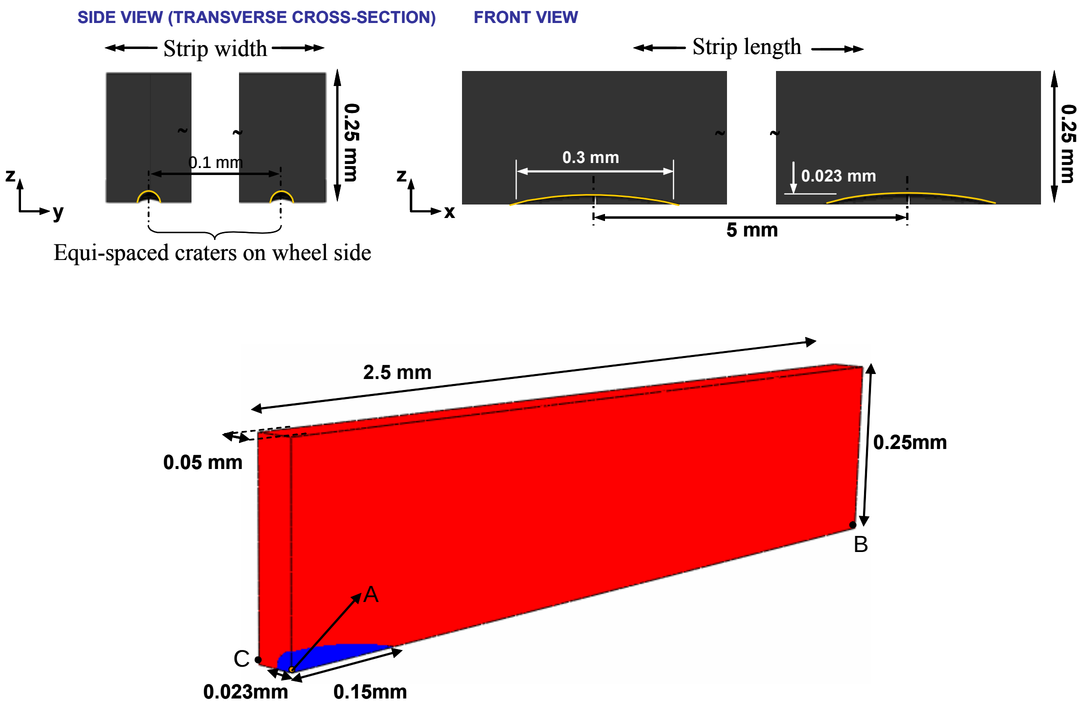

Figure 3.17. 3-D domain showing transverse depression geometry (Air gap case)

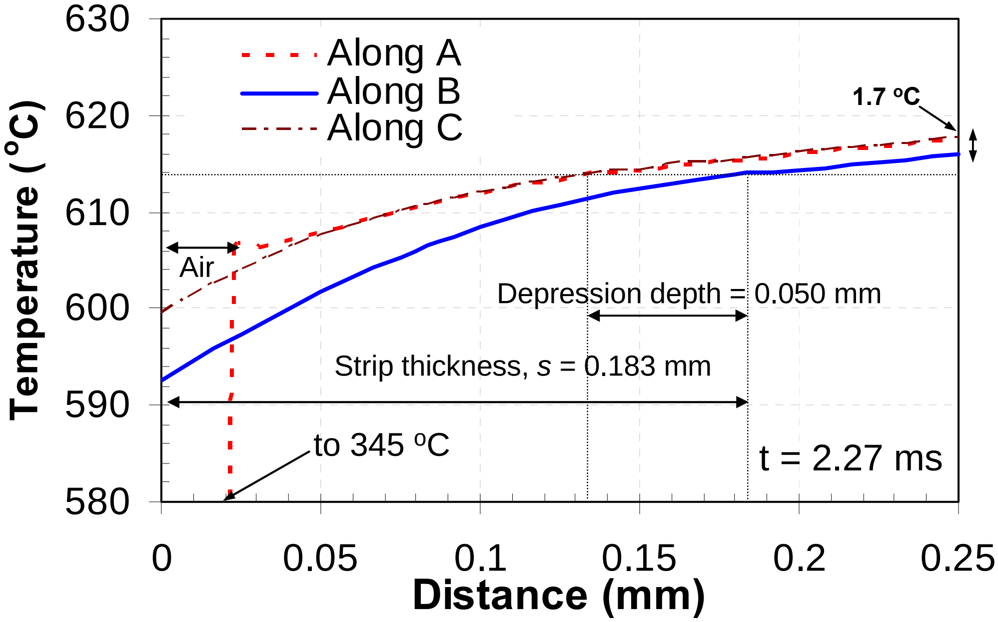

Figure 3.18. Temperature profiles at Zone I exit showing liquid-side depression depth (Air gap case)

Temperature profiles computed through the strip thickness at various locations A, B and C are presented in Figure 3.19. As expected, the temperature profile through the strip at the depression (point A) is higher than that through the 1-D region (point B) and is due to the large temperature gradient through the insulating air pocket. The temperature profile along C, which represents the end of the domain along the width matches the profile at A at about 0.05 mm above the wheel surface, which indicates the continuous nature of the obtained liquid side depression. The individual depressions caused by each gas pocket merge together because they are spaced so closely across the width. Although similar in appearance, the longitudinal surface gradient of 1.7°C is less than the 6.1°C gradient found in the BN gap case, because of the shallower, discontinuous nature of the air pockets.

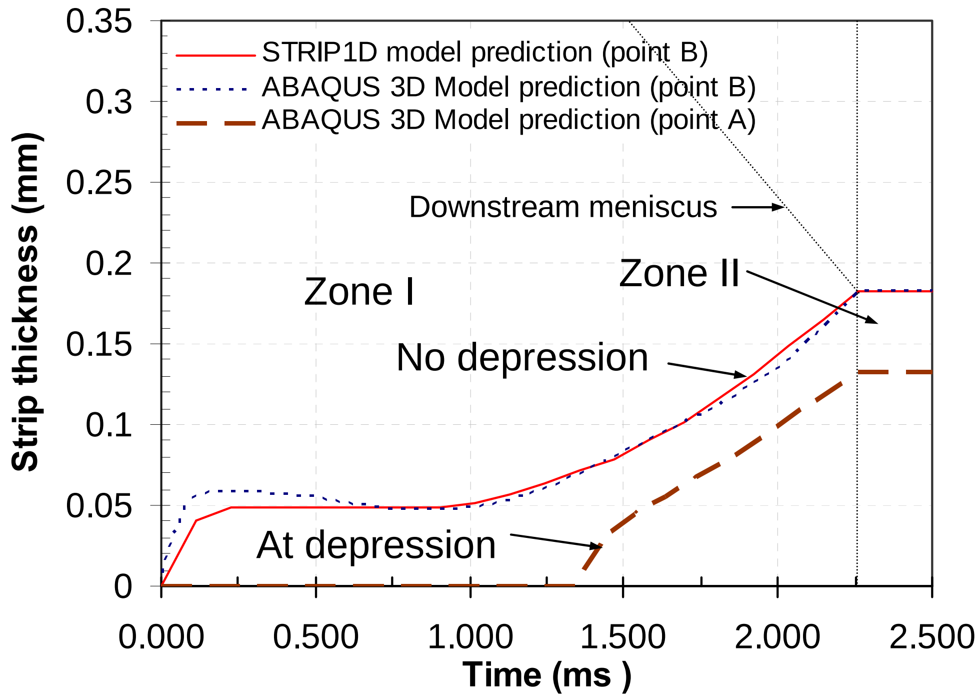

Figure 3.19. Solidification front (liquidus) growth profile at Zone I exit (Air gap case)

Figure 3.20 shows a 3-D view of the temperature contours in the domain to illustrate the predicted shape of the liquid side depression. The computed liquid-side depression depth is 50mm everywhere across the width. The predicted and measured depression shapes are compared in Figure 3.21. and the match is close. The small variations and uncertainness in the spacing of the small air pockets are responsible for the slight discrepancies. For the gas pocket size, shape and spacing studied here, the individual wheel-side depressions result in a continuous depression on the liquid side of the strip.

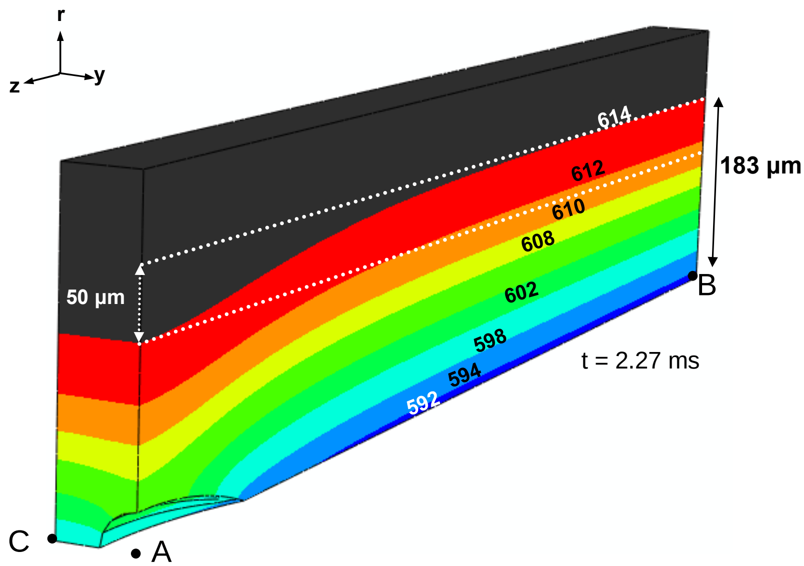

Figure 3.20. Temperature Contours through the strip at Zone I exit showing transverse depression
(Air gap case)

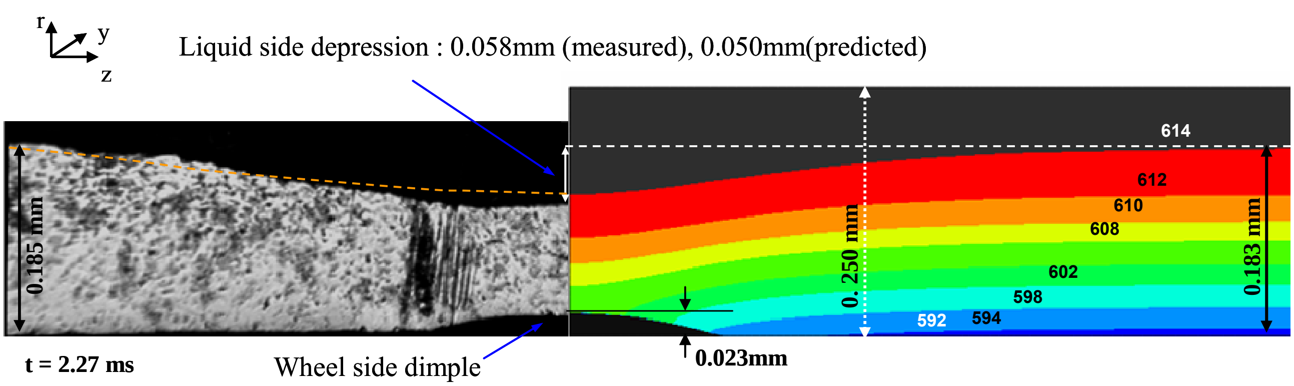

Figure 3.21. Comparison between measured & predicted transverse depression shapes at Zone I exit (Air gap case)

If these wheel-side craters were deeper or spaced further apart, they would each produce an equivalent crater-shaped depression on the liquid side. Increase in the depression depth further would deepen these depressions from both sides, eventually producing holes through the strip. This mechanism explains the formation of this type of surface defect has been observed in practice, as discussed in section I.

3.7. Discussion

The relation between phenomena and controllable parameters in melt spinning and strip casting is presented schematically in Figure 3.22. This melt-spinning process studied in this work is "flow-rate controlled" with an unconstrained melt pool (puddle) whose length is governed by satisfying both strip thickness (mass balance) and heat transfer (heat balance). For a given nozzle geometry and width of the inlet, the flow rate is a direct function of both gap height and the pressure head exerted by the melt in the crucible. Applying a mass balance to relate the flow rate to the strip thickness at the puddle exit gives Eq [6], which quantifies how strip thickness depends directly on gap height and pressure and inversely with casting speed [47].

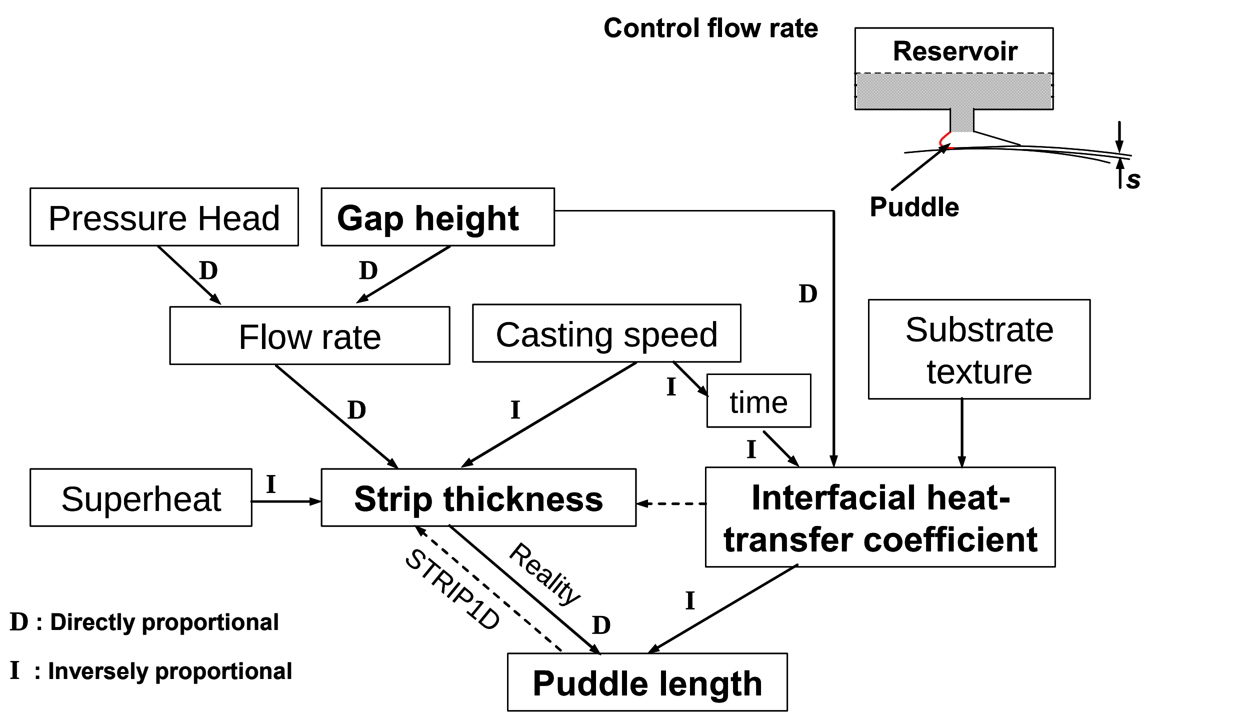

Figure 3.22(a). Relation between melt-spinning phenomena with unconstrained liquid pool (flow-rate controlled thickness)

As shown in Fig. 3.22(a)., it is proposed that a decrease in gap height also decreases the heat transfer coefficient, which together with the strip thickness determines puddle length. This means that any increase in heat transfer coefficient caused by an external process variable (such as substrate texture) for a given gap height produces strips with the same thickness, but requires the puddle length to become shorter in order to accommodate the faster solidification.

As mentioned above, a dependency of the interfacial heat transfer coefficient on gap height has been incorporated into the model used in this study. Perhaps, this is an empirical trend that simply accounts for a systematic measurement error, such as missing rapid fluctuations in puddle length . Alternatively, some other correlated effect might cause similar heat transfer variations with time. From previous work in castings with solid-solid contact [23, 64, 65], the heat transfer coefficient is known to increase with interfacial contact pressure. In the melt-spinning process, the static pressure exerted by the melt in the crucible increases with the head of the liquid in the crucible. Head and thickness both generally decrease with time, so this trend is logical, and likely explains the rapid drop in strip thickness near the end of a cast. However, head is maintained almost constant during most of the casting time for the cases studied here. Furthermore, if the heat transfer coefficient was simply a function of pressure, the decrease in gap height every cycle would increase the pressure, causing increased heat transfer coefficient and strip thickness. This is contrary to the experimental observations, where the decrease in gap height consistently is accompanied by a decrease in thickness. The relation presented here between gap and heat transfer coefficient is a simple way to account for this trend in a quantitative manner and enables the models in this work to match a wide range of measurements. Moreover, a realistic mechanism can be conceived to justify this relation, described in the next section. The effect of increasing casting speed on the heat transfer coefficient has been captured by the increasing nature of the average heat transfer coefficient due to the decreased residence time of the strip on the wheel. Other parameters which are known to affect the heat transfer coefficient, such as wheel texture as discussed in Section II, were assumed to remain constant in this work and deserve further study.

Figure 3.22(b). shows a flow chart describing the phenomena of a single-roll or twin-roll strip-casting process where feedback control is used to maintain a constant liquid level in the melt pool reservoir. Since this maintains a constant puddle length contacting the strip, the interfacial heat transfer coefficient directly controls the strip thickness. Thus, this process is heat-transfer controlled. To satisfy mass balance, changes in strip thickness are accommodated by changing the liquid flow rate entering the reservoir using a flow control mechanism. The STRIP1D model has been developed using the same set of logical relations as this strip casting process, where the puddle length is treated as an input variable.

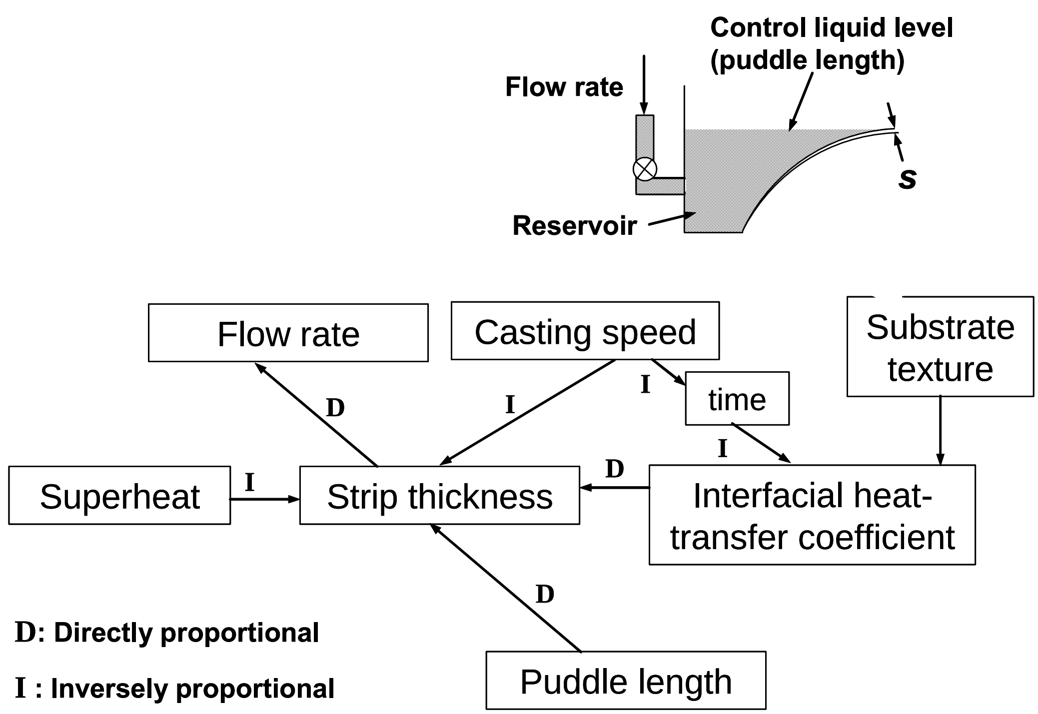

Figure 3.22(b). Relation between phenomena in constrained liquid pool strip-casting (heat transfer controlled thickness)

In a real melt-spinning process, puddle length is determined by the strip thickness and heat transfer, which are both determined by the gap height. These two effects of gap height variations are simultaneously responsible for the strip thickness variations observed in two different time scales. When this STRIP1D model is used to simulate the melt spinning process, the puddle length is treated as an input variable, which together with the heat transfer coefficient control the strip thickness (see dotted arrows in Figure 3.22(a).). Because heat balance and mass balance must both be satisfied, using the heat transfer model to simulate this process and accurately predict strip thickness from a given measured puddle length is equivalent to predicting the puddle length given a measured thickness. Thus, use of the STRIP1D heat-transfer model is valid. The results in Section VI 4 have unorthodox presentation, however, in the sense that they appear to present the effect of puddle length on strip thickness. These results should be interpreted with puddle length (X axis) as the dependent variable.

In contrast to the melt spinning process, an increase in heat transfer coefficient directly increases the strip thickness in the strip casting process. This is because the constant liquid level fixes the puddle length so the process is not flow-rate controlled but heat-transfer controlled. For this reason, any slight change in heat transfer coefficient due to external factors, results in the formation of strip with non-uniform thickness. Changing the control variable in this process to allow the puddle length to adjust could greatly improve the consistency of strip thickness and quality in these processes.

3.8. Proposed Mechanism

A mechanism for solidification and the formation of transverse wavy depressions on the strip surface in the melt-spinning process has been developed based on this work. These steps are consistent with, and build upon the mechanism proposed by Steen and coworkers[2].

- The gap height and pressure head exerted by the melt in the crucible determine the flow rate of the liquid entering the melt pool. The flow rate increases with gap height due to the drop in flow resistance and with pressure head from the Bernoulli relations.
- Time-varying flow in the melt pool causes periodic oscillations of the meniscus, which continuously moves the upstream meniscus upstream and downstream along the wheel surface. The oscillation frequency increases with decreasing melt pool volume, so decreasing gap size causes more oscillations. .
- The upstream movement of the upstream meniscus captures air pockets at the wheel-meniscus contact interface. If capture occurs at the same instant during the meniscus oscillation, the gas pockets will form a discontinuous wavy line with the same shape as the melt pool meniscus at that instant.

- As metal solidifies around these pockets, they form wheel-side surface depressions that move with the strip through the melt pool at the wheel speed.
- The gas pockets retard heat transfer locally, which causes an equivalent liquid-side surface depression with the same shape. The depth of the liquid-side depressions grows with time, according to conduction within the strip. If the gas pockets are they aligned, the depressions they can merge into continuous lines, such as the cross-stream pattern.
- The pitch of the resulting defects naturally has the same frequency as the meniscus oscillation.
- With increasing time, thermal expansion of the heating wheel causes the gap height between the nozzle and the wheel surface to gradually decrease throughout the cast. Superimposed within each wheel rotation cycle, local variations in gap are caused by the slightly oblong shape of the wheel. Superimposed on these variations are the meniscus oscillations that are responsible for the third time scale of thickness variations.
- The decreasing gap height, and its accompanying higher frequency of menisci oscillations, and increased number of air pockets captured, causes a decrease in the average contact area between the liquid and wheel surface. This decreases the interfacial heat transfer coefficient.
- The decrease in gap height is also responsible for a decrease in flow rate, which decreases the strip thickness to satisfy mass balance. Increasing casting speed would cause the same effects.
- Liquid in the melt pool remains until the strip thickness has solidified, which dictates the end of the puddle.

3.9. Conclusions

Two and three-dimensional transient heat-transfer models of the planar-flow melt-spinning process have been developed using ABAQUS and validated using the STRIP1D model, which was presented and validated in chapter 2. The effect of process conditions including casting speed, puddle length, gap height, superheat and interfacial gaps on the heat-transfer occurring during this process have been investigated using these models. A method has been devised to quantify the surface depressions observed in melt spinning has been developed and validated using experimental measurements, which reveals the mechanism of their occurrence.

4. Conclusions

Multi-dimensional heat-transfer solidification computational models of the melt-spinning process have been developed. As a first step, a one-dimensional finite-difference numerical model called STRIP1D has been developed of the process. The model includes a separate fluid-flow model of the melt-pool, which takes into account the effect of fluid flow on the superheat flux entering the solidifying strip. Also, a time-dependent model of the interface heat transfer coefficient has been developed as a part of this model. In an attempt to quantify the effect of interfacial gaps on the heat transfer occurring in the process, two- and three-dimensional transient heat-transfer models of the planar-flow melt-spinning process have been developed using ABAQUS and validated with STRIP1D. These models have been validated using simultaneous predictions of various process parameters obtained from experimental data measured at Cornell. They have then been used to investigate the effect of various process conditions on the heat-transfer during this process. The surface depression predictions obtained using these models have been validated using experimental measurements. This has enabled the formulation of a mechanism governing the melt-spinning process and its underscoring difference from the strip-casting process. The following detailed conclusions arise from this study.

- The superheat flux method presented is a realistic treatment of the effect of the fluid-flow on heat transfer and solidification occurring in the strip and has been validated with other equivalent simple conduction models.

- Heat transfer across the wheel-strip interface governs solidification in the strip and heat transfer to the wheel. It remains constant (h_0) for a small time t_0 (0.1 ms) and then decreases with time given by.

$$h(kW/m^2K) = h_0(kW/m^2K)\left[\frac{10^{-4}}{t(s)}\right]^{\frac{1}{3}} \text{, } t>0.1ms$$

- In addition to controlling flow rate, and thereby strip thickness, a decrease in gap height seems also to decrease the interfacial heat transfer coefficient, perhaps due to increasing the oscillations in the puddle:

$$h_0\ (kW/m^2K)=225\ G(mm)$$

- Strip solidification depends greatly on residence time. As the contact time in zone I increases, the strip thickness increases, for a given interfacial heat transfer coefficient function.
- The observed non-classical solidification front growth profile for different solid fractions is steep with similar steep temperature contours almost parallel to each other. Also, the strip is mushy even after it enters Zone II and rapidly becomes fully solid near the end of Zone II.
- Heat transfer in the wheel is affected by heat loss through wheel sides, which has been taken into account The effect of a thermocouple placed 2mm below the wheel surface has also been captured effectively using a separate model.
- An increase in casting speed decreases the strip thickness due to the decrease in residence time, while an increase in wheel surface temperatures is observed due to increased average interfacial heat transfer coefficient.
- Puddle length increases with strip thickness owing to the increased time needed by the strip to solidify in the melt pool.
- Strip thickness is directly proportional to gap height because an increase in gap height increases the flow rate of the fluid.
- The gap height controls both the strip thickness and the heat transfer from the strip to the wheel, which together determine the puddle length.
- For all other conditions kept the same, an increase in superheat decreases the strip thickness because more heat enters the solidifying strip. If the superheat is very low, the strip might start solidifying at the nozzle resulting in freeze-up.
- The superheat-flux method developed in part one has been further validated using 2-D and 3-D transient heat transfer models.
- Interfacial depressions on the wheel side of the strip interfere with the heat transfer to the wheel and decrease the local solidification rate resulting in an equivalent corresponding depression on the liquid side of the strip.
- Longitudinal depressions formed because of BN deposits on the wheel have been modeled using a 2-D model and validated using micrographs of the samples.
- The melt-spinning process is flow-rate controlled unlike the strip-casting process, which is heat-transfer controlled where the flow rate is controlled by thickness.

- Together, the STRIP1D and ABAQUS models comprise a powerful tool to study these processes. This work explains the variations in the strip thickness observed in three different time / length scales.
    1. Thickness generally decreases with time during the entire cast, due mainly to decreasing gap height as the wheel expands, and also due to heat-up of the wheel.
    2. Thickness variations with the frequency of the wheel rotation are caused by gap variations due to slightly non-circular wheel shape.
    3. Small, closely-spaced transverse depressions occur due to the entrapment of air at the strip-wheel interface, owing to oscillation of the melt pool menisci. They can be predicted using a 3-D model that matches experimental measurements.

This work consists of an important contribution to the aluminum cast shop industry. It is a first attempt to propose, quantify and validate a theory behind formation of defects in aluminum strips produced from the melt-spinning process. Recently the developed models have been used to understand the effect of different types of interfacial gaps on the heat transfer occurring during this process. The models developed, however do not accommodate the hydrodynamic behaviour of the melt pool and the effect of thermal expansion of the wheel on the strip formation. Thermal expansion of the wheel affects the surface of the wheel, which makes it more uneven resulting in formation of gaps, and the stresses developed at the strip-wheel interface results in thermal shrinkage of the strip, thereby causing the strip to separate from the wheel. Furture work in this area should aim at incorporating these factors and thereby leading to a very lucid understanding of the physics underlying the process.

Appendix A

Numerical treatment of governing PDE

Eq. [4] in chapter 2 was discretized using standard 1-D Explicit Finite-Difference equations for each node, based on the following three Taylor series expansions, and neglecting temperature dependency of the thermal conductivity.

$$\frac{\partial T}{\partial t} = \frac{T_i^{n+1} - T_i^n}{\Delta t}, \frac{\partial^2 T}{\partial r^2} = \left(\frac{T_{i+1}^n - 2T_i^n + T_{i-1}^n}{\Delta r^2} \right), \quad \frac{\partial T}{\partial r} = \left(\frac{T_{i+1}^n - T_{i-1}^n}{2\Delta r} \right) \text{ and } \frac{\partial k}{\partial t} = 0 \qquad \text{[A1]}$$

Substituting Eqs. [A1] in [4], and rearranging for T_i^{n+1} gives,

$$T_i^{n+1} = T_i^n + \alpha_w \Delta t \left(\frac{T_{i+1}^n - 2T_i^n + T_{i-1}^n}{\Delta r^2} \right) + \frac{\alpha_w \Delta t}{r} \left(\frac{T_{i+1}^n - T_{i-1}^n}{2\Delta r} \right) + \frac{\Delta t}{\rho_w c_{pw}} Q \qquad \text{[A2]}$$

Boundary equations are obtained by adding and subtracting T_{i-1}^n or T_{i+1}^n accordingly in Eq. [A2] and rearranging. The discretized nodal equations for the strip and the wheel are as given below.

Wheel:

Interior wheel nodes

A heat source is applied to account for convection loss from the large sides of the wheel.

$$Q = -Q_{sides} \qquad \text{[A3]}$$

$$T_{wi}^{n+1} = T_{wi}^n + \alpha_w \Delta t \left(\frac{T_{w(i+1)}^n - 2T_{wi}^n + T_{w(i-1)}^n}{\Delta r^2} \right) + \frac{\alpha_w \Delta t}{r} \left(\frac{T_{w(i+1)}^n - T_{w(i-1)}^n}{2\Delta r} \right) - \frac{\Delta t}{\rho_w c_{pw}} Q_{sides} \qquad \text{[A4]}$$

Wheel Hot Face

Substitute: $\frac{\partial T}{\partial r} = -\frac{q_{wn}}{k_w}$

$$\text{[A5]}\; T_{wn}^{n+1} = T_{wn}^n + 2\alpha_w \Delta t \left(\frac{T_{w(n-1)}^n - T_{wn}^n}{\Delta r^2} \right) + \frac{2\alpha_w \Delta t}{\Delta r} \left(-\frac{q_{wn}}{k_w} \right) + \alpha_w \Delta t \left(-\frac{q_{wn}}{k_w} \right) - \frac{\Delta t}{\rho_w c_{pw}} Q_{sides} \;\text{[A6]}$$

Wheel Cold Face

Substitute: $\dfrac{\partial T}{\partial r} = \dfrac{q_{amb}}{k_w}$ [A7]

$$T_1^{n+1} = T_1^n + 2\alpha_w \Delta t\left(\frac{T_2^n - T_1^n}{\Delta r^2}\right) - 2\frac{\alpha_w \Delta t}{\Delta r}\left(\frac{q_{amb}}{k}\right) + \frac{\alpha_w \Delta t}{r}\left(\frac{q_{amb}}{k}\right) - \frac{\Delta t}{\rho_w c_{pw}} Q_{sides} \quad \text{[A8]}$$

Strip:

Liquids nodes in the strip $1 < si < sf$

$$T_{si}^{n+1} = T_{liq} \quad \text{[A9]}$$

Interior strip nodes, $si > sf$

Substitute: $Q = 0$ [A10]

$$T_{si}^{n+1} = T_{si}^n + 2\alpha_s \Delta t\left(\frac{T_{s(i+1)}^n - T_{si}^n}{\Delta r^2}\right) - \frac{2\alpha_s \Delta t}{\Delta r}\left(\frac{T_{s(i+1)}^n - T_{s(i-1)}^n}{2\Delta r}\right) + \frac{\alpha_s \Delta t}{r}\left(\frac{T_{s(i+1)}^n - T_{s(i-1)}^n}{2\Delta r}\right) \quad \text{[A11]}$$

Strip Cold face

Substitute: $\dfrac{\partial T}{\partial r} = -\dfrac{q_{sn}}{k_s}$ *and being a surface node,* $Q = 2\dfrac{q_{sup}}{\Delta r}$ [A12]

$$T_{sn}^{n+1} = T_{sn}^n + 2\alpha_s \Delta t\left(\frac{T_{s(n-1)}^n - T_{sn}^n}{\Delta r^2}\right) + 2\frac{\alpha_s \Delta t}{\Delta r}\left(-\frac{q_{sn}}{k_s}\right) + \frac{\alpha \Delta t}{r}\left(-\frac{q_{sn}}{k_s}\right) + 2\frac{\Delta t}{\rho_s c_{ps}}\frac{q_{sup}}{\Delta r} \quad \text{[A13]}$$

Here q_{sup} is non-zero only when the strip is less than one node thick.

Strip internal insulated node, where superheat flux is added as a heat source.

$T_{sf} < T_{liq} < Ts_{(f-1)}$

Substitute: $\dfrac{\partial T}{\partial r} = 0$ (insulated boundary condition) and substituting $Q = 2\dfrac{q_{sup}}{\Delta r}$ [A14]

$$T_{sf}^{n+1} = T_{sf}^n + 2\alpha_s\left(\frac{T_{s(f+1)}^n - T_{sf}^n}{\Delta r^2}\right) + 2\frac{\Delta t}{\rho_s c_{ps}}\frac{q_{sup}}{\Delta r} \quad \text{[A15]}$$

Strip Internal node: Alternate method treating superheat flux as a boundary condition.

Substitute: $\dfrac{\partial T}{\partial r} = -\dfrac{q_{sup}}{k_s}$ [A16]

$$T_{sf}^{n+1} = T_{sf}^{n} + 2\alpha_s \Delta t\left(\frac{T_{s(f+1)}^{n} - T_{sf}^{n}}{\Delta r^2}\right) - 2\frac{\alpha_s \Delta t}{\Delta r}\left(-\frac{q_{sup}}{k_s}\right) + \frac{\alpha_s \Delta t}{r}\left(-\frac{q_{sup}}{k_s}\right) \quad \text{[A17]}$$

Note: The last term in Eq. [A17] is negligible, so Eq. [A17] is practically identical to Eq. [A15]

Appendix B

B.1. Calculation of wheel-ambient heat transfer coefficient[40]

$$\mathrm{Re}_{Da} = \frac{2r_0 v_a \rho_a}{\mu_a} = 3.09E+05, \mathrm{Pr}_a = 0.7$$

$$for\ 4E+04 < \mathrm{Re}_D < 4E+05, C = 0.027, m = 0.805$$

The Nusselt's number is given by

$$Nu_{Da} = \frac{2r_0 \bar{h}_{conv}}{k} = C\,\mathrm{Re}_{Da}^m\,\mathrm{Pr}_a^{\frac{1}{3}} = 630. \qquad [B1]$$

This gives $\bar{h}_{conv} \sim 10$ W/m^{2}K

$$\bar{h}_{rad} = \varepsilon\sigma(T_{wn}^2 + T_{amb}^2)(T_{wn} + T_{amb}) \qquad [B2]$$

$$\bar{h}_{rad} \sim 15 \text{ W/m}^2\text{K}$$

$$h_{total} = \bar{h}_{conv} + \bar{h}_{rad} \sim 25. \text{ W/m}^2\text{K} \qquad [B3]$$

B.2. Heat source, Q_{sides}, to account for convective heat transfer from the wheel sides (See Figure 1)

Considering all 4 surfaces of the two wheel sides,

Wheel sides area, $A = 4\Pi r_0^2$

Wheel rim volume, $V = 132.5\Pi(r_0^2 - r_i^2)$

Average heat removed from the wheel nodes, $Q_{sides} = h_{amb} A(T_i - T_{amb})/V$ [B4]

B.3. To model the temperature measured by the thermocouple in the wheel (TC), treat the TC as a series of resistors, (See Figure 14).

The thermal resistance of the air gap is given by

$$R_{air\ gap} = \frac{L_{air}}{k_{air} A_{air}} \quad [B5]$$

The total resistance of the system is the sum of thermal resistances of individual components

$$R_{tot} = R_{air\ gap} + \sum_{i=1}^{4} \frac{L_i}{k_i A_i} + \frac{1}{\sqrt{hPkA}} \quad [B6]$$

Rearrange and solve for the TC temperature, knowing that heat flux through the system is constant

$$T_1 = (1 - \frac{R_{air\ gap}}{R_{tot}})T_0 + \frac{R_{air\ gap}}{R_{tot}} T_{amb} \quad [B7]$$

Substituting values from Table 2,

$$T_1 = 0.89T_0 + 0.11T_{amb} \quad [B8]$$

References

1. J. K. Brimacombe and I. V. Samarasekera: in *Int. Symp. on Casting of Near Net Shape Products*, TMS, Y.Sahai, J.E.Battles, R.S.Carbonara and C.E.Mobley, eds.,Warrendale, PA, 1988, pp. 3-24.
2. C. J. Byrne, E. A. Theisen, B. L. Reed and P. H. Steen: *Metall. Mater. Trans. B,* 2006, vol. 37 (3), pp. 445-456.
3. T.J.Praisner: *Metall. Mater. Trans. B,* 1995, vol. 26, pp. 1199-208.
4. J. S. J. Chen: *Proc. Manufacturing Engineering Division*, ASME, 1996, vol. 4, p. 345.
5. P. H. Steen and C. Karcher: *Annual Review of Fluid Mechanics,* 1997, vol. 29, pp. 373-397.
6. D. Pavuna: *J.Mater. Sci.,* 1981, vol. 16 (9), pp. 2419-2433.
7. S.Kavesh: in *Metallic Glasses*, ASM, J. H. Gilman and H. J. Leamy, eds.,Metals Park, OH, 1978, pp. 36-73.
8. H. H. Liebermann: *Metall. Mater. Trans. B,* 1984, vol. 15 (1), pp. 155-161.
9. R. E. Maringer: *Mater. Sci. Eng.,* 1988, vol. 98, pp. 13-20.
10. P. H. Steen, E. A. Theisen and C. J. Byrne: Cornell University, Ithaca, NY, private communication, 2007.
11. *ABAQUS 6.7 Manual*, ABAQUS Inc.,Providence, RI, 2007.
12. G. Li and B.G. Thomas: *Metall. Mater. Trans.,* 1996, vol. 27B (3), pp. 509-525.
13. *FLUENT6.1-Manual*, Fluent Inc.,Lebanon, New Hampshire, 2003.
14. C. J. Byrne, S. J. Weinstein and P. H. Steen: *Chem. Eng. Sci,* 2006, vol. 61 (24), pp. 8004-8009.
15. K. Takeshita and H. Shingu: *Trans. Jpn. Inst. Met.,* 1986, vol. 27 (6), pp. 454-462.
16. L. Granasy and A. Ludwig: *Mater. Sci. Eng.,* 1991, vol. 133A (1), pp. 751-754.
17. J. Birat, M. Larrecq, J. Lamant and J. Petegnief: *Proc. Mold Operation for Quality and Productivity*, A. W. Cramb and E. Szekeres, eds., ISS, Warrendale, PA, 1991, pp. 3-14.
18. W. Blejde and R. Mahapatra: *Proc. The Belton Memorial Symposium*, Sydney, Asutralia, 2000, pp. 1-14.
19. K. G. Keanini: *Int. J. Heat and Mass Transfer,* 1998, vol. 41 (2), pp. 275-285.
20. C.A. Muojekwu, I.V. Samarasekera and J.K. Brimacombe: *Metall. Mater. Trans. B,* 1995, vol. 26B (2), pp. 361-382.
21. G. Li and B. G. Thomas: *Metall. Mater. Trans. B,* 1996, vol. 27B (3), pp. 509-525.
22. G. X. Wang and E. F. Matthys: *Int. J. Heat and Mass Transfer,* 2002, vol. 45 (25), pp. 4967-4981.
23. K. Ho and R. D. Phelke: *Metall. Mater. Trans. B,* 1985, vol. 16 B (3), pp. 585-94
24. J. S. J. Chen, R. C. Ren and A. A. Tseng: *J.Mater. Proc. Manufac. Sci.,* 1995, vol. 3 (4), pp. 373-386.
25. J. K. Carpenter and P. H. Steen: *Int. J. Heat Mass Transfer,* 1997, vol. 40 (9), pp. 1993-2007.
26. J. Kukura, K. Ford, A. Singh and P. H. Steen: *Simul. Mat. Proc.: Theory, Methods, and Applications,* 1995, pp. 1153-57.
27. G. X. Wang and E. F. Matthys: *Int. J. Heat and Mass Transfer,* 1992, vol. 35 (1), pp. 141-153.
28. N. H. Pryds and J. H. Hattel: *Modelling Simul.Mater. Sci. Eng.,* 1997, vol. 5 (5), pp. 451-472.

29. J. Masounave, J. Blain, E. Essadiqi and S. Caron: in *Int. Symp. on Casting of Near Net Shape Products*, TMS, Y.Sahai, J.E.Battles, R.S.Carbonara and C.E.Mobley, eds.,Warrendale, PA, 1988, pp. 473-492.
30. S. Caron, E. Essadiqi, F. G. Hamel and J. Masounave: *Proc. Light Metals*, TMS, Warrendale, PA, 1990, pp. 967-973.
31. J. P. Papai and C. E. Mobley: in *Int. Symp. on Casting of Near Net Shape Products*, TMS, Y.Sahai, J.E.Battles, R.S.Carbonara and C.E.Mobley, eds., Warrendale, PA, 1988, pp. 51-62.
32. J. A. Dantzig and C. L. Tucker III: *Modeling in Materials Processing*, 1 ed., Cambridge University Press, Cambridge, UK, 2001.
33. J. P. Papai and C. E. Mobley: in *Int. Symp. on Casting of Near Net Shape Products*, TMS, Y.Sahai, J.E.Battles, R.S.Carbonara and C.E.Mobley, eds.,Warrendale, PA, 1988, pp. 79-90.
34. R. K. Mallik and S. P. Mehrotra: *ISIJ International,* 1993, vol. 33 (5), pp. 595-604.
35. S. L. Wu: *Applied Mathematical Modeling,* 1992, vol. 16, p. 394.
36. J. C. Moore: *Proc. Light Metals*, J. Evans, ed., TMS, 1995, p. 1137.
37. P. H. Steen, B. L. Reed and M. B. Kahn: *Inter. Dynamics of Convection and Solidification,* 2001, pp. 145-153.
38. M. Bussmann, J. Mostaghimi, D. W. Kirk and J. W. Graydon: *Int. J. Heat Mass Transfer,* 2002, vol. 45 (19), pp. 3997-4010.
39. X. Huang, B. G. Thomas and F. M. Najjar: *Metall. Trans. B,* 1992, vol. 23B (6), pp. 339-356.
40. F. P. Incorpera and D. P. Dewitt: *Fundamentals of Heat and Mass Transfer*, 5 ed., John Wiley & sons, Hoboken, NJ, 2002.
41. J. Blumm, J. B. Henderson and L. Hagemann: *Proc. High Temperatures-High Pressures*, ECTP, 1998, vol. 30, pp. 153-57.
42. C. J. Byrne, K. M. Aaron, S. P. Baker and P. H. Steen: *Mater. Sci. Eng. A,* 2007, vol. 459 (1-2), pp. 172-181.
43. M. Bamberger, B.Z. Weiss and M.M. Stuperl: *Mater. Sci. and Tech.,* 1987, vol. 3 (2), pp. 49-56.
44. J.E.Spinelli, M.D.Peres and A.Garcia: *J. alloys and compounds,* 2005, vol. 403, p. 228.
45. I. Jimbo and A. Cramb: *Metall. Mater. Trans. B,* 1993, vol. 24B, pp. 5-10.
46. B. G. Thomas, J. T. Parkman and T. Chandra: in *Thermec 97 Int. Conf. on Thermomechanical Processing of Steel and Other Materials*, vol. 2, TMS,Wollongong, Australia, 1997, pp. 2279-2285.
47. J. K. Carpenter and P. H. Steen: *Journal of Materials Science,* 1992, vol. 27 (1), pp. 215-225.
48. S. C. Huang and H. C. Fiedler: *Metall. Mater. Trans. B,* 1981, vol. 12 (6), pp. 1107-1112.
49. P. H. Steen and A. H. Hirsa: *Proc. NSF Design and Manufacturing*, San Juan, PR, 2002.
50. P.H. Steen, B.G. Thomas and S. Baker: *Proc. 2005 NSF Design, Manufacture and Industrial Innovation Grantees* J. Shaw, ed., Scottsdale, AZ, USA, Jan. 3-6, 2005, 2005, vol. MPM # DMI0423791, pp. T/BGT/1-24.
51. P. H. Steen, U.S Patent 7,082,986 2006.
52. P. H. Steen: "Collaborative Research: Casting by Design EBM (TSE01-1)", Cornell University, Ithaca, NY, Nugget Report to NSF Grant Number # DMI- 0124730, 2001.
53. B.G. Thomas: *Proc. 3rd Internat. Congress on Science & Technology of Steelmaking*, Charlotte, NC, 2005, pp. 847-862.

54. J. Sengupta, B.G. Thomas, H.J. Shin, G.G. Lee and S.H. Kim: *Metall. Mater. Trans. A,* 2006, vol. 37 A (5), pp. 1597-1611.
55. S. N. Singh and K. E. Blazek: *J. Metals,* 1974, vol. 26, pp. 17-27.
56. M.S. Jenkins, B.G. Thomas, W.C. Chen and R.B. Mahapatra: *Proc. 1994 Steelmaking Conference*, Chicago, IL, 1994, vol. 77, pp. 337-345, 82.
57. B.G. Thomas, D. Lui and B. Ho: *Proc. Sensors and Modeling in Materials Processing: Techniques and Applications*, Orlando, Florida, USA, 1997, pp. 117-142, 55.
58. J. Kubota, K. Okimoto, M. Suzuki, A. Shirayama and T. Masaoka: *Proc. ISC. The Sixth International Iron and Steel Congress.* , Nagoya, Japan, 1990, vol. 3, pp. 356-363.
59. Y. Sasabe, S. Kubota, A. Koyama and H. Miki: *ISIJ Int.,* 1990, vol. 30 (2), pp. 136-141.
60. J. Legresey, Y. Brechet and P. Menet: *Scripta Mater.,* 1997, vol. 36 (12), pp. 1437-42.
61. P. H. Steen, E. A. Theisin and C. J. Byrne: Cornell University, Ithaca, NY, private communication, 2007.
62. A. Sundararajan and B.G.Thomas: *Submitted to Metall. Mater. Trans. B.,* 2007.
63. P. H. Steen and T. Ibraki: in *Melt Spinning, Strip Casting and Slab Casting*, TMS, E. F. Matthys and W. G. Truckner, eds.,Warrandale, PA, 1996, pp. 159-171.
64. C.V. Madhusudana and L.S. Fletcher: *AIAA Journal,* 1985, vol. 24, pp. 510-23.
65. M. Bellet and B.G. Thomas: in *Materials Processing Handbook*, J. R. Groza, J. F. Shackelford, E. J. Lavernia and M. T. Powers, eds., 2007, p. 6.